NOVEL THERMOELECTRIC GENERATOR

FOR STATIONARY POWER WASTE HEAT RECOVERY

by

Kylan Wynn Engelke

A thesis submitted in partial fulfillment
of the requirements for the degree

of

Master of Science

in

Mechanical Engineering

MONTANA STATE UNIVERSITY
Bozeman, Montana

January 2010

APPROVAL

of a thesis submitted by

Kylan Wynn Engelke

This thesis has been read by each member of the thesis committee and has been found to be satisfactory regarding content, English usage, format, citation, bibliographic style, and consistency, and is ready for submission to the Division of Graduate Education.

Dr. Stephen Sofie

Approved for the Department of Mechanical Engineering

Dr. Christopher Jenkins

Approved for the Division of Graduate Education

Dr. Carl A. Fox

STATEMENT OF PERMISSION TO USE

In presenting this thesis in partial fulfillment of the requirements for a master's degree at Montana State University, I agree that the Library shall make it available to borrowers under rules of the Library.

If I have indicated my intention to copyright this thesis by including a copyright notice page, copying is allowable only for scholarly purposes, consistent with "fair use" as prescribed in the U.S. Copyright Law. Requests for permission for extended quotation from or reproduction of this thesis in whole or in parts may be granted only by the copyright holder.

Kylan Wynn Engelke

January 2010

ACKNOWLEGEMENTS

I would like to thank Dr. Stephen Sofie for his incredible energy, enthusiasm and support for this project. I would also like to thank Dr. Vic Cundy, Dr. Ruhul Amin and Dr. Steven Shaw for their generous time and support on my graduate committee.

This work was performed under Department of Defense contract W9132T-05-C-0027: Large Scale Thermo-Electric Power Generation Demonstration for DoD Applications for Leonardo Technologies, Inc. I thank LTI for their incredible support and very much appreciate the opportunity given to me by this project. My greatest thanks to Joel Lindstrom of LTI with whom I worked extensively on this project and Craig Cassarino of LTI, who made the project possible.

I would also like to thank Nik Sorenson for his incredible CAD work; and thanks to the folks of JE Soares of Belgrade for facilitating our fabrication needs. And last, but certainly not least, I would like to thank my parents, Keenan and Lana Engelke, whose encouragement and support helped make this project a reality.

TABLE OF CONTENTS

TABLE OF CONTENTS-CONTINUED

TABLE OF CONTENTS-CONTINUED

TABLE OF CONTENTS-CONTINUED

TABLE OF CONTENTS-CONTINUED

TABLE OF CONTENTS-CONTINUED

LIST OF TABLES

Table Page

LIST OF FIGURES

Figure Page

LIST OF FIGURES - CONTINUED

LIST OF FIGURES - CONTINUED

Figure Page

LIST OF FIGURES - CONTINUED

Figure Page

LIST OF FIGURES - CONTINUED

LIST OF ABBREVIATIONS

TE ..... Thermoelectric
SSP ..... Small-Scale Prototype
FDP ..... Field Demonstration Prototype
Genset ..... Generator Setup
TEG ..... Thermoelectric Generator
emf ..... Electromotive Force
FOM ..... Figure of Merit
RTG ..... Radioisotope Thermoelectric Generator
GPHS-RTG ..... General Purpose Heat Source RTG
PVD ..... Physical Vapor Deposition
CTE ..... Coefficient of Thermal Expansion
DAQ ..... Data Acquisition System
ICAL ..... Imaging and Chemical Analysis Laboratory – MSU Campus
FE SEM ..... Field Emission Scanning Electron Microscopy (Microscope)
EDS ..... Energy Dispersive X-ray Spectroscopy (Spectrometer)
XRD ..... X-ray Diffraction (Diffractometer)
TGA ..... Thermogravimetric Analysis
DTA ..... Differential Thermal Analysis
DI ..... Deionized (Water)
CAD ..... Computer Aided Drafting and Design
CNC ..... Computer Numerically Controlled
SS ..... Stainless Steel
IR ..... Internal Resistance
LPG ..... Liquefied Petroleum Gas
RTD ..... Resistance Temperature Detector
DMM ..... Digital Multimeter

ABSTRACT

Internal combustion engines produce much excess heat that is vented to the atmosphere through the exhaust fluid. Use of solid-state thermoelectric (TE) energy conversion technology is a promising technique to recapture some of the energy lost. The TE effect, discovered in 1821 by Thomas Seebeck, is essentially the solid-state conversion of a temperature gradient into an electric potential. The scope of this work was the design, testing and evaluation of a novel and robust TE generator that is amendable to use in a vast array of convective thermal processes.

Seebeck testing of TE elements was combined with thermal/hydraulic and thermoelectric modeling to develop the design of a working prototype system. A proof-of-concept small-scale prototype (SSP) TE generator was built to evaluate concepts intended for the construction of a fully-functional field demonstration prototype (FDP). The SSP was used to evaluate electrical contact integrity, thermal characteristics, various TE materials and the feasibility of using compression-based TE contacts. The SSP featured 9 P/N TE pairs and has thus far produced a maximum open-circuit voltage of 380mV and a maximum electrical power of 1.47W. Knowledge gained from the SSP construction and testing was utilized in the design and fabrication of the FDP.

A liquid-cooled Honda ES6500 6.0kW genset was procured to provide a test-bed for the FDP. The primary goal was to power the electric radiator fan with the heat energy contained in its exhaust, thus decreasing the genset's fuel consumption rate. The FDP contained 256 P/N pairs and thus far has produced an open-circuit voltage of 5.5VDC and a maximum power of 8.49W. Replacing the stock muffler reduced fuel consumption by 11.6% whereas removing the fan load reduced it an additional 1.64%. Through the recovery and conversion of wasted thermal energy, the genset's fuel consumption rate was successfully lowered, therefore validating the benefits of secondary TE power systems. The radiator fan of the Honda ES6500 consumes approximately 1% of the overall power output of the genset. Radiator fans in larger gensets can draw as much as 12-16% of their peak output. By recuperating waste heat, substantially higher fuel savings could be achieved.

CHAPTER 1

INTRODUCTION

Project Motivation

The motivation of this project was not only to make use of available waste heat sources, but to also create a high-performance thermoelectric module that is robust and has a wide range of applications. Current TE modules are very fragile and tend to have problems with internal thermal expansion differences due to fixed soldered connections. The foremost feature of this project was the development of a TE generator with no soldered joints and a high enough power output to be useful in practical applications.

Most industrial and power generation processes produce unwanted excess heat. Much of this heat is expelled through exhaust fluids. If the exhaust fluids contain enough heat, they can be used to operate a turbine, a boiler or some other cogenerative process. If the amount of heat expelled is not significant enough to be used in a typical fashion, the heat is exhausted to the atmosphere. Any heat exhausted to the atmosphere can be thought of as “wasted” heat. One very promising option for recovering the energy lost through waste heat is the use of thermoelectric power generation.

Thermoelectric Heat Exchanger

The goal of this project was to design and construct a TE heat exchanger for the conversion of waste heat into a useful amount of electrical power. The design was to be open-ended and applicable to almost any industrial process in which unwanted heat is produced.

Thermoelectric Generator Application

The most important aspect of the project was to prove the merit of a TE heat exchanger by retrofitting an existing system that could use supplemental DC power. A Honda ES6500 generator setup (genset) was chosen because it featured an electric fan that cooled the liquid coolant radiator. The fan consumed 50-60W of DC power that was provided from a sub-winding within the generator. If the fan could be powered completely by the thermoelectric generator (TEG), a load would be relieved from the generator, thus increasing overall energy conversion efficiency and lowering total fuel consumption. It was very important that any additions to the genset imposed no parasitic loads or impeded the genset's function in any way.

Basic Design-Thermohex®

The basic design of the TE heat exchanger was to feature a novel fin-fin/plate-fin configuration with a hot fluid applied to one side of the stack and a cooler heat sink fluid applied to the other. The fins were not only to transmit heat to and from the TE elements, but to also conduct electricity produced by the elements

through the Seebeck Effect. The overall design of the TEG was based on a patent pending and trademark design known as THERMOHEX® (THERMOelectric Heat Exchanger) and is currently under development with Thermohex, LLC.

Electrical Connections

The most novel aspect of the design was that no electrical connections would be soldered per the current state-of-the-art. The use of soldered connections introduces mechanical problems and temperature limits. All internal contacts were designed to be dry with either a highly conductive contact medium or simply no contact media between the TE elements and the conduction fins.

Small-Scale Prototype

In order to test and evaluate concepts developed as the project moved forward, a small-scale prototype (SSP) design was to be developed. The SSP was to serve as a proof-of-concept test bed to allow for a non-soldered TE system to be tested and proven.

The SSP module was to feature up to 9 N/P pairs (18 TE clusters) in all. The SSP would be of great importance in the project due to the fact that it could easily be disassembled, modified and reassembled per changes in the overall design.

Field Demonstration Prototype

The final product of this research was to be a fully-functional, power producing TE heat exchanger to serve as a demonstration prototype. The Field Demonstration Prototype (FDP) was to be implemented into a genset as a means to provide supplemental DC power to the genset's electrical system, namely the electric radiator fan. The two main sources of waste heat, the coolant radiator and exhaust fluid, were investigated as possible heat sources for the TE generator. Ultimately, it was decided that the exhaust fluid would be used as the heat source because it was a gas and at a much higher temperature. By powering the fan externally, improvements in the genset's power conversion efficiency were hypothesized, tested and achieved.

CHAPTER 2

BACKGROUND

The Thermoelectric Effect

The TE effect is defined as the solid-state conversion of a thermal gradient directly into electricity and vice versa. TE energy conversion requires that a temperature gradient be maintained across the thermoelements which in turn produce the electromotive force (emf) that creates the voltage potential. The temperature difference produces waves in the crystal lattice called phonons. These phonons interact with other phonons, grain boundaries and crystal imperfections in the crystal lattice; as well as charge carriers such as free electrons in metals and valence electrons and gaps in semi-metals and semiconductors. It is the interaction of the phonons and charge carriers (known as 'phonon drag') that allows for the TE effect to be possible.

When a TE material is at an equilibrium temperature, all phonons are equal in magnitude and opposite in direction and cancel one another out. It is only when a temperature gradient is introduced that there is an imbalance in phonon density along the material imposing an electron density imbalance and, ultimately, electric voltage potential. Phonon mechanics will be discussed in further detail later in this chapter.

Almost all metals and most other electrically conductive materials (semimetals, semiconductors, etc.) have been shown to exhibit TE properties. The

TE effect is a result of the excitation of charge carriers in materials; free electrons in metals and valence electrons/holes in semiconductors. Only relatively few materials exhibit pronounced TE behavior. The magnitude of the TE effect is directly linked to the mobility and mean free path of the charge carriers of the material.

Most TE materials are characterized by a parameter known as the thermoelectric Figure-of-Merit (FOM). This parameter can be thought of as a performance characterization of how well the thermoelectric material performs in electrical power generation. It allows many different types of TE materials to be compared when making a decision on what material is to be used in a design. The TE FOM will be discussed in further detail in subsequent sections of this work.

Sign Convention

The TE material sign convention defined in this work will be characterized as having one of the following two behaviors: P-type and N-type. P-type (positive type) materials exhibit a positive voltage difference across a positive temperature gradient. N-type (negative type) materials exhibit a negative voltage difference across a positive temperature gradient. More importantly, N-type materials yield electron flow in the same direction as heat flow, whereas P-type materials yield electron flow in the opposite direction of heat flow. This phenomenon is very useful for the fabrication of devices having multiple junctions in series in order to obtain useful output voltages and currents. Note that the sign convention used in this study is completely arbitrary; its only importance is for consistency. Another

important point to note is that the P and N-type nomenclature used in this body of work in no way refers to P and N-type conduction of semiconductive materials. The P and N-type convention used strictly for semiconductor theory deals directly with the way that electrical energy is conducted through the molecular lattice, either with free/valence electrons or with valence "holes." The P/N convention used for this work is simply to differentiate the voltage polarity vs. temperature gradient behavior of the materials. It is for this reason that metallic TE materials are characterized as either P or N-type in this study.

The TE effect can be characterized in the following two ways: (a) a temperature gradient used to produce a voltage potential, or (b) a voltage potential used to produce a temperature gradient. Effect (a) works as a solid-state electric generator much like a fuel cell, only instead of using hydrogen and oxygen concentration gradients, it makes use of thermal gradients imposed by heat sources and sinks. Effect (b) works as a heat pump and can be used in solid-state heat transfer applications.

A Brief History of Thermoelectrics

Seebeck Effect

The TE effect was discovered in 1821 by Thomas J. Seebeck. Seebeck discovered the effect using two wires or strips composed of dissimilar metals bonded at two junctions and imposing a temperature gradient, ΔT ($\Delta T=T_2-T_1$), from one end to the other. Seebeck constructed a device using two dissimilar metals,

copper and iron, connected at both ends. He noticed that when one side of the device was heated with a candle, a compass needle near the wire deflected. Seebeck initially hypothesized that the temperature gradient induced a magnetic field, and he published his findings in his paper, *Magnetische Polarisation der Metalle und Erze durch Temperatur-Differenz* (loosely translated: *Magnetic Polarization of Metals and Minerals due to Temperature-Difference*). The observed magnetic field was later discovered to be resultant of the flow of electrons around the closed current path. It was determined that an open-circuit voltage could be produced as indicated in the diagram in Figure 1. The Seebeck Effect essentially describes a solid-state thermoelectric generator.

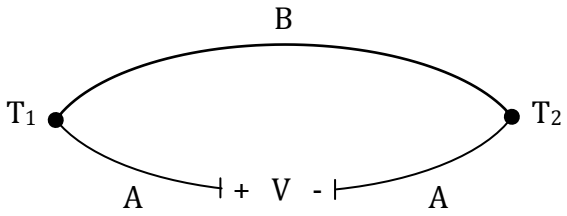

Figure 1: Principle of the Seebeck Effect

Seebeck then found that the temperature difference and voltage output were directly related. In order to convey this relationship, Seebeck formulated the following equation:

$$V_{AB} = (S_A - S_B) \cdot \Delta T \quad (1)$$

Where V_{AB} is the voltage potential, ΔT is the temperature difference, and S_A and S_B are the relative Seebeck coefficients of the two metals. The Seebeck coefficient is useful when discussing TE materials since it only characterizes the

voltage potential produced due to the applied temperature gradient. Units for Seebeck coefficients are expressed in microvolts per degree Kelvin (μV/K).

Peltier Effect

The Peltier Effect was discovered by Jean Peltier in 1834. The Peltier Effect is essentially the Seebeck Effect in reverse. When an electric current is applied across two junctions of two dissimilar materials a temperature gradient is produced. The Peltier Effect can be thought of as a solid-state heat pump. Peltier, like Seebeck, noticed a direct correlation between the amount of heat pumped and the electrical current passing through the circuit. Figure 2 illustrates the Peltier Effect, which is characterized by Equation 2, the Peltier Relation:

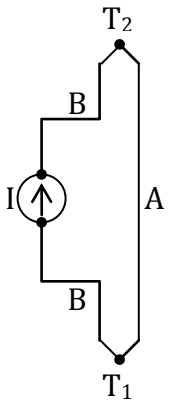

Figure 2: Principle of the Peltier Effect

$$Q_{AB} = (\Pi_A - \Pi_B) \cdot I \qquad (2)$$

Where Q_{AB} is the rate of heat pumped, Π_A and Π_B are the respective Peltier coefficients and I is the electric current passing through the circuit. The Peltier

coefficient is primarily of use when comparing TE materials for heat transfer devices designed for cooling applications.

Thomson Effect

William Thomson (Lord Kelvin) further simplified the mathematics behind the TE effect. In 1854 Thomson set out to incorporate the newly formulated Laws of Thermodynamics into TE phenomena. He first formulated the following relationship:

$$q_A = \tau_A \cdot I \cdot (dT/dx) \quad (3)$$

Where q_A is the rate of heat absorption per unit length of the conductor, τ_A is the Thomson coefficient of conductor A, I is the electrical current and dT/dx is the temperature gradient per unit length along the conductor.

This relationship is thermodynamically reversible. It also describes the behavior of a discrete material; unlike the Seebeck and Peltier relationships which describe junctions of materials. By postulating that the First and Second Laws of Thermodynamics could be applied to the TE circuit, Thomson related all three TE coefficients.

$$\tau_{AB} = T \cdot (dS/dT) \quad (4)$$

$$\Pi = S \cdot T \quad (5)$$

Where, as before, τ_{AB} is the Thompson Coefficient, T is absolute temperature (K), dS/dT is the change in Seebeck Coefficient with respect to absolute temperature and Π and S are the Peltier and Seebeck Coefficients, respectively. These

relationships have been validated empirically and have been shown to have an accuracy of 2-5% (Blatt 1976).

TE phenomena have been the topic of much study and analysis for nearly two centuries; however, TE technologies used for power generation have had limited practical application, namely due to their low efficiency, as well as due to their impractical integration and scale-up. Thermoelectric efficiency as it relates to Carnot theoretical efficiency is described in further detail later in this chapter.

TE Material Parameters

Several material parameters must be considered when assessing the performance characteristics of TE materials. The Seebeck coefficient (S) is of great importance. It is a description of what voltage potential can be produced given an applied temperature gradient. Electrical conductivity is also very important since high electrical conductivity (σ) is required for efficient TE operation. If the electrical conductivity is too low, much of the electrical power will be lost due to significant Ohmic losses as power is drawn from the TE generator. Finally, thermal conductivity (κ) is of great importance since low thermal conductivity permits a material to retain a large temperature gradient.

The three material properties involved in the TE FOM are highly dependent on temperature. In order to predict TE performance accurately, the temperature to which the module will be subjected must be included in all material parameter values.

The three main parameters, S, σ and κ, comprise the thermoelectric Figure-of-Merit, as defined in Equation 6:

$$Z = S^2 \cdot \sigma / \kappa \tag{6}$$

As is apparent, the TE FOM is proportional to the square of the Seebeck coefficient. Any change in the Seebeck coefficient will have a profound effect on the TE FOM. Thermal and electrical conductivity also greatly influence the FOM, therefore all three parameters must be considered and optimized with respect to one another when making a TE element selection. The TE FOM has units of (1/K). Z-values for common TE materials are provided in Table 2. In some instances, the TE FOM is multiplied by the absolute nominal temperature in order to obtain a dimensionless FOM, known as ZT.

TE Generation Efficiency

The general definition of the efficiency of a thermal process is the ratio of the amount of energy output to the amount of energy input. Since the First Law of Thermodynamics states that energy is neither created nor destroyed, this ratio is always less than or equal (only in theory) to 1. Since the Carnot efficiency is the maximum theoretical efficiency of a thermal process, the maximum TE efficiency must be a function of that value. The Carnot efficiency of a thermal process is provided in the following equation (Sonntag 2003):

$$\eta_C = \frac{T_h - T_c}{T_h} \tag{7}$$

Where η_C is the Carnot efficiency, T_h is the hot temperature and T_c is the cold. The efficiency of a TE module can then be thought of as the ratio of the power applied to a load to the amount of heat absorbed at the hot junction. This relation is shown below (Rowe 2006):

$$\gamma_{TE} = \frac{\sqrt{1+\overline{ZT}}-1}{\sqrt{1+\overline{ZT}}-\frac{T_h}{T_c}} \tag{8}$$

Where γ_{TE} is the TE efficiency, ZT is the dimensionless TE FOM, and T_h and T_c are the hot and cold junction temperatures, respectively. Combining the two efficiencies gives an overall possible energy conversion efficiency of:

$$\eta = \eta_C \cdot \gamma_{TE} = \frac{T_h - T_c}{T_h} \cdot \frac{\sqrt{1+\overline{ZT}}-1}{\sqrt{1+\overline{ZT}}-\frac{T_h}{T_c}} \tag{9}$$

This efficiency approximation does, however, come with several assumptions. The thermal inlet and outlet are assumed to be capable of transferring the same amount of heat; thermal resistances at inlet and outlet are equal and negligible in comparison to the entire system; and the material properties comprising the ZT (Seebeck coefficient, thermal and electrical conductivity) are assumed to be uniform and constant. In reality, Seebeck coefficients and thermal and electrical conductivities are strongly dependent on temperature and must be dealt with accordingly when using these relations in actual design. Figure 3 shows the TE efficiency for three different Z-values. The Z data used is of the TE materials for this study.

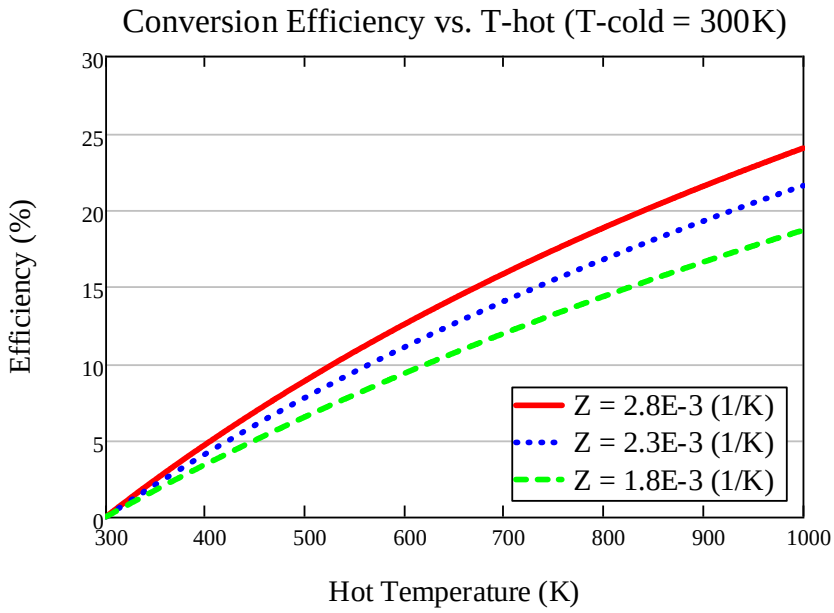

Figure 3: TE Efficiency vs. Hot-Side Temperature

Figure 3 features the theoretical TE/thermal efficiency as a function of hot temperature for three different values of Z. The values of Z between 1.8 and 2.8 (1/K) are actual values of the TE FOM for TE materials used in this study.

Mechanisms of Thermoelectrics

Atomic Bonding

In metals, atoms are bonded together in a large electron gas. When the individual atoms are bonded together, their electrons move from the valence/conduction bands of the individual atoms to the overall conduction band due to the overlapping valence and conduction bands. This is somewhat of a weak bond, but it allows for the atoms to move in relation to one another without complete fracture. This is seen as elastic and plastic yielding of the material on the

macro scale. The vast number, usually one or two per atom, of free electrons makes metals highly conductive, both thermally and electrically. Metallic crystals are typically of the close-packed variety, i.e. face-centered cubic, body-centered cubic, hexagonal close-packed. Most metals and their alloys are bonded metallically (Burns 1985; Kittel 2005).

In ionic materials, the atomic bonding is due to the electrostatic attraction of two oppositely charged atoms. When ions are bonded, electrons are transferred amongst them in order to fill electron shells or to get rid of spare electrons. The positive ion will accept excess electron(s) from the negative ion, leaving both with electrons in lower potential energies. Ionic materials typically form two types of crystal structures, face-centered cubic (sodium chloride) and simple cubic (cesium chloride). The alkaline metals from the left side of the periodic table (Na, Mg, and Cs) typically form ionic compounds with nonmetals from the right side (Cl, F). These compounds are seldom found in practical TE materials. Ionic materials conduct through the transport of ions through the lattice. This phenomenon is very useful in fuel cells, which require ion transport, but is not of much value in TE applications (Burns 1985; Kittel 2005).

In covalently bonded materials, the constituent atoms share electrons. Examples of covalent compounds are carbon, in the form of graphite or diamond; silicon, in its pure semiconductive form or in simple quartz crystals; and even gases such as methane and propane. Covalent bonds are very strong and the shared electrons tend to be localized. The localized valence electrons then require a certain

amount of energy to become conduction electrons. This is known as the band gap, E_g. When the E_g threshold is reached, the electron "jumps" to the conduction band and becomes available for electricity conduction. It is now, however, at a higher potential energy and will fall back into the valence band at its nearest convenience, filling a valence "hole." Figure 4 illustrates a comparison between the band gap in insulators, semiconductors and metals (Kittel 2005).

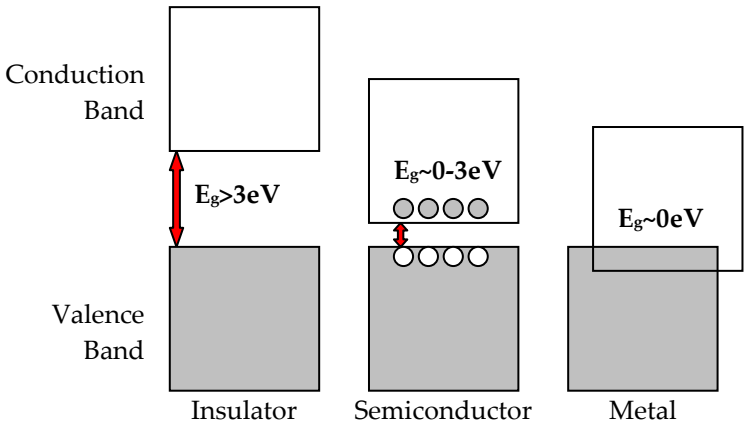

Figure 4: Band Gap Theory

All elements feature a valence and conduction band in their electron shells. Insulators are characterized as non-conductive but do, in fact, have a bridgeable band gap, but it is usually so wide (>3 or 4eV) that it cannot be overcome unless subjected to very high voltages, yielding dielectric effects. Semiconductors typically have an E_g between 0 and 3eV. Metals and semimetals typically have an E_g of 0eV due to their overlapping valence and conduction bands (Yu 2001).

Phonons

Phonons are defined as vibrations of the crystal lattice of a material. The atoms in a lattice are suspended in a three dimensional array. Each atom has attraction and repulsion forces acting upon it, holding it in its equilibrium position. These atomic attraction and repulsion forces are what hold the lattice structure together and keep it from simply collapsing inward or diffusing outward.

The stiff and strong covalent bonds found in the diamond structure are ideal for phonon transport, making the thermal conductivity of diamond very high. The covalent bonding in the diamond structure locks up all electrons resulting in almost no free charge carriers to conduct electricity. This results in diamond being a very good thermal conductor, but a very poor electrical conductor. The thermal conductivity of natural diamond has been measured to be on the order of 2400-2500 W/m-K (Pan 1995). The electrical conductivity of diamond varies greatly with temperature: $\sim 10^{-4}(\text{ohm-cm})^{-1}$ at 1200°C and $\sim 10^{-15}(\text{ohm-cm})^{-1}$ at 100°C (Pan 1995).

In thermal equilibrium, all lattice elements are equally excited, meaning they are all vibrating with relatively the same frequency and amplitude all directions. In this condition, phonons are present but tend to cancel each other out, thus eliminating any cooperative interactions which would yield notable TE behavior. When a temperature gradient is introduced, the lattice is no longer in thermal equilibrium. The thermal gradient causes the lattice elements on the hot side of the material to be more excited than the elements on the cold side. Since the phonons

on the hot side have more thermally induced kinetic energy than those on the cold side, they tend to move to a state of lower kinetic energy, causing them to "flow" from the hot side to the cold side, thus inducing overall heat flow per the Second Law of Thermodynamics (Sonntag 2003). This phenomenon is illustrated in Figure 5.

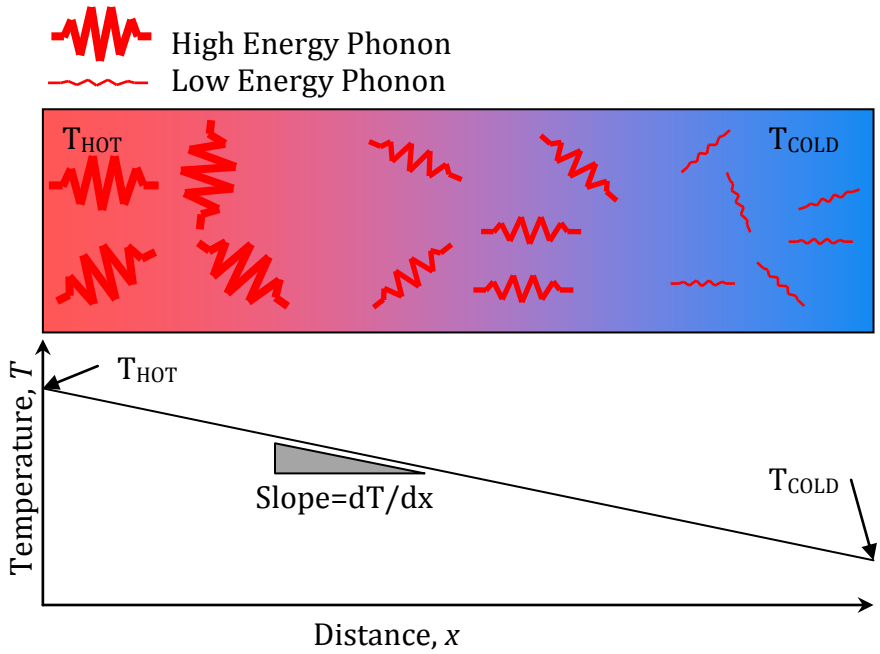

Figure 5: Phonon Energy vs. Temperature (Ashby 2007)

As phonons travel through the lattice of the element, they impact other phonons, grain boundaries, lattice imperfections and charge carriers. These interactions cause phonon scattering. However, the most important interaction is the one that makes the TE effect possible, phonon-to-charge carrier interaction. The magnitude of this interaction dictates the magnitude of the Seebeck Effect of a material. (Rowe 2006)

In metals, charge carriers are free electrons. In semiconductors, charge carriers are valence electrons and valence gaps (holes) in the outer shells of the valence bands of the individual lattice elements. P-type TE semiconductors are doped to have more holes than electrons in the valence band. This imbalance causes P-type TE semiconductors to conduct through the transfer of holes in the valence band of the atom. N-type TE semiconductors are doped with an abundance of electrons. They conduct through valence electrons freed into the conduction band of the outer shells of the atoms. Further discussion regarding semiconductor physics is provided later in this section.

Phonons set charge carriers in motion as they flow through the structure and cause the carriers to "pile up" at one side of the TE element. In both types of TE materials (P and N), the phonons cause an imbalance in charge carriers along the length of the temperature gradient, yielding an electric potential.

TE Materials

As stated previously, most conductive materials exhibit some level of TE behavior. TE materials can be roughly classified into three general categories: metals, semi-metals and semiconductors.

Metals: Metallic TE materials are of increasing interest in the field of thermoelectricity. Metals have high electrical conductivity as well as superior mechanical properties. However, they tend to have poor TE performance

characteristics. Another problem encountered with metals is their high thermal conductivity, which can make it difficult to impose a large temperature gradient.

The key disadvantage of metallic conductors is that the proportionality between their electrical and thermal conductivity remains nearly constant. The Weidmann-Franz law states that the thermal and electrical conductivity of metals, which are driven by free/conduction electron transfer, can be correlated with a constant coefficient known as the Lorenz number: $L = \kappa/\sigma T \approx 2.45E\text{-}8\ W\cdot\Omega/K^2$ (Kittel 2005). At constant temperature, the thermal conductivity of a metal cannot be increased without increasing the electrical conductivity at the same time since both are driven by free electrons. Increasing the Seebeck coefficient would have a great deal of positive impact on the TE FOM. This is of limited possibility because the Seebeck coefficient is directly dependent on free electrons. All three parameters depend in some form, on the concentration and mobility of charge carriers, i.e. free electrons (Cadoff 1960).

Another major issue with the use of metals is their high temperature performance. Most metals tend to exhibit undesirable oxidation characteristics at high temperatures. Metal oxides tend to be quite non-conductive which can lead to the degradation of electrical contacts. Another high temperature issue with metals is that their electrical conductivity decreases with increased temperature. This phenomenon is due to the increased number of electrons and phonons of colliding with lattice imperfections resultant from the higher kinetic energy of the electrons and phonons (Kittel 2005).

Metallic TE materials in the form of wires have been available for many years. Thermocouples are comprised of two dissimilar TE metals which have a common junction so that when the junction is at a certain temperature, the thermocouple outputs a known voltage. Thermocouples are very robust and are a very accurate and very repeatable tool for making temperature measurements. They are also incredibly simple to use and can be used to very high temperatures. The overall Seebeck coefficient for a thermocouple is what is used to convert the output voltage to temperature.

TE metals in wire form work well for temperature measurement but generally their TE FOM is too low for their practical use in TE power generation or cooling equipment. Some examples of typical metallic TE materials used in thermocouples are: Constantan (55%Cu 45%Ni), Chromel (90%Ni 10%Cr), platinum and palladium. The average Seebeck coefficients over the range 25-625°C for Chromel and Constantan vs. Ag wire were measured to be -22 and 48μV/K, respectively. These results are shown in Table 5 in the Results section. Note that the measurements performed for this body of work are in the opposite polarity of those in the data found in published values. More discussion will be presented on polarity conventions in subsequent sections.

Semimetals: Semimetals are materials that have electrical conduction properties of both metals and semiconductors. A semimetal is a material that has a small overlap of the valence and conduction bands in its outer electron shells. The

overlap allows excess valence electrons to move freely to the conduction band. This overlap is small compared to that of true metals, which makes their conductivities 1-2 orders of magnitude lower than true metals. The electrical conductivity of semimetals is typically on the order of 10^4 $(ohm\text{-}cm)^{-1}$ whereas metals have conductivities on the order of $10^5 – 10^6$ $(ohm\text{-}cm)^{-1}$ (Burns 1985).

Semimetal compounds typically consist of at least one semi-metal element compounded with a metal or non-metal. Semi-metallic elements, also known as metalloids, are found along the metal/non-metal separation line in the Periodic Table. They include but aren't limited to: boron (B), silicon (Si), arsenic (As), antimony (Sb), bismuth (Bi) and tellurium (Te). One interesting point to make is that graphite is considered a semi-metal due to its semimetallic conduction properties.

As previously discussed, semiconductive materials (including semi-metals) do not conduct electricity in the same way that metals do. In metals, the conduction and valence bands overlap so no extra energy is required to move an electron. In semiconductors, the valence and conduction bands are not overlapping. A band gap separates the valence and conduction bands in a semiconductor's outer electron shell. The band gap can be thought of as an amount of energy that needs to be overcome before the valence electrons can be used as conduction electrons.

Semi-metal compounds generally comprise of the most efficient and widely used TE materials. They are commonly constructed in a bulk dice configuration, i.e. small cubes. These bulk dice are then arranged in alternating P and N-type

configurations in order to produce the desired output performance. Figure 6 shows a typical P-N couple and how the voltage potential of each type related to an imposed temperature gradient.

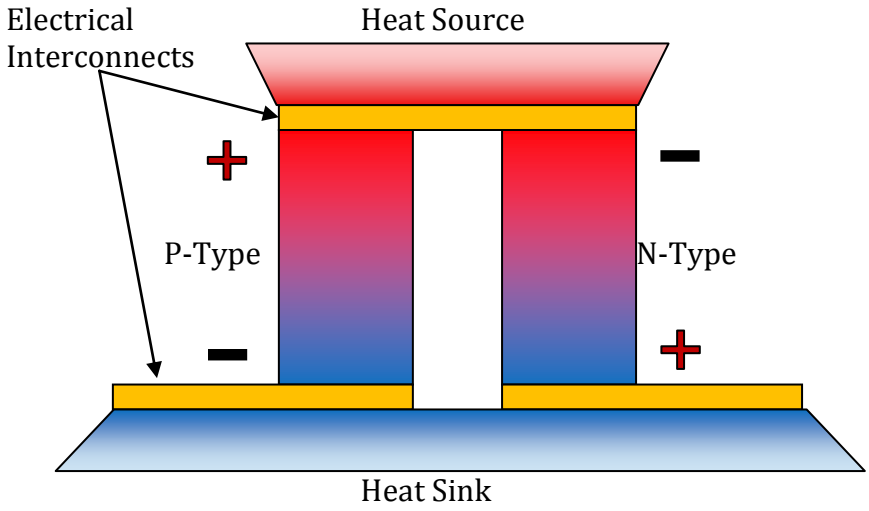

Figure 6: TE Generator Schematic

Semi-metals are of much use due to their relatively high TE output performance. They tend to have a TE FOM on the order of 10-100 times that of their metal counterparts (Tittes 2003). They can also be "doped" with impurities to enhance and manipulate their TE properties. These dopants can be used to increase electrical conductivity and Seebeck coefficient, as well as decrease thermal conductivity. The properties can also be optimized for the desired temperature range. Further, doping can also alter the fundamental conducting behavior of the N or P-type material. The most commonly used TE material, bismuth telluride (Bi_2Te_3) can be doped with either selenium or antimony to adjust TE polarity to either P or N.

Semi-metal TE materials do have their own unique set of challenges. Raw material cost, in addition to difficult processing and fabrication can lead to somewhat expensive semi-metal TE materials. The semi-metal TEs act much like ceramics in that they tend to have poor mechanical properties, most notably, low fracture toughness. Table 1 lists typical fracture toughness, K_{1c}, values of common design materials.

Table 1: Fracture Toughness Values of Select Materials at Room Temperature (Dowling 1999)

Material	**Fracture Toughness, K_{1c}: MPa-m$^{1/2}$**
AISI 4130 Steel	110
2024-T351 Aluminum	34
Ti-6Al-4V Titanium	66
ABS Plastic	3.0
PVC Plastic	2.4
Soda-Lime Glass	0.76
Alumina, Al_2O_3	4.0

Fracture toughness is a measure of a material's resistance to brittle fracture. It is a function of the material's yield strength and size of inherent cracks within the grain structure of the material. A material with a high K_{1c}, can resist brittle fracture even with large internal cracks. A material with a low K_{1c}, will experience brittle fracture even with very small inclusions. (Dowling 1999)

Materials of this type are constructed as bulk dice which can be a detriment if size and dimension restrictions are present. Construction of bulk dice consists of growing crystals composed of the TE material and then either machining the crystals into bulk die or pulverizing the crystals and then hot pressing the resulting

powder into the desired shape and size. The properties of Bi_2Te_3 crystals tend to be highly anisotropic, requiring special attention with regard to crystal orientation. The pulverization and hot pressing can correct the anisotropies of the material, but this processing further increases the cost of manufacture and may adversely affect TE performance. Another problem encountered with bulk dice is that electrical circuit construction can be difficult due to the fact that thermal expansion differences between the semi-metal TE material and the metallic electrical contacts can cause destructive stress concentrations which can severely inhibit the practicality of TE modules under desired working conditions. Thermo-mechanical issues will be discussed in depth later in this chapter.

Some common semi-metal TE materials include Bi_2Te_3, PbTe, and ZnO_2. As stated earlier, Bi_2Te_3 is the most widely used TE material and has proven itself useful for both cooling operations and power generation. It exhibits competitive performance and relatively low cost due, in part, to its established market presence. The magnitude of the Seebeck coefficient of both P and N-type Bi_2Te_3 typically lies between 170 and 260 μV/K (Goldsmid 1986).

Semiconductors: Semiconductors tend to have very high Seebeck coefficients. They can be doped to increase electrical conductivity and inherently they have low thermal conductivity. Thermal and electrical properties of semiconductors can be independently altered through doping. This is due to the fact that neither thermal nor electrical conductivity depend explicitly on the presence of free electrons. Both are defined by what is known as a “mean free path.”

The mean free path is defined as the average distance a particle or phonon travels before colliding with other particles/phonons or imperfections (Burns 1985). A material's electrical conductivity is also directly dependent on the charge carrier mobility of that particular material, which is directly dependent on the charge carrier mean free path. The mean free path for phonons in a material defines its thermal conductivity (Ashby 2007).

Semiconductive TE materials include silicon and its variants (quartz, silicon carbide, etc.), germanium and even carbon (graphite, diamond, carbon nanotubes). The Seebeck coefficient of chemical vapor deposited diamond doped with boron has been found to be between 300-600 μV/K (Balducci 2006). Diamond has a very high band gap at room temperature, 5.47eV (Burns 1985), making it almost electrically insulating. It also has very high thermal conductivity, hindering the introduction of thermal gradients. The high performance of these materials is generally eclipsed by their high cost and less-than-desirable mechanical properties.

Table 2 features the Seebeck coefficients and TE FOM of several TE materials. Included are pure metals (Ni, Cr), metallic compounds (Ni-Cr, Cu-Ni), semimetals (Bi, Sb), semimetal compounds (Bi_2Te_3) and a pure semiconductor, (p-doped silicon).

Table 2: Seebeck Coefficients and TE FOM for Select TE Materials at Room Temp (Tittes 2003)

Element/compound	$\alpha(10^{-6}$ V/K)	$\alpha^2\sigma/\kappa$ (10^{-3} K^{-1})
$(Bi_{2-x}Sb_x)Te_3$	210	1-3
p-Bi_2Te_3	140	
p-Si	1300	0.0001
Sb	48	0.03
Ni-Cr (80/20)	25	0.04
Cr	22	0.03
Ni	-20	0.04
Cu-Ni	-35	0.09
Bi	-68	0.3
n-Bi_2Te_3	-110 to -250	1-3
$Bi_2(Se_xTe_{3-x})$	-250	

Notice that while silicon has a very high Seebeck coefficient, its TE FOM is quite low due to its high thermal conductivity and electrical resistivity. The two most common TE materials, and incidentally those used in this work, are antimony and selenium-doped bismuth telluride; found at the very top and bottom of Table 2. These two materials have TE FOMs on the order of 1-3 (K^{-1}), making them ideal for TE power generation.

Current Use of Thermoelectric Generators

Radioisotope Thermoelectric Generators

Radioisotope thermoelectric generators (RTGs) use the temperature gradient between a decaying radioactive material as a heat source and a flowing liquid metal as a heat sink to produce a temperature gradient across a TE module. RTGs are useful in remote locations where a steady power source is required but solar arrays or stationary engine power is not practical, i.e. above the Arctic/Antarctic circles.

They are also of great use in deep space where solar energy is not strong enough to be used by photovoltaic devices.

Some examples of the radioactive materials employed as heat sources for RTGs are Plutonium 238 (the most popular due to its relative safeness of use), Strontium 90, Polonium 210, Cerium, and Americium 241. RTG candidate materials must be of fissile nature, but also must be within a certain output radiation limit. Radioactive materials for use in RTGs must have an optimum half-life that allows them to output a sufficient amount of heat over a long enough period of time for the module to be useful.

RTGs have been used by NASA since the 1960's as power sources for deep space probes and on the Apollo missions to the moon. They are extremely valuable in deep space where solar energy is no longer a viable source of energy to power the probes' systems. The space probes Galileo, Ulysses, and more recently, Cassini-Huygens were all designed around a General Purpose Heat Source RTG (GPHS-RTG) power supply. The Cassini-Huygens probe was powered by 3 GPHS-RTGs, providing a total of 887W of electrical power (Bennett 2008). A single GPHS-RTG weighed approximately 56.4kg and was 114cm long and 42.2cm in diameter across the fins. The "general purpose heat source" was Pu-238 which emits alpha particles. Emitted alpha particles are easily absorbed and convert to heat well. The TE elements were doped Si-Ge elements capable of withstanding temperatures of 1300K.

RTGs have also been used in the medical field. They were introduced in the early 1970s as highly reliable power sources for cardiac pacemakers. They were

typically powered by 0.2-0.5 grams of Pu-238 and had an intended useful life of 20 years, but some still functioned adequately after 35+ years. RTG pacemakers were designed to use either a metallic thermocouple array or a semiconductor TE material thermopile to convert the heat of radioisotope decay to electricity. The first human-implanted RTG pacemaker was powered by a $Pu^{238}Sc$ alloy heat source and a Bi_2Te_3 thermopile and could output 250μW of power. (Parsonnet 1973)

The protective structure around the radioactive material is designed to withstand daily life including falls and other trauma and even events as extreme as gunshots and cremation. The stigma associated with nuclear power has hastened the retirement of the RTG in medical applications. Rechargeable lithium-ion batteries have been used to power pacemakers since the mid-to-late 1970s.

Combustion Powered TE Generators in Remote Areas

Another heat source for use in TE generators is the combustion of a hydrocarbon fuel such as natural gas. If a source of fuel is present, but no energy infrastructure is available, a TE generator is a low maintenance, highly reliable source of electricity. The available fuel source can be combusted in a burner and the heat applied to the hot leg of the TE generator. Depending on the environment, the cold leg can simply be a heat sink exposed to the surroundings, or a heat-pipe cooling system. A simple schematic of a combustion-powered TE generator is shown in Figure 7.

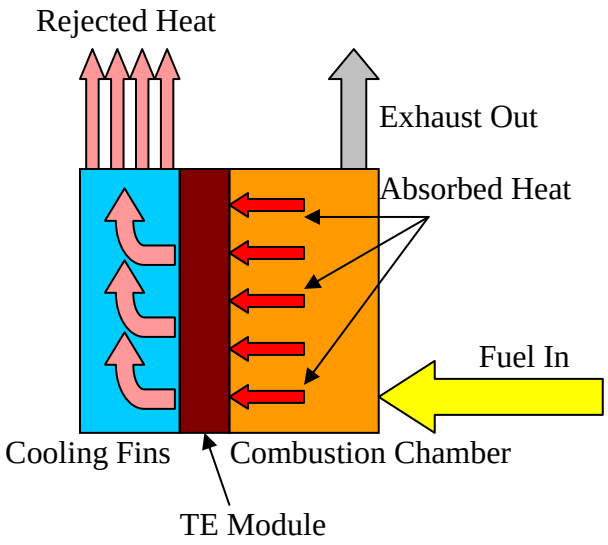

Figure 7: Combustion-Powered TE Generator Concept

Fuel is combusted in a chamber where the heat is conducted directly to the TE module. The cold-side of the TE module is cooled using passive cooling systems. The use of TE generators in remote areas along pipelines and other remote areas provides a low maintenance, economical source of DC power that can be used for diagnostic and communications systems as well as cathodic corrosion protection. Using self-contained remote power systems coupled with wireless telemetry reduces the need for expensive power and communication infrastructure.

TE Generators as Standalone Power Systems

TE power generation is somewhat of a niche applied area of power production. TE generators, as discussed previously, are typically used as remote power sources where the use of traditional generators is not practical.

TE power generation typically has an efficiency of less that 10%, meaning less than 10% of the heat transferred through the TE generator is converted into

electricity. Ideal heat cycles such as Carnot and can exhibit efficiencies of nearly 60-80%. A Stirling engine is a heat engine that uses externally applied heat to expand and contract the gas within its closed system to convert heat to work. An ideal Stirling cycle absorbs and rejects heat isothermally (at constant temperature) and, therefore, has the same theoretical efficiency as the ideal Carnot cycle previously discussed (Sonntag 2003). Their theoretical ideal efficiency as a function of the cycle's high temperature is shown in Figure 8.

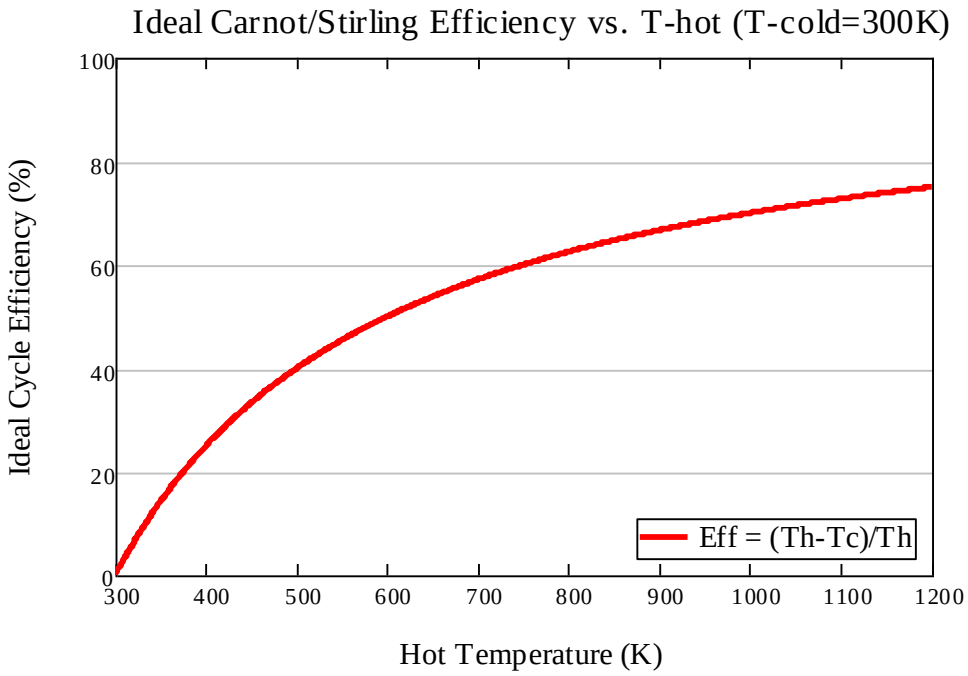

Figure 8: Ideal Carnot/Stirling Efficiency vs. Hot Temperature

Due to the relatively low efficiency of the TE power generation process, it would be impractical to use as a standalone system for the generation of grid-magnitude power. TE generators are, however, very useful as supplemental power systems. They can be included in combined cycle thermal processes as a way of

capturing waste heat that is not practical for use in other cogeneration applications. TE generators are simple systems with very few, if any, moving parts and little to no required maintenance over the span of their useful life. Even at only 10% efficient, TE generators can prove themselves more than useful in recovered energy over the course of their use. The overall value of a TE generator increases greatly when applied to waste heat sources of thermal systems without hindering their intended performance, i.e. without increasing fluid pressures, adding parasitic loads, or adding a detrimental amount of weight or volume to the system.

Inconsistencies in Documented Research of the Thermoelectric Effect

Through rigorous research and testing, a firm understanding of the TE effect and its constituents has been attained. Through the inspection of documented research, several issues have arisen:

Poor Documentation of TE Test Data

In-depth explanations into the fundamental mechanics of the TE effect are difficult to locate within most published discussions. The concepts of phonons and charge-carriers are well documented and understandable, but the interaction between the two that yields the TE effect is not thoroughly explained.

Another source of vagueness in TE research is that tests performed to determine Seebeck coefficients and thermal emf characteristics of materials are not well documented, and therefore not reproducible. Testing conditions and

apparatuses are not defined in much detail. Historical data currently used as base-lines for much design and testing seems to not have a good source of reference. In the TE metals work performed by Cusack and Kendall methods of testing for Seebeck coefficients are cited but are difficult to reproduce. This is due to their involvement of superconducting materials used for one leg of the TE couple being tested. The superconductive material effectively has a Seebeck coefficient of zero so it can be neglected and the other's Seebeck can then be determined. This method is very difficult to perform without the proper equipment and materials.

Most existing data used as baselines for material testing proves difficult to use. Much of this historical data does not seem to include an accurate enough description of its origin to be used as a means to predict TE behavior of desired materials (Cusack 1958). The data is typically given as a table of Seebeck coefficients or thermal emf values with reference to temperatures. Another difficulty found was that the reference temperature against which the values were plotted was typically not well defined. It could have been the mean temperature of the material with a set temperature difference, or it could have been either the hot or cold side temperature used during the test.

Some existing research also does not describe what material was used as the reference junction when testing for Seebeck and thermal emf. A reference junction is needed as a means to read the voltage potential of the specimen when undergoing high temperature testing. The reference junction almost always imparts its own thermal emf that must be taken into account in order to obtain true Seebeck values

for the sample specimen only. It is the inherent connection between the overall Seebeck coefficient of the couple and the coefficients of each leg that clouds the data and creates difficulty in application.

P vs. N-Type Material Sign Conventions: The Case for Consistency

Another major inconsistency encountered in research of the Seebeck effect was the P vs. N sign convention. A standardized sign convention of the behavior of TE materials does not seem to be evident in existing Seebeck research. P and N-type behavior refers to the polarity of the voltage potential produced given an applied temperature gradient. The voltage potential can be positive in the direction of a positive temperature gradient or it can be negative in the direction of the same positive temperature gradient.

In order to mitigate confusion and for the sake of consistency, a standard P vs. N-type behavior sign convention was introduced and implemented for this body of work. P-type will refer to the behavior where a positive voltage potential is read in the same direction of the positive temperature gradient (increasing temp). N-type will refer to the behavior where the positive voltage potential is in the opposite direction of the temperature gradient. This convention was chosen mostly for the fact that it intuitively made sense on the level of carrier transport. Figure 9 illustrates the standardized sign convention introduced for this project and used throughout.

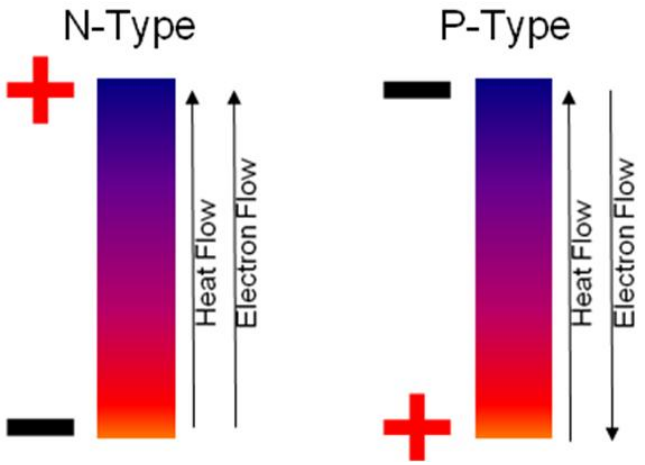

Figure 9: N vs. P-Type TE Behavior

The disciplines of physics and electrical engineering are at odds with respect to electrical conduction. In electrical engineering, electrons flow from a positive terminal to a negative/ground. Physics states that electrons, in fact, flow from the negative terminal to the positive through electrostatic attraction; i.e. electrons are negatively charged and are therefore attracted to a positive charge. Without attempting to rectify this discrepancy, this body of work will use the electrical engineering definition of electric current, i.e. positive current measured going from positive terminal to negative. Figure 10 has been provided to aid in clarification of these conventions.

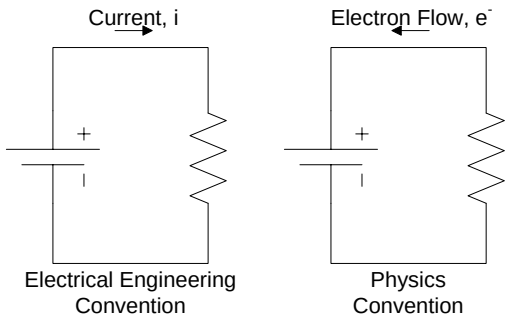

Figure 10: Electric Current in Electrical Engineering and Physics

Electroplating

Electrodeposition Background

Electroplating, better characterized as electrodeposition, is the process by which ions of a specific material are deposited onto the surface of another through an anodic reduction reaction facilitated by an electrolytic process. The source ions can be simply dissolved as metal salts in an acid or alkaline solution or they can come from the galvanic corrosion of a sacrificial anode. Typically, a combination of both is used.

The electrodeposition process is facilitated by the imposition of an electric current through an ionic medium between an anode and the material to be plated known as a cathode. The anode is charged with the positive terminal of a current source and the cathode is charged with the negative terminal. As the electrons flow from the anode to the cathode, they impose a charge on the metal particles in the solution and on the anode. The charged particles, called ions, are attracted to the oppositely charged cathode. They move through the electrolytic solution to the cathode and become attached to the surface. As more and more ions are

transferred, the cathode surface becomes covered with an even, homogeneous layer of deposited material. Figure 11 features a simple galvanic cell used for electrodeposition (McChesney 2004).

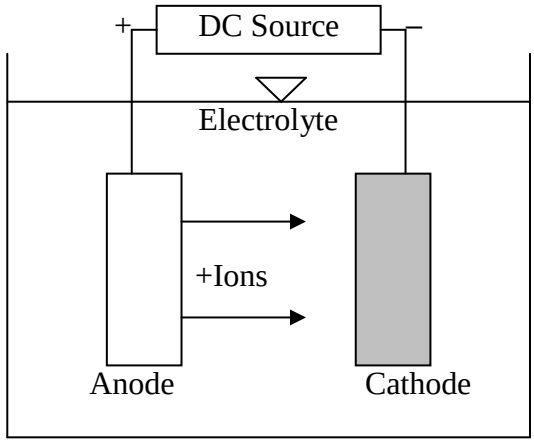

Figure 11: Simple Galvanic Cell (McChesney 2004)

Electrodeposition is used as a surface treatment for several reasons. It is used to coat a surface for aesthetic/decorative reasons. It is also used to protect an object's surface from oxidation, corrosion, mechanical wear, etc. It is also used to fundamentally change the chemical nature of the surface being plated.

Electrodeposition is also used to create a specific chemistry of the plating material. For instance, electroplating a material onto the surface of an inert cathode (stainless steel) can yield a layer of highly pure material that can be removed from the cathode and used elsewhere. The plated material's physical and chemical properties as well as its crystal structure can be altered and tailored to its intended result (Tittes 2003). The electrodeposition of the TE material bismuth telluride has been investigated as a means for formulating very pure, high performance TE

elements. Metals such as gold, platinum, and silver can also be refined to extremely high purity through an electrodeposition process.

Thermoelectric Heat Exchanger Concepts

The purpose of a TE heat exchanger is to take an available source of heat, create a gradient between the heat source and an available heat sink, and apply that gradient across a material to produce a notable amount of thermal emf. If a TE heat exchanger is designed correctly, it can then become a TE generator. The TE generator can then be used as a source of supplemental electrical power to help take parasitic loads off of the primary generation device(s), decreasing the overall rate of fuel consumption of the process.

TE Heat Exchanger

The TE generator in this project initially took the design of a counterflow fin-fin heat exchanger with heated air as the hot fluid and room temperature air as the cold fluid. As discussed earlier, the TE effect, namely the Seebeck effect, is a function of an imposed thermal gradient, thus requiring a drastic temperature change at the location of the TE elements. The design of the TEG eventually took the form of a cross/counter-flow hybrid design. The overall layout resembled a plate-fin or plate-frame heat exchanger

Because traditional semi-conductor TE elements tend to have poor mechanical properties, TE metals were initially used. Foils made from the thermocouple alloys Constantan and Chromel were the initial candidates for the TE

generator design. Many other metal foils were tested and investigated as potential candidates for the power generating material for use in the TE generator.

Metal TE materials are much more robust and easier to obtain but tend to have on the order of 10 times lower thermal emf output as their semiconductive counterparts. After much testing and deliberation it was determined that the higher power output characteristic of the semiconductors greatly outweighed their higher cost and lower mechanical strength.

Existing TE Module Design

Some existing TE module designs utilize solder to make thermal and electrical contacts. TE circuits are typically soldered together via an array of conductive metal interconnects arranged so that the ideal combination of voltage and current is produced. The TE circuit is typically fixed onto a ceramic substrate (typically alumina, Al_2O_3) with a high thermal conductivity to conduct as much heat as possible to and from the module to increase its overall performance. Matweb.com gives the thermal conductivity of alumina to be 20-40 W/m-K over the range of ~25-250°C.

Soldering the TE dice to the metal interconnects can pose several problems. Most TE elements are comprised of Bi_2Te_3 doped with antimony or selenium. Bismuth telluride has high susceptibility to "poisoning" when in contact with certain metals. The term poisoning means that when a certain material comes in contact with the material in question, it diffuses into the atomic structure and degrades the performance of the element. Bismuth telluride has shown notable degradation

when in contact with metals such as tin, nickel and copper (Lan 2008). Solders containing these elements can cause undesirable degradation and performance loss if no steps are taken to combat diffusion. Degradation can come in the form of changes in charge carrier density and lower thermopower output. Another problem with the diffusion of the solder into the TE element is that when material leaves the solder layer, voids are created, thus lowering the overall electrical conduction area of the contact and decreasing performance through higher resistance.

Steps taken to combat diffusion have been the use of diffusion barriers deposited on the connection surfaces of the TE dice. Nickel (Ni) is a great tin diffusion barrier, but it also diffuses into the bismuth telluride crystal structure. Molybdenum (Mo) has been found to be a good nickel diffusion barrier and is currently in use for this purpose. The Mo and Ni are typically deposited in very thin layers (~1-10μm) using physical vapor deposition (PVD). One example of PVD is the rapid heating the deposition material to the point where it becomes an ionized vapor. The material to be coated is electrostatically charged opposite in polarity to the ion vapor so the particles will be attracted. The charged substrate is put in the presence of the ion vapor which then adheres. The result is a highly pure, strongly bonded layer of deposited material. The requirement of the TE dice to be coated with multiple layers can lead to high production costs in terms of time and money.

One of the biggest problems encountered when using soldered connections in TE modules is that the coefficient of thermal expansion (CTE) of the solder is much different than that of the TE elements. The CTE of a material is a measure of

how much the material changes in dimension as a function of temperature. Thermal expansion is resultant from the increase in kinetic energy of the material's individual particles. Their higher energy caused them to collide more frequently with more energy, thus forcing them apart, therefore yielding expansion due to thermal energy (Ashby 2007). It is typically represented as 10^{-6}m/m/°C or ppm/°C and its units take the form of 10^{-6}/K.

When the module is brought up to operating temperature, stresses induced from different rates of thermal expansion can be destructive to the TE dice. Another issue encountered is that the solder plastically deforms as the module experiences thermal cycling. This plastic deformation can lead to increased electrical resistance in the solder layers. Finding solders that do not degrade the performance of the TE elements and have comparable CTE values has been a great challenge in designing high-performance soldered TE modules with long operation lives.

Table 3 features the thermal and mechanical properties of components of typical TE modules as presented by Hori, et al. in his publication "Analysis on thermo-mechanical stress of thermoelectric module."

Table 3: Thermal/Mechanical Properties of TE Module Components (Hori 2000)

Material	**Young's Modulus (GPA)**	**CTE (ppm/K)**	**Thermal Conductivity (W/m-K)**
Al_2O_3 Substrate	310	7.20	17.0
Copper	117	17.1	390
Sn-Pb Solder	18.0	23.4	46.5
Ni	201	13.7	90.5
Bi_2Te_3	40.0	13.0	1.50

As is apparent, there are several mismatches in material stiffness and CTE of the individual components. All material dimensions must be tailored to optimize the operating conditions and internal stresses of the TE module.

Previous Work

This work was a continuation of the work performed in DOE Contract Number DE-AM26-99FT40465- ‘‘Final Report, Evaluation & Demonstration of Broad Applications for Thermoelectric Devices for DOE’s Office of Industrial Technologies,” and US Patent Application: 20080142069-“A Thermoelectric module.”

CHAPTER 3

LABORATORY TESTING PROCEDURES

TE Material Testing

Seebeck Coefficient Testing

The first iteration of the Seebeck testing chamber featured fire-brick walls pasted together with ceramic epoxy. A hinged door was also attached to aid in sample loading. The chamber had a slot cut in one side to allow for sample strips to be inserted. The heat source was a Robertshaw Uni-Line Model 41-402 silicon carbide hot surface igniter. The power to the heating element was regulated through a Variac® Type W5MT3 variable voltage autotransformer. The transformer allowed for discrete temperatures to be achieved within the Seebeck chamber, greatly improving the accuracy of the data taken. Pictures featuring this Seebeck chamber are featured in Figure 12 and Figure 13.

Figure 12: Seebeck Testing System

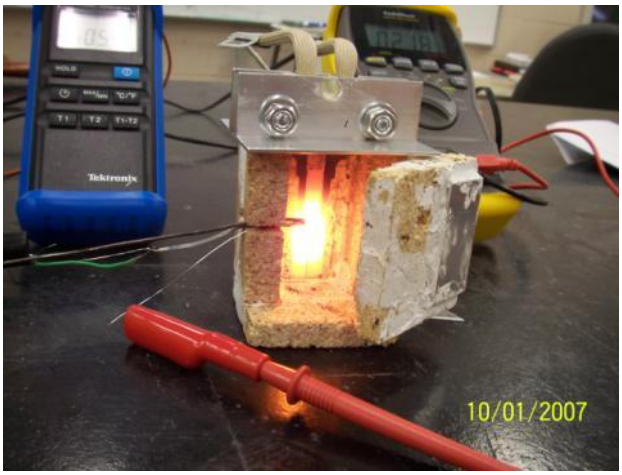

Figure 13: Detail of Initial Seebeck Chamber

Through repeated testing, the initial test chamber was not sufficiently durable to withstand further use. A more advanced Seebeck chamber was constructed as a replacement. This iteration of the Seebeck testing apparatus was constructed from Zircar Ceramics' ZAL-45AA refractory sheet and adhered together with high temperature ceramic epoxy. ZAL-45AA is a 97% alumina, 3% silica insulation board capable of withstanding extremely high temperatures (~1550°C). The refractory sheet was cut into interlocking pieces to aid in construction and to increase the strength of the chamber. The same silicon carbide hot surface igniter was installed as the heat source and a slot was cut in the side of the chamber to allow easy and accurate sample placement. The improved Seebeck chamber is shown in Figure 14.

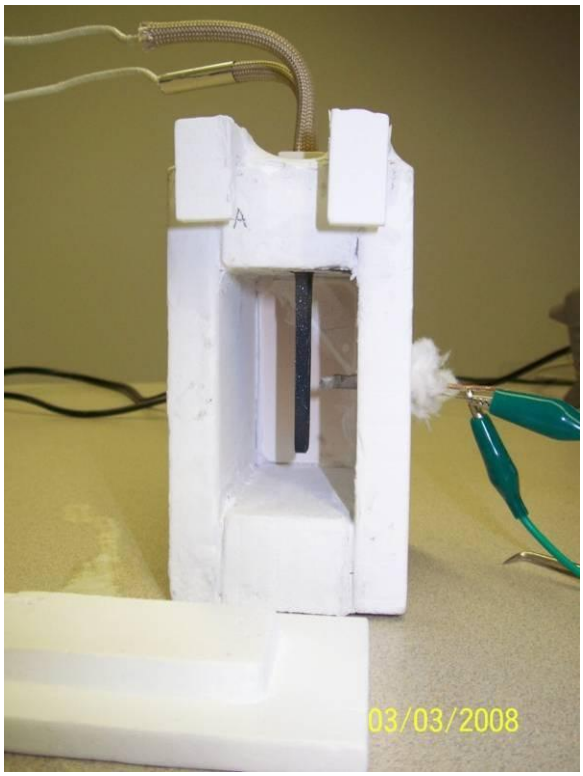

Figure 14: Detail of Improved Seebeck Chamber

Several different metals and alloys were tested as potential candidates for the TE generator. The materials tested included many different copper-nickel alloys, cobalt foil, many different nickel-chromium alloys, some iron-chromium alloys, several brazing and soldering alloys and graphite foils. The temperatures applied to the hot side of the TE foils were up to 625°C. Temperature differentials of multiples of 100°C (ΔT=100, 200…600°C) were used for testing the materials. The TE materials tested were in foil form usually 200-500μm thick, 0.5-1cm wide and 5-10cm long. The pure silver reference material was in wire form, 100μm in diameter.

The Seebeck coefficient testing was performed in a manner that resembles the operation of a thermocouple. The sample metal and a reference metal are

connected at one end and the contact is coated in silver epoxy to ensure good electrical connection. The testing sample is then inserted into the heated chamber. Thermocouples are placed near both ends of the sample strip to get an accurate measurement of the temperature differential. The temperatures of both sides of the TE material are recorded along with the voltage output by the sample/reference wire couple. All temperature and voltage data were collected with an Agilent 34970A Data Acquisition Switch Unit (DAQ) with an Agilent 34901A 20 Channel Multiplexer.

All metals exhibit some thermal emf as a result of the Seebeck effect, therefore the emf from the reference material must be subtracted from the overall output in order to get the true output of the sample material. Figure 15 illustrates the Seebeck testing method in detail.

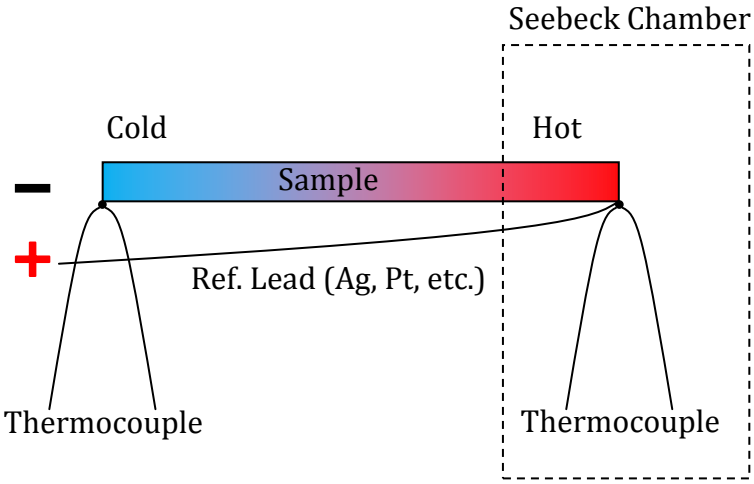

Figure 15: Seebeck Testing Methodology

Elemental Analysis of TE Materials

Samples of available TE materials were subjected to elemental analysis utilizing a field-emission scanning electron microscope (FE SEM). The qualitative elemental composition was determined by energy dispersive spectroscopy (EDS) to determine potential impurity and minority alloy agents.

EDS works by impinging high-energy electrons (protons or X-rays are also used) at the material being investigated. The beam enters the electron bands of the individual elements within the sample. The excitation caused by the beam then "kicks" an electron out of the band and creates a space or "hole" in the valence band of the atom's electron cloud. This creates a potential energy imbalance in the atom's electron cloud. When the electron moves back down to fill the hole, it emits a certain wavelength of X-rays due to the energy released from going down a step in the valence band of the atom. This wavelength is unique for all elements in the periodic table. An X-ray detector takes the emitted X-rays and correlates them with their characteristic elements.

X-ray diffraction was utilized to determine the crystal structure and phases present in the material. Through the bombardment of a sample of material with a known monochromatic wavelength of X-rays at various known angles, a detector picks up the X-rays that diffract on the sample and measures the angle at which the X-rays interfere constructively. These angles based on the atomic packing of the materials, like the X-rays emitted in EDS, are characteristic of individual crystal structures and phases. The refraction data is then compared to a database of known

profiles to look for matches. XRD was used to determine the composition and phase of unknown samples.

Samples to be tested in the FE SEM were mounted in a thermoset epoxy and allowed to cure. After curing, the now mounted samples were sanded and polished to a fine surface using 1200 grit SiC sandpaper. The samples were etched with nitric acid for 15-30 seconds to expose grain boundaries on the surface for optical and SEM imaging.

SEM requires that the sample be conductive to avoid the buildup of excessive charge during imaging. A gold film was sputter coated onto the surface of the sample for SEM imaging. Graphite ink (Ted Pella #16053) was painted on the sides and bottom of the mount to finish the electron pathway to the base of the sample holder. Samples for XRD were pulverized in an aluminum oxide mortar and pestle and scanned from 15 to 70 degrees.

Cooling TE elements used in the SSP were examined using SEM and EDS. It was desired to look at the surfaces of the dice to determine the condition of the silver conductive media used. Figure 16 features two TE dice that were subjected to SEM and EDS analysis

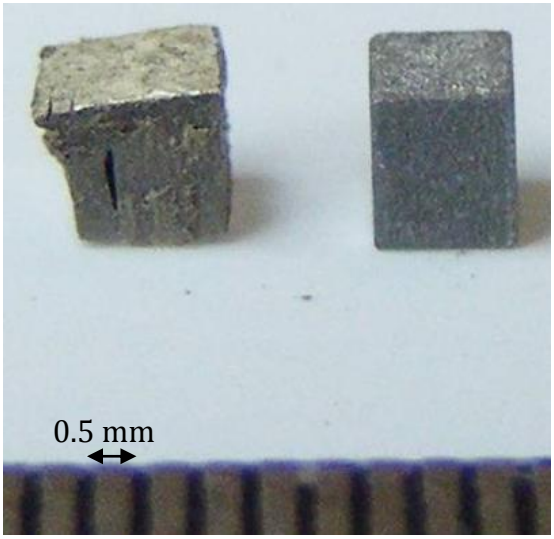

Figure 16: Fractured TE Cooling Die

The fractured TE cooling die was mounted in epoxy and prepared for SEM and EDS analysis. The surfaces of a used and an unused TE die were examined and compared. Silver contact medium adhesion and quality were investigated, as was the structure of the fractured die.

High Temperature Testing

Several tests were performed on the insulation material candidates in order to determine their suitability for use within the TE heat exchanger.

Binder Curing

The organic-based insulation materials tested for use in the TE heat exchanger were known to outgas at elevated temperatures. Due to this fact, the material candidates were tested at different temperatures and various dwell times.

A small sample was inserted into a Thermolyne® 48000 lab furnace with controlled heating and dwell cycles. The outgassed sample was then qualitatively inspected for pliability, strength and durability.

Thermogravimetric Analysis

The insulation materials were also subjected to thermogravimetric analysis (TGA) in order to determine how their mass changes with respect to high temperature environments. The TGA used for this work was a Linseis L81 TGA/DTA. A TGA is a high-temperature mass balance that can very accurately sense minute changes in a sample's mass. A sample is placed in the TGA's sample crucible and the microgram sensitive scale is zeroed out. An oven is then lowered around the sample and crucible and the chamber is heated. This data was used to investigate the amount of mass lost or gained due to a thermal process (combustion, oxidation, reduction, etc.) A sample TGA (along with an accompanying DTA) is shown in Figure 17.

Differential Thermal Analysis

Another component of the Linseis L81 was the differential thermal analyzer (DTA). The DTA consists of two thermocouples, one that is in contact with the bottom of the sample's crucible and another that is in contact with a control sample's crucible (typically Al_2O_3). The voltage output by each thermocouple is measured and recorded. The two thermocouple voltages are then compared to evaluate the heat flow in/out of the specimen.

The control sample is typically inert so little change will occur as a function of temperature. When an exothermic (i.e. combustion) or endothermic (i.e. melting) reaction occurs within the sample, heat is released from or absorbed into the sample. When a difference between the two thermocouple voltages is observed, it can be correlated to either type of reaction, both qualitatively and quantitatively. A sample DTA is shown in Figure 17.

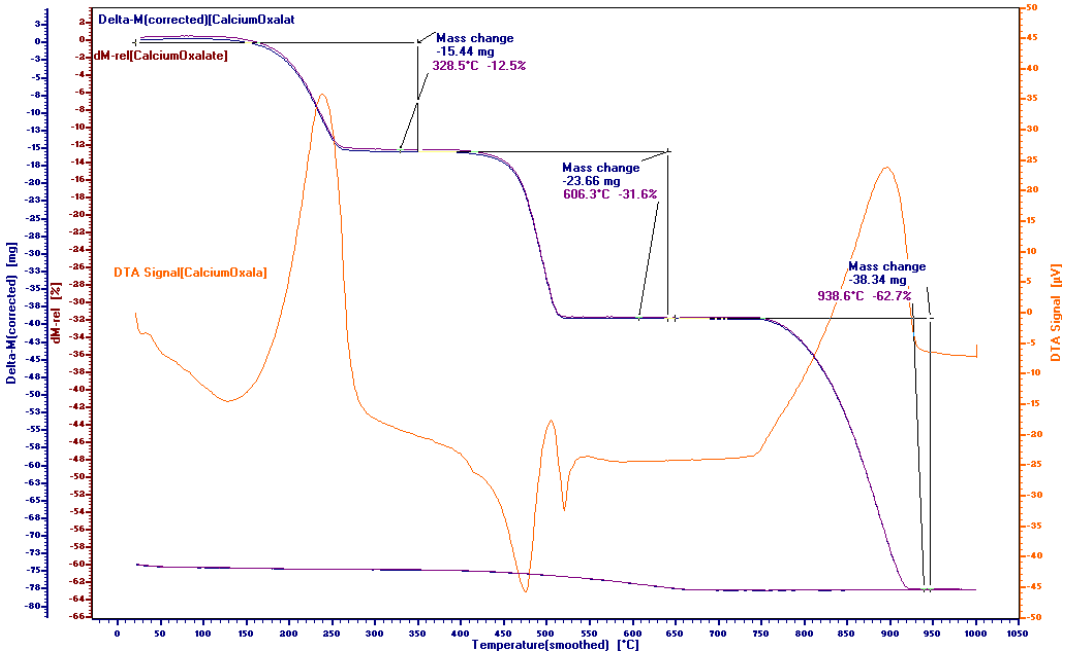

Figure 17: TGA and DTA Data for Calcium Oxalate Control Test.

Figure 17 features the data from a control test performed on a typical control sample, calcium oxalate monohydrate ($CaC_2O_4+1H_2O$). The sample of calcium oxalate was weighed and then loaded into the TGA/DTA. The temperature profile was loaded to the software and the test was run.

Dilatometry

The dimensional stability of the insulation specimens was determined by dilatometry not only to examine the effects of binder burnout, but also effects of compression under static load. The dilatometer measures minute changes in an axial direction as a function of increased temperature.

The dilatometer is most commonly used to measure the CTE of a specimen. The dilatometer is comprised of a heated chamber inside of which is the sample fixture. The fixture consists of two parallel plates made of alumina, one of which is rigidly fixed and the other is connected to a LVDT (linear variable differential transformer). The equipment used for this test was a Linseis L75 Dilatometer.

A sample of insulation was inserted into the test fixture and a small pre-load (~300mN) was applied by the machine to ensure proper placement. An insulated heating chamber was then lowered around the sample and heat was applied under a 200mL/min flow of dry air.

For the TN-9045 dilatometer test, the chamber was heated to 350°C at a rate of 5°C/min in which 350°C was maintained for three hours. The heat was removed and the chamber was left to cool to ambient temperature. The three hour dwell was meant to mimic actual operating conditions that the insulation material would undergo during TE module testing.

Liquid Operating Fluids

Testing Equipment

Liquid engine coolant was investigated as a possible heat transfer medium for the TE module. On this basis, the electrical stability of contacts and fin materials was evaluated in an ethylene glycol-based system. A sample of equal parts of Prestone Extended Life Antifreeze/Coolant and distilled water was taken. The testing apparatus shown in Figure 18 was constructed twice using two different aluminum fin materials.

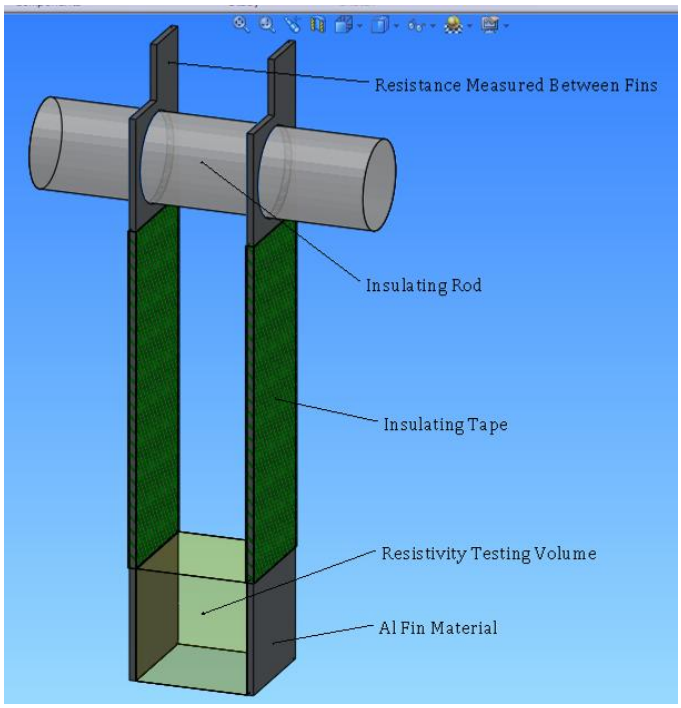

Figure 18: Liquid Resistivity Tester

A hot-plate was used to heat the liquid and a K-type thermocouple was used to measure liquid temperature. The temperature and resistance were measured using the Agilent DAQ at a sampling rate of 1Hz.

Testing Procedure

The testing apparatus was suspended in the necessary amount of solution. The resistance through the liquid and the temperature of the liquid's temperature were recorded over the range 25-100°C. The resistance was then converted to resistivity using the following equation.

$$\rho = R \cdot A / l \tag{10}$$

Where ρ is the resistivity of the liquid (Ω-cm), R is the recorded resistance (Ω), A is the cross-sectional area of the measurement volume (cm^2) and l is the distance between aluminum electrodes (cm). The testing equipment is shown in Figure 19.

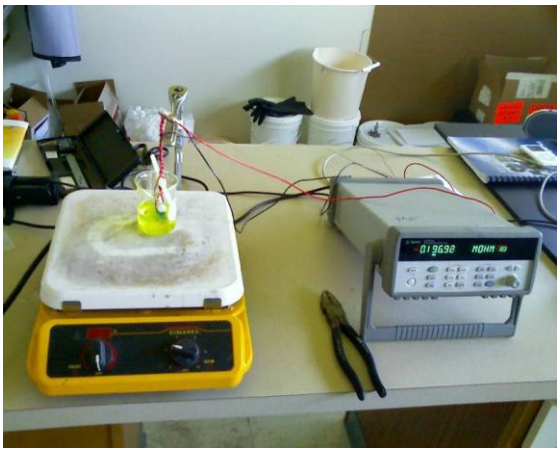

Figure 19: Engine Coolant Resistivity Testing

CHAPTER 4

APPLICATION TESTING PROCEDURES

Pressure Testing

Uniaxial Press

The main purpose of the uniaxial press was to subject materials, namely insulation materials, to high pressures to determine their response as a function of time and temperature.

Press Design: An existing uniaxial press frame was retrofitted with a new hydraulic jack. The jack was a 9kN bottle jack model 76412G from NORCO Industries featuring a threaded outlet port for internal pressure measurement. An electronic pressure transducer (Omega Engineering model PX309-10KG5V) was installed into the outlet port on the jack in lieu of a traditional Bourdon gauge due to the enhanced data collecting capabilities offered by the electronic transducer. The electronic pressure transducer featured a 0-69.0MPa input with a corresponding linear 0-5VDC output yielding a sensitivity of 13.8MPa/1VDC. The transducer utilizes a silicon strain gauge sensor array that outputs a DC voltage through resistive bridge circuitry. The transducer required external DC voltage excitation within the range of 9-30VDC. A small fitting known as a snubber was installed onto the inlet of the transducer to slow down fluid flow, thus preventing pressure spikes from damaging the sensitive silicon strain gauge array. The snubber, model PS-4D

from Omega, is essentially a small fitting containing a porous metal disk. The DC voltage source used was an AC/DC rectifier with a variable voltage output or a fixed 16 VDC power source scavenged from a computer printer. Data from the press was collected utilizing the Agilent DAQ as shown in Figure 20.

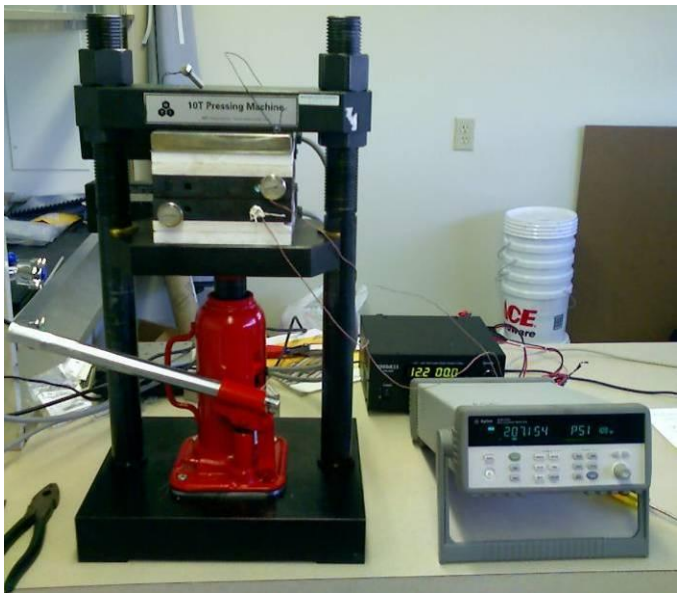

Figure 20: Updated Uniaxial Press System

Testing Procedure: The transducer was powered with DC voltage and let to warm up per the manufacturer's instruction. The transducer's output leads were then connected to the Agilent 20 channel multiplexer that was installed into the DAQ. The DAQ's computer interface and data collection software allowed for the voltage output by the transducer to be mathematically converted to pressure using the 1VDC/13.8MPa sensitivity value. Samples were then set into place between the top and bottom plates of the press and it was manually operated using the hand

pump on the side of the jack. The pressure was raised to the desired pressure to observe thickness decay as a function of time and temperature.

Insulation Testing: Three different types of gasket testing were performed with the uniaxial press. Pressure Test A consisted of placing a piece of insulation, either outgassed or not, into the press. The sample was then loaded to a desired pressure value. The pressure was maintained for 10-15 seconds and then it was released. The sample was removed and its thickness was measured using a KD Tools 3756 digital caliper. Next, the sample was put back into the press and loaded to the next desired pressure and the cycle was repeated.

Pressure Test B was performed in much the same way as A, except that the insulation thickness was measured while still under pressure in the uniaxial press. This was done by loading the sample to the desired pressure and using a Craftsman 40811 automotive feeler gauge set to find the thickness of the sample. The correct combination of gauges was used to find the thickness between the top and bottom plates of the press. The feeler gauges were then measured using the KD Tools digital caliper to determine the thickness of the sample at the applied pressure.

Pressure Test C was performed quite differently than the previous two. In this test, a spare TE die was inserted into a hole cut into a piece of insulation material. The insulation and die were then loaded to the desired pressure and held for 10-15 seconds. The pressure was then released and the die was removed. The die's height in the direction of the load was measured with the KD Tools digital caliper. The die's final height was directly representative of the gasket's thickness at

the pressure seen due to the fact that the mechanical properties of the TE dice are such that they deform plastically with very little elastic return. The strictly plastic deformation is due to the slipping of crystallographic planes of the dice as failure/fracture occurs.

Electroplating

Nickel was plated onto the electrical contact areas of the aluminum and copper heat exchanger fins. The nickel layer prevents the Al and Cu from oxidizing in the high temperature environment seen by the TE heat exchanger, maintaining proper electrical connection between the TE elements and the conduction fins.

Plating Equipment

Two different plating systems were used for contact plating within the TE heat exchanger. A copper strike coating bath known as Flash Copper ™ from Caswell Inc. was used as a base for a nickel coat. The copper plating bath used was a proprietary blend of aqueous copper sulfate and other chemicals. The nickel plating bath, also from Caswell, Inc. was a Watts type bath which is an aqueous solution of nickel sulfate, nickel chloride and boric acid. The Watts bath may also contain organic brighteners and levelers that fill in imperfections and help make the plated nickel more lustrous and ductile. A batch of high strength industrial detergent known as SP Degreaser™ was provided as a means to remove grease and dirt from parts prior to plating. A chemical known as sodium zincate was provided to remove

the natural oxide from aluminum parts and deposit zinc in its place. The zinc layer prevents any further oxidation of the surface of the aluminum.

Both plating baths had individual anodes, low phosphorous copper anodes for the Flash Copper™ and high purity nickel anodes for the Watts nickel bath. Porous fabric bandages were provided with the anodes. The bandages act as a net to catch any unwanted compounds that may be released from the anodes and contaminate the plating baths.

A model Caswell SPC-9250 AC-DC rectifier was purchased from Caswell, Inc. The output capabilities of the rectifier were 0-15VDC and 0-25ADC. Several 300W titanium heaters and thermostats were also provided to aid in maintaining bath temperatures. A pH meter was provided to help maintain the ever-important bath pH. Small amounts of sulfuric acid, nitric acid and ammonium hydroxide were used to raise and lower bath pH when needed.

Since not all of each part was to be plated, a masking tape was procured to cover non-plated areas of the parts. The masking tape used was item number 24-GT-1.5-72 from CS Hyde Co. The masking tape was made of 50μm thick polyester foil with silicone adhesive.

Plating Procedures

Copper Strike Coat Plating: Sometimes a copper strike coat is necessary to achieve a successful nickel plate. This is typically used for decorative finishes because the copper will help fill in voids and gaps and leave a more even surface.

The aluminum parts were thoroughly cleaned in SP Degreaser for 10-20mins at >60°C. They were then thoroughly rinsed with deionized (DI) water. They were then "zincated" in the sodium zincate solution for 10-30sec to remove existing oxide and to prevent further oxidation. Another thorough rinse was performed. The parts were then put into the copper plating bath. The copper plating bath was continuously air-agitated with a submersible tank circulation pump and maintained at 43°C with a thermostat and 300W titanium heater. The aluminum parts were then plated at a current density of 97 amps/m^2 of surface area for 15 minutes. The flash-copper layer would then be immediately plated with nickel as described in the following steps. This step is typically removed when plating strictly for mechanical purposes or corrosion resistance.

Plating Nickel Directly onto Zincated Aluminum: The aluminum parts were masked with polyester tape to prevent plating on unwanted areas. The parts were then cleaned for 10-20 minutes in SP Degreaser heated to >60°C. The cleaned parts were rinsed thoroughly with DI water and then zincated. For functional plating, the nickel was plated directly onto the zincated aluminum. The nickel anodes were covered in individual "bandages" and then fixed on opposite sides of the plating bath and connected in parallel to the positive terminal of the rectifier. The bath was continuously agitated with a submersible fish-tank circulation pump and the temperature was maintained at 43°C with a titanium tank heater and thermostat. The objects to be plated were then inserted and connected to the negative terminal of the rectifier. The objects were plated at a current density of 97 amps/m^2 of

surface area for approximately 15mins. The parts were then removed, rinsed and dried.

Plating Nickel onto Copper: The copper parts were masked with polyester tape to prevent any unnecessary plating. Copper parts were cleaned for 10-20min in SP Degreaser heated to >60°C and then rinsed in DI water. Any surface oxidation was removed via an etching dip in either dilute ferric chloride or nitric acid. Once the parts were etched sufficiently, they were again rinsed in DI water. The nickel anodes, again, covered with their individual bandages, were fixed on opposite sides of the plating bath and both were connected in parallel to the positive terminal of the rectifier. The bath was continuously agitated with a submersible fish-tank circulation pump and the temperature was maintained at 43°C with a 300W titanium tank heater and thermostat. The copper fins were then inserted and connected in parallel to the negative terminal of the rectifier. The objects were plated with a current density of 97 amps/m^2 for approximately 15mins. The parts were then removed, rinsed and dried.

Small-Scale Prototype

The SSP was used to test various design components of the TE heat exchanger. Items tested were fin design and materials, electrical contact materials, and different types of TE elements. The SSP was instrumental in the design

progression of the FDP. The power output, voltage and heat transfer data obtained from SSP testing were also used to help develop numerical modeling efforts.

SSP Components

The entire SSP was fully designed in SolidWorks CAD (computer aided drafting/design) software. Using the CAD models, plates, manifolds, fins and insulation pieces were solicited to fabricators to be cut using CNC (computer numerically controlled) mills, punches and lasers. The fabricated parts were then examined to ensure quality and tolerance.

Endplates and Manifolds: Spark R&D of Bozeman, MT was commissioned to do most of the machining for the SSP. The SSP's end plates and inlet/outlet manifolds were all cut by a CNC mill following CAD models of each part. 9.5mm-thick, 304 stainless steel (SS) plate was used for the end plates. The hot inlet and outlet manifolds were machined out of 304 SS. The cold inlet and outlet manifolds were machined out of aluminum stock. The manifolds and end plates are featured in Figure 21.

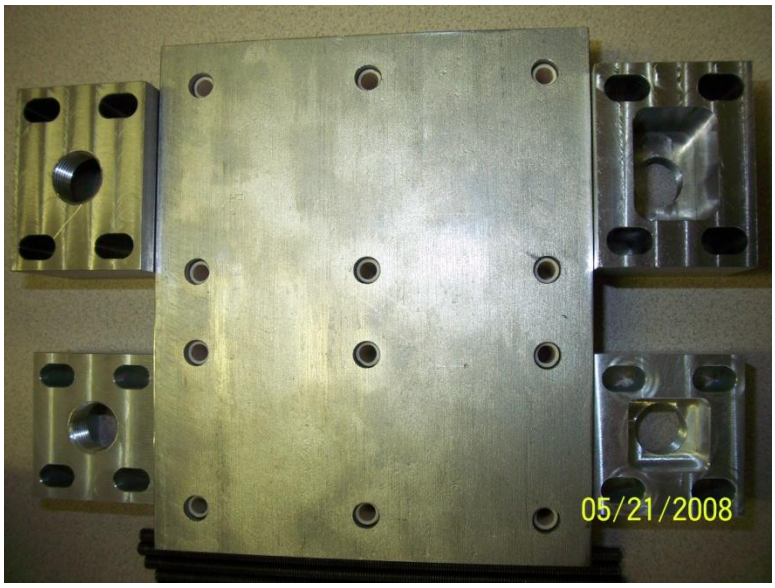

Figure 21: SSP Components

Fins: Several fin materials were investigated for their use in the SSP and the FDP. 580μm thick 1350-O aluminum; 260μm thick 1100-O aluminum; 800μm thick 1100-O Al; and 800μm thick C110 high purity copper were investigated. The final fin material selection was 800μm 1100-O Al for the hot-side fins and 800μm C110 high purity copper for the cold-side fins. The copper fins were required to be cut using the CNC punch because to laser-cut copper requires a great deal of ventilation which was not available with Soares' equipment. Some aluminum fins were cut in the CNC punch and the rest were cut using the CNC laser. The method used for cutting the aluminum was dependent on the complexity of the part; the simple parts were cut with the punch and the complex parts were cut with the laser. The aluminum and copper fins were then electroplated with a ~10μm layer of nickel at their respective contact areas. They were then cleaned and inspected prior to implementation.

Contact Media: Several different contact media were evaluated for their performance in the SSP design. Colloidal graphite, product no. 16053 from Ted Pella, Inc., was investigated as one conductive medium. Three silver-based contact media were also investigated: CircuitWorks®, Product No. CW7100, Silver Conductive Grease; 0.5-1.0μm silver microspheres, Alfa Aesar Stock #41597; and 4-7μm silver powder, Alfa Aesar Stock #11402. The colloidal graphite was composed of graphite flakes suspended in an isopropanol liquid base. The colloidal graphite was painted onto the desired surface where the isopropanol was allowed to evaporate, leaving only a layer of pure carbon. The silver conductive grease was essentially silver powder dispersed in a silicone oil base. It too was simply spread onto a contact area, but the silicone oil did not evaporate. The silver 0.5-1.0μm microspheres and 4-7μm powder were obtained in their dry form. They were dispersed in rubbing alcohol (70%isopropanol/30%H_2O) before being "painted" onto their desired locations. Much like with the colloidal graphite, the alcohol was allowed to evaporate, leaving only a layer of pure silver.

TE Dice: Two different types of TE dice were used. The first type, used in Builds 1-6, was a bismuth telluride-based cooling element, typically used in Peltier solid-state cooling devices. The dimensions of the cooling dice were 1.40mm on each side and 1.62mm tall. The second type, used from Build 7 on, was a bismuth telluride-based power generation element. The dimensions of the power generation dice were 2.04mm on each side and 1.52mm tall.

Internal Steel Spacers: As the design progressed and matured, steel spacers were added to the design. The purpose of the spacers was to aid in keeping the stack robust and evenly compressed, while maintaining as high as possible thermal gradient through the insulation thickness (across the TE elements). The steel spacers for the SSP were CNC laser-cut out of 800μm thick 304 SS to their desired shape.

Insulation: 1.59mm thick Thermo-Tork® TN-9045 gasket material was chosen for the insulation of the SSP and, ultimately, the FDP. The insulation pieces were cut to spec by Die Cut Technologies in Northglenn, CO, using CNC laser equipment. The laser-cutting process employed to cut the insulation materials produced a layer of carbon build-up at the cut edges. The carbon was carefully cleaned from the insulation pieces and they were outgassed to the point that was necessary for the test runs.

Insulation Outgassing: High temperature testing of the insulation material in a non-functional SSP mock-up revealed the need for outgassing prior to implementation. It was determined that the most practical outgassing procedure was to heat an entire build's worth of insulation pieces in a lab oven to the desired temperature and then dwell for a desired time. The outgassed pieces were then allowed to cool before being implemented in the SSP. Builds 1-9 all used outgassed insulation materials.

Grafoil: The available cooling TE dice were taller than the thickness of the TN-9045 insulation; therefore, layers of Grafoil® were added to effectively "thicken" the insulation. Grafoil® GTB flexible graphite sheet from GrafTech International was used to add thickness to the insulation so that the dice would not be crushed under the pressure exerted by the through rods. The thickness of Grafoil chosen for this application was 127μm. A piece of Grafoil was cut to the desired shape and placed on each side of the dice-cluster containing insulation. Grafoil was used in SSP builds 3-6.

Compression Rods: #10-32 threaded titanium through rods were procured and cut to the desired length. Upon further testing, it was desired that custom titanium through rods were required. The purpose of the through rods was to compress the stack to facilitate and maintain good electrical contact between the TE elements and conduction fins. Various hardware components (nuts, washers, etc.) were also collected. Alumina tubes with an internal diameter of 4.83mm and an outer diameter of 7.11mm were used as electrical and thermal insulation between the internal components of the SSP and the #10-32 titanium through rods. SS Belleville washers were also used the design of the SSP. The following figure features the #10-32 titanium rods, alumina tubes and #10 SS Belleville washers used in the SSP.

Figure 22: 10-32 Titanium Rods, Al_2O_3 Tubes and #10 SS Bellevilles

It was eventually discovered that the #10-32 titanium rods were not strong enough to handle the torques necessary to produce the desired internal pressures of the SSP. Larger ¼-28 titanium rods were designed and custom ordered. No high temperature insulating tubes could be found that would fit over the rods and still fit inside the 7.14mm holes cut in the SSP plates, fins and insulation pieces. It was decided that anodized aluminum tubes could be used to insulate the conductive internal components from the through rods. 3003 grade aluminum tubes, 7.14mm outside diameter and with a 0.359mm wall thickness were selected for this purpose. The tubes were cut to the desired length and were anodized by Spark R&D.

Belleville Spring Washers: Special spring washers known as Bellevilles were ordered to the desired specifications for use with the SSP. The Belleville washers were employed to retain pressure on the stack when internal components expand and contract as a result of thermal expansion and contraction. Bellevilles made of 300 series SS and the superalloy, Inconel X-750, were used.

Heat Dissipation Washers: Finned heat dissipation washers were designed and fabricated. Three different materials were chosen: 1018 steel, 304 SS and 5051 Al, all at 710μm thick. Their sole purpose was to keep the temperature of the Bellevilles low in order to help prevent thermally induced creep. Figure 23 features the CAD model used for the fabrication of the heat dissipation washers. These were also fabricated with the CNC laser at JE Soares, Inc.

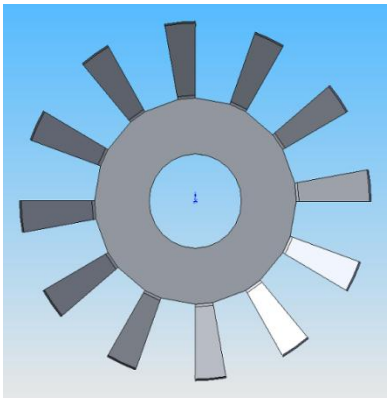

Figure 23: Heat Dissipation Washer CAD Model[1]

SSP Assembly

After all parts and components were ready, the stack was constructed and installed into a testing apparatus used to simulate conditions that would be seen by the FDP, only on a smaller scale. The figures below feature a comparison between using the #10-32 titanium rods vs. the ¼-28 titanium rods in the SSP.

[1] CAD model by Nik Sorenson

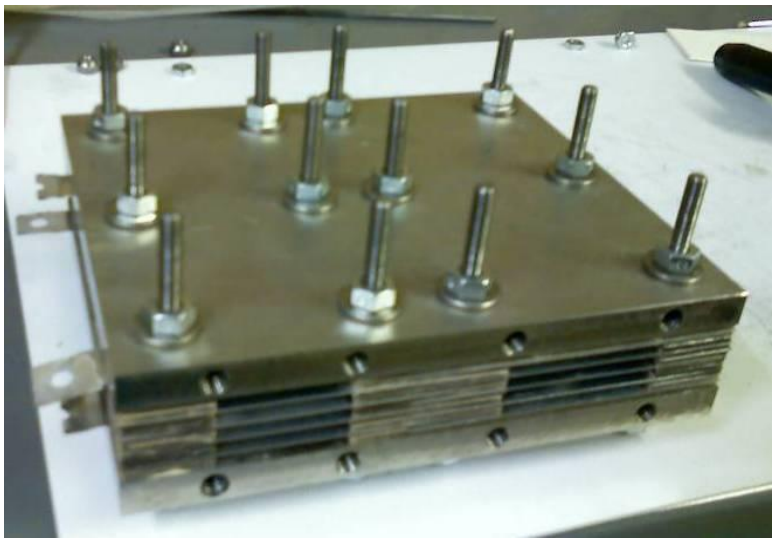

Figure 24: Fully-Assembled SSP with 10-32 Titanium through Rods

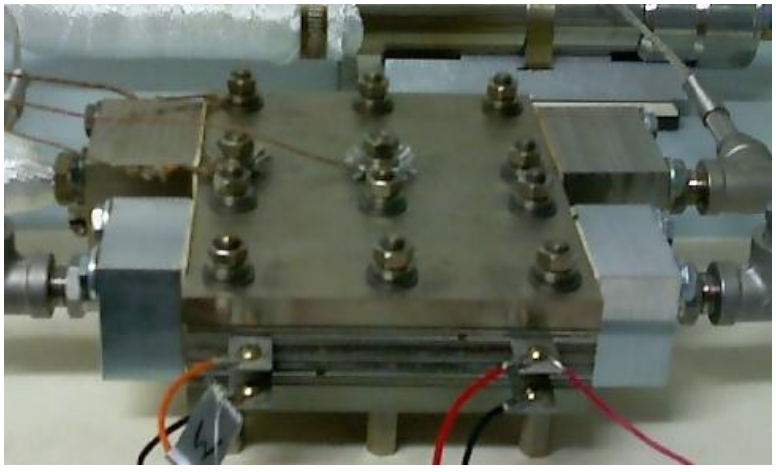

Figure 25: Fully-Assembled SSP with ¼-28 Titanium through Rods

The through rods were tightened to specified torque values using a Craftsman Microtork, torque wrench, model #44593. Figure 26 is a view of the top of the SSP. The numbers represent the sequence of the torquing pattern used to compress the SSP.

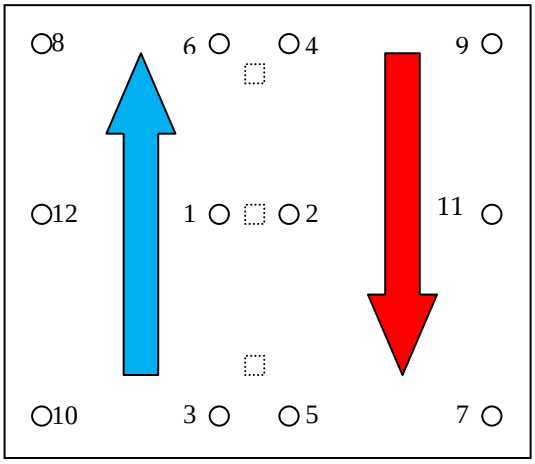

Figure 26: SSP Rod Torque Pattern

This torque sequence was used for all SSP builds. It was repeated until rods were all equal torque. The arrows represent the direction of fluid flow; blue for the cold and red for the hot. The TE dice locations are displayed by the dotted squares.

SSP Test Rig and Instrumentation

A test rig was developed as a means to impose a controllable thermal gradient within the SSP. It featured a 1000W inline heater, two Alita AL-150 air pumps with an Omega Engineering model FL-2061 flow meter for each and the necessary hardware and fittings to complete the test rig's construction. The test rig was assembled on a mobile cart to aid in construction and troubleshooting. Stainless steel (SS) fittings and pipe-plug thermocouples were procured so as to measure the temperatures in and out of the SSP. Figure 27 shows the components of the SSP testing rig.

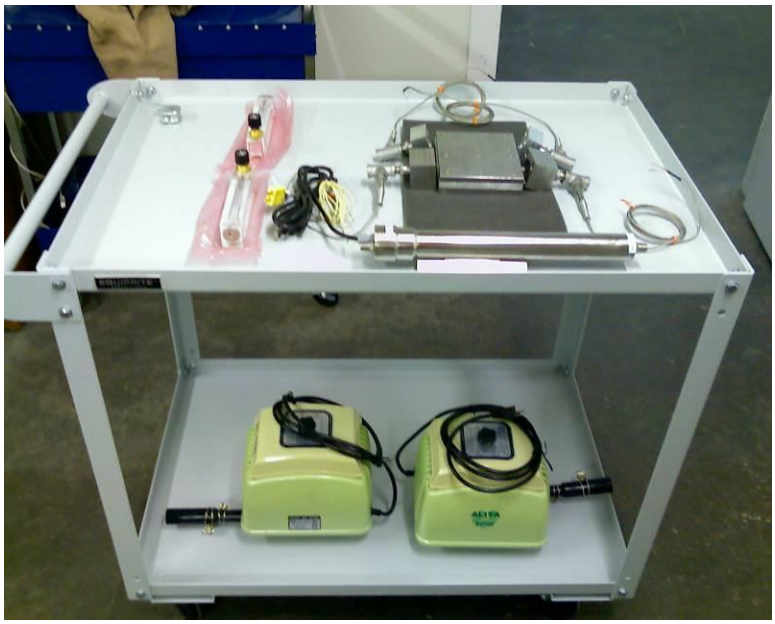

Figure 27: SSP Testing Equipment

SSP Testing

The Agilent DAQ was set up in such a way as to measure voltages output by the SSP. A PROVA CM-05 current clamp was used to measure electric current produced by the SSP under resistive load conditions. Figure 28 features the entire SSP test rig while a load test was being performed. The computer and DAQ are visible at the left of the picture, the air pumps and their respective flow meters can be seen on the bottom right and the SSP is in the top middle. An Agilent U1252A handheld DMM (digital multimeter) and a Hewlett Packard 34401A bench top DMM were also used to make voltage and resistance measurements when necessary. A high precision LOM-510A micro-ohmmeter from IET Labs was used for making highly accurate IR (internal resistance) measurements.

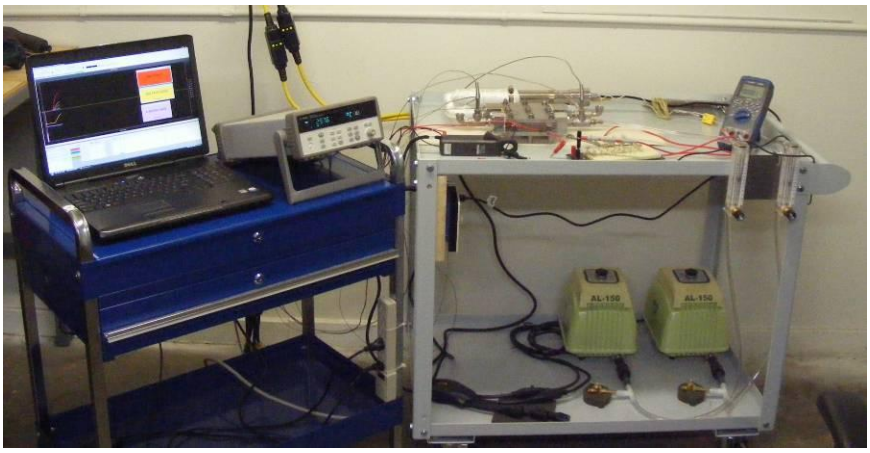

Figure 28: SSP Load Testing

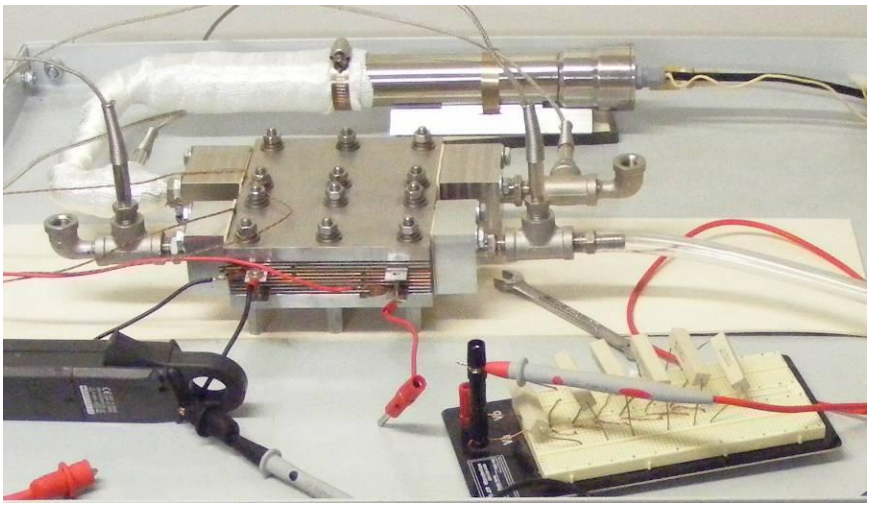

Figure 29: Close-Up of SSP and Resistive Load Bank

SSP Performance Testing

Testing Equipment

Internal resistance of the stack was continuously measured while stack was being compressed. The Agilent U1252A handheld DMM was used for IR measurements in Builds 1-7 and the IET Labs LOM-510A micro-ohmmeter with 4-probe Kelvin test leads was used in Builds 8 and 9. The Agilent DAQ was used to

collect SSP output voltage data as well as fluid temperatures in and out of the stack. Under resistive load conditions, the current output of the SSP was measured with a PROVA CM-05 DC current clamp. The current clamp featured analog DC voltage output with a sensitivity of 100mV/ADC. The current clamp data was also collected using the Agilent DAQ. BenchLink Data Logger 3 software was used to collect SSP performance data.

Non-Functional Build

The SSP was initially constructed as a non-functional mock-up. This build was aimed at investigating the high temperature performance of the individual SSP components. The SSP mock-up was assembled without any TE elements. The hot and cold fins were both constructed of the 580μm 1350-O aluminum sheet and the gaskets were of the ThermoTork® TN-9045 insulation material.

The SSP mock-up was subjected to inlet air temperatures of 430°C. Information gathered with this build prompted the pre-construction binder outgassing procedures of the internal gaskets. Functional variants of the SSP were constructed 9 different times. The following are technical construction aspects of each build.

Build #1: 3/27/09–4/6/09

TN-9045 insulation material was chosen as the gasket material. The pieces were cut off site. They were then outgassed for 2 hours at 375°C. 36 TE cooling dice

were used in all. This build featured an alternating P/N pattern of 18 series sets of two dice in parallel.

Circuitworks® Silver Conductive Grease was used as a lubricant/electrical contact on the surfaces between the TE dice and conduction fins. 260μm thick 1350-O aluminum sheeting was used for the hot and cold fins. The fins were cut to spec by JE Soares Inc. of Belgrade, MT using their CNC laser sheet metal cutter.

#10-32 threaded titanium rods were used to compress the stack. The through rods were torqued to 3.39N-m and the stack was run in its test rig. The rods were then re-torqued to 5.08N-mand the stack was run in its test rig again.

The hot air volumetric flow rate was 144L/min and the cold air flow rate was 177L/min, both measured at ~45°C. These flow rates yielded typical air temperature values of 380°C and 260°C for the hot inlet and outlet, respectively; and 50°C and 70°C respectively for the cold inlet and outlet. These flow and temperature regimes were used throughout Builds 1-3. Build 1 was run twice for a total of 2 hours.

Build #2: 5/29/09–6/7/09

The insulation pieces for Build 2 were outgassed at 375°C for two hours. A total of 162 cooling dice were used in Build 2. They were arranged an alternating P/N pattern of 18 series clusters of 9 dice in parallel (3x3 clusters).

Custom-made ¼-28 thread titanium rods were procured and used throughout the rest of the SSP builds. The hot fins used were made of 800μm 1100-

O aluminum sheet and the cold fins were of high purity copper sheet, also at 800μm thick. Fins of this type were also used throughout the rest of the SSP builds.

Build 2 initially featured a piece of Grafoil GTB on each side of the dice-containing insulation. The rods were torqued to 5.08N-m. The stack was not run in the test rig. It was disassembled and the Grafoil was removed from both sides of the insulation. Also, while the stack was disassembled, thermocouples were installed internally; one on a hot fin near the dice contact and one near the contact on a cold fin. The thermocouples were used to measure the temperature differential of one dice cluster. This temperature differential was used to determine the Seebeck coefficient of the TE dice. The stack was then reassembled and torqued to 1.695N-m whereas the internal TE dice were heard cracking. The stack was hooked up to the test rig and run once for 1 hour.

Build #3: 6/8/09–6/10/09

The insulation pieces from Build 2 were re-used in Build 3. 162 new cooling dice were used in Build 3 in the same way as Build 2. Al and Cu fins from Build 2 were re-used. Colloidal graphite was painted on both sides of TE dice clusters. Silver conductive grease was spread onto the conduction surfaces of fins. Grafoil was placed on only one side of the dice-containing insulation.

The rods were torqued incrementally to 1.695N-m. The SSP was then allowed to sit over night. The next day, the rods were re-torqued to 1.695N-m. The top nuts were removed one-by-one and a stack of 3 parallel SS Belleville washers were placed onto the rods. All rods were re-torqued to 1.695N-m. The module was

run two separate times for a total of 3 hours. A resistive load bank constructed of 1Ω and 0.47Ω power resistors was used to load the SSP to test its output power.

Build #4: 6/15/09–6/30/09

The insulation pieces for Build 4 were outgassed at 350°C for 1 hour. New aluminum and copper fins were used. The colloidal graphite was discontinued from use. The silver conductive paste was spread onto fin contacts and TE dice surfaces. The SSP was reassembled with the insulation and Grafoil from Build 3 and torqued to 1.695N-m and 3 parallel SS Bellevilles per rod were used.

Thermocouples were again used to measure the temperature difference across one dice cluster. A new load bank consisting of an array of 0.05Ω power resistors was used to load the SSP.

The hot side air flow rate was slowed down to 93.5L/min in order to increase the inlet temperature of the hot gas. This yielded the following air temperatures: hot inlet ~480-500°C, hot outlet ~270°C, cold inlet ~50°C and cold outlet ~65°C. The hot air flow rate was slowed down to effectively replicate the temperature of the exhaust gas exiting the Honda Genset's engine. This flow rate and temperature were used throughout the rest of the SSP builds. Build 4 was run 5 separate times for a total of 14.5 hours.

Build #5: 7/17/09–7/29/09

Build #5 used the same dice and insulation pieces from Build #4. The hot side aluminum fins were re-used but new, freshly plated copper fins were used on

the cold side. The same SS Bellevilles, Grafoil pieces and aluminum fins were used from Build #4.

The rods were torqued to 1.695N-m. Small wave washers were installed below the Bellevilles in an effort to help keep them cool. A thermocouple was installed on the bottom of one Belleville stack to determine what temperature it was seeing during operation. The stack was run in the test rig. Build 5 was run 4 separate times for a total of 10 hours.

Build #6: 8/3/09–8/31/09

Build 6 re-used the dice and insulation pieces from Builds 4 and 5. It also used the same Grafoil pieces and aluminum and copper fins. New Inconel X750 Belleville washers were used. Three were installed in parallel onto the through rods.

The 0.5-1.0μm silver microsphere powder was used as contact medium. The silver powder was dispersed in rubbing alcohol and painted onto the surfaces of the dice clusters as well as the contacts of the fins. The rods were torqued to 2.26N-mand the stack was run once for 2hours 20min.

Build #7: 8/31/09–9/18/09

72 power generation dice were used. They were arranged in 18 series clusters of 4 parallel dice (2x2). Grafoil was discontinued from use. One insulation piece broke from handling and was replaced with a freshly outgassed one. The rest of the insulation pieces, fins, and Inconel Bellevilles were re-used.

Three different silver contact materials (silver conductive grease, 0.5-1.0μm silver microspheres and 4-7μm silver powder) were used on the three individual stack columns. The paste was painted onto the dice and fins and the two powders were dispersed in rubbing alcohol and painted onto their respective dice and fins. All three contact media were used as a way to compare benefits/detriments associated with the use of each. The stack rods were torqued to 1.13N-m. The Bellevilles were installed as before and the rods were torqued to 1.695N-m.

The SSP was run once for 4 hours. Heat dissipation washers were then added to the design to be evaluated for their effectiveness. Two sets of three dissipation washers were placed onto two of the rods on the hot side of the SSP. The stack was run again for 1hour 45mins. Heat dissipation washers were then used in different configurations and with different materials from this point on.

Build #8: 9/18/09–10/20/09

72 new power generation dice were used. All new, outgassed insulation pieces were used. Only the 4-7μm silver powder was used as contact medium. Heat dissipation washers were again used to evaluate the potential of keeping the Bellevilles cooler. The LOM-510A micro-ohmmeter from IET Labs was used from this point on for making IR measurements.

Build 8 was run once for 5hrs 50mins. Results from this test prompted an investigation into the silver contact material. The entire SSP was put into a lab oven at 300°C for 8 hours. The IR of the stack was monitored over the length of the test. The SSP was run twice after the oven test without any notable modifications having

been made to the module. Modifications to the load bank were, however, made between test runs 2 and 3 of Build 8. The 0.05Ω metal oxide power resistors were removed and replaced with lengths of solid-core copper wire. Build 8 was run a total of 3 times for a total of 9hours 40mins.

Build #9: 10/20/09–11/3/09

All new power generation dice were used. The insulation, fins and Bellevilles from Build 8 were re-used. For Build 9, no internal contact media were used. Heat dissipation washers were used for all tests of Build 9. The material type and location of the washers were alternated between the tests in order to get a large amount of comparable data.

Many tests of Build 9 featured thermal cycling, wherein the heat was applied to the module until it had reached steady-state power output then the heat was turned off and the module was allowed to cool. After the module was relatively cool, the heat was applied again. This heating/cooling cycle was repeated several times over the length of the tests. The IR of the stack was measured and recorded between tests to monitor any changes. Build 9 was run 8 separate times for a total of 36hours.

Honda ES6500 Genset

A Honda ES6500-K2 model genset was procured as a test bed for the practical application of the FDP. The genset was powered by a Honda GX360-K1 two-cylinder, four-cycle internal combustion engine, rated at 9.6kW at 3600rpm.

The ES6500 featured a liquid cooling system and aftermarket modifications that enabled the genset to be powered by either liquid gasoline or gaseous fuels such as propane or LPG (liquefied petroleum gas). The genset had an electrical power generating capability of 6.0kVA continuous with a peak output of 6.5kVA, rated while running on liquid gasoline. The genset output 120/240VAC and could provide continuous currents of 50/25AAC, respectively. The following is a picture of the ES6500 as it was received for this project.

Figure 30: Honda ES6500 Genset

The aftermarket LPG fuel conversion can be seen in the top-right picture. Another important feature of the ES6500 is its mobility. The genset featured a wheeled chassis, making it mobile and easily maneuvered. The following figure features the physical dimensions of the ES6500.

Table 4: Honda ES6500K2 Physical Dimensions (Honda 2002)

Model	**ES6500K2**
Length	1.15m
Width	0.710m
Height	0.680m
Dry Weight	124kg

Genset Instrumentation

Cooling System: Radiator air inlet and outlet temperatures were measured with model 5TC-GG-K-24-72 thermocouples from Omega Engineering. One was suspended in the front of the radiator to get the air temperature immediately before it enters the radiator and the other was suspended immediately after the radiator fan to read air outlet temperatures.

The liquid inlet and outlet lines of the radiator were retrofitted with copper fittings and in-line thermocouples. Pipe-plug thermocouples, model TC-K-NPT-G-72 from Omega Engineering were installed into threaded copper fittings. An example of the pipe-plug thermocouple fitting is shown in Figure 31.

Figure 31: Pipe-plug Thermocouple and Fitting

A model FP7002A paddle-wheel type flow meter from Omega Engineering was selected to measure the flow of engine coolant through the radiator. The flow

meter is featured in Figure 32. The flow meter also featured temperature measurement via an RTD (resistance temperature detector). Figure 33 features the inlet side of the radiator with flow meter and in-line thermocouple visible.

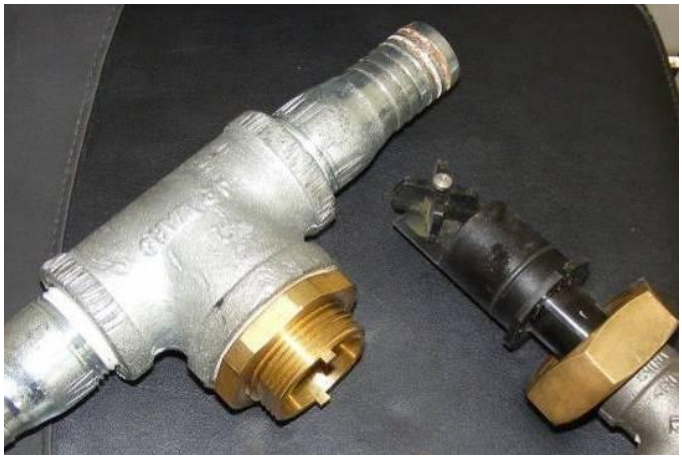

Figure 32: Model FR7002A Paddle-Wheel Flow Meter

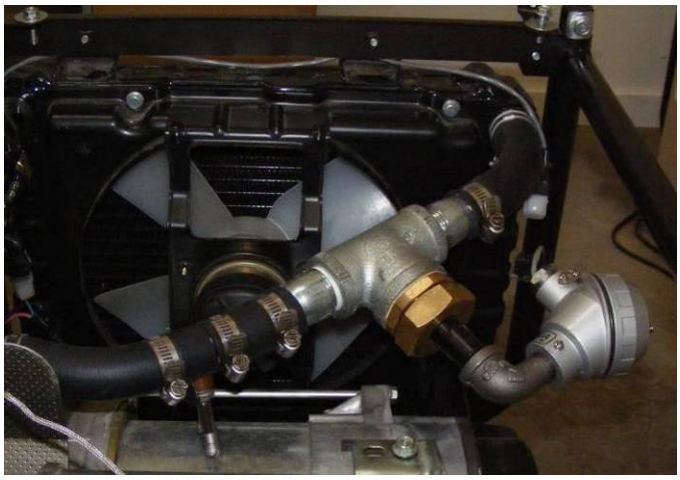

Figure 33: Coolant Flow Meter and Thermocouple at Radiator Inlet

Radiator Fan: The radiator fan's voltage was measured directly with a channel on the Agilent DAQ. The electric current drawn by the fan was measured

using a PROVA CM-05 DC current clamp. The voltage and current data were used to determine the power drawn by the fan.

Exhaust System: The exhaust system was monitored using several different means. Simple welded bead thermocouples, model 5TC-GG-K-24-72 from Omega Engineering, were used to measure the surface temperature of the muffler inlet, the surface temperature of the exhaust outlet and the temperature of the exhaust fluid exiting the muffler. A hole was drilled in the top of the muffler's inlet pipe. A threaded fitting was welded over the hole so that a TC-K-NPT-G-72 pipe-plug thermocouple could be installed and used to measure the temperature of the exhaust fluid entering the muffler. Figure 34 shows the welded fitting and thermocouple.

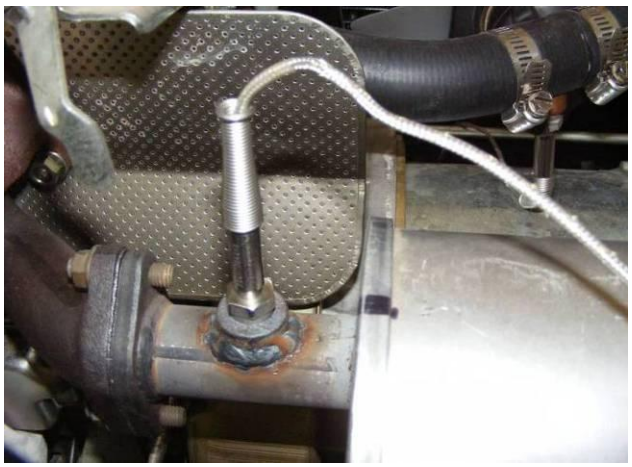

Figure 34: Thermocouple at Muffler Inlet

Exhaust back pressure exhibited by the muffler was also measured. This was done through the same welded fitting as was used for temperature testing. The pressure was measured using a PX309-001G5V pressure transducer with a PS-4G

snubber, both from Omega Engineering. The transducer was powered using the same means as was used with the uniaxial press's transducer. The transducer had a range of 0-6.90kPa (gauge pressure) and output a range of 0-5 VDC linearly dependant on pressure (1.379kPa/VDC). A 10.2cm long 304 SS pipe nipple and a ball valve were installed before the transducer and snubber. The nipple was to isolate the transducer from the heat of the exhaust and the valve was used to protect the transducer from pressure spikes that may have occurred as the genset was run. The stock exhaust muffler and pressure transducer are featured in Figure 35.

Figure 35: Stock Muffler with Pressure Transducer

Honda ES6500 Genset Modifications: The Honda ES6500 was fully instrumented in its stock form to successfully characterize its performance. The repercussions of any changes made to the genset would then be easily seen in

performance changes. The following figures feature the fully instrumented stock genset.

Figure 36: Instrumented Stock Honda ES6500

Figure 36 shows the ES6500 in its instrumented stock form. The LPG fuel conversion adapter is visible on the top-right of the picture.

Figure 37: Instrumented ES6500 with Panels and Fuel Tank Removed

Eventually, structural and functional modifications were made to the genset. The gasoline fuel tank, stock muffler and all external panels were removed. Their removal was prompted by the space requirements of the FDP. A flanged steel tube was fabricated to attach the FDP to the stock exhaust manifold. The coolant line running from the engine outlet (at the thermostat) to the radiator inlet was lengthened and re-routed above the space needed for the FDP's air shroud. The stock radiator mounts were also altered to move the radiator upward and outward in order to get more direct air flow through the shroud. The following figure illustrates some the changes made to the genset.

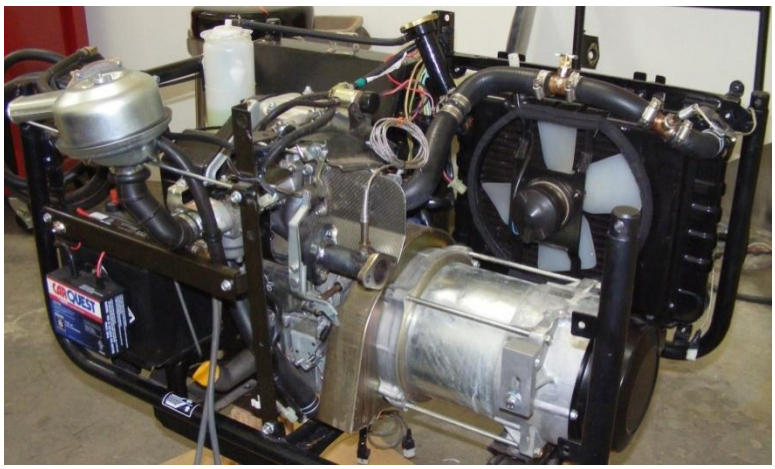

Figure 38: Modified Honda Genset

Figure 38 features the changes made to the exhaust system and the removal of outer panels. The re-routed coolant line can be seen above the radiator fan on the top-right. The exhaust extension tube can be seen in the center of the figure with a thermocouple protruding from it.

Baseline Performance Testing

The baseline performance of the genset was tested and evaluated. The genset in its stock configuration was operated on gasoline and propane for a comparison between fuels. The coolant system temperatures, coolant flow rate, radiator fan power, and exhaust temperatures were monitored.

Fuel Consumption and Efficiency Testing

Fuel consumption rates of the Honda genset were measured at various load conditions. The fuel consumption rates were later converted to energy conversion efficiencies by comparing the amount of fuel consumed to the amount of work done over a certain period of time. The fuel consumption rates were measured by taking the propane tank's mass before and after running the genset for a known amount of time. The mass change per unit time was then calculated as the fuel consumption rate. The mass of the tank was taken using an Ohaus EB30 compact bench scale. The EB30 measured up a maximum mass of 30kg with 0.001kg of precision.

The energy conversion efficiency of the generator in its stock configuration was calculated by running the genset at a known resistive load for a pre-determined period of time and measuring the amount of fuel consumed over that time. The amount of power output by the genset in relation to the amount of fuel spent is defined as the energy conversion efficiency.

Power was drawn from the genset by a Model 627 Generator Test Set from Sotcher Measurement, Inc. The test set featured a maximum load of 10kW at either 120/240 VAC. The power output to the load bank was measured with an AEMC

8220 single-phase portable power analyzer. The load voltage was measured with standard voltage test leads and the current was measured with an AEMC MN93-BK AC current probe. The 8220 featured an optical-USB interface which could be used to view and record power data and characteristics on a computer in real-time using DataView data logger software.

Testing Procedure: Two separate propane tanks were used for the fuel consumption/efficiency testing. One tank was used to power the engine until it reached internal temperature equilibrium. For consumption testing at a specific load, the engine was operated at that load until it had reached equilibrium. After the engine reached equilibrium, the genset was powered off and the fuel source was quickly switched over from the warm-up tank to the second tank, whose initial mass was measured. The genset was powered up again and run for the desired amount of time (usually 1 hour). The genset was then immediately shut down and the fuel tank's final mass was measured using the bench scale. For the load testing, the amount of energy expelled through the load bank was compared to the amount of energy consumed as fuel to determine the fuel conversion efficiency. Fuel consumption rates of the genset in its stock configuration were compared to those with the FDP in place of the muffler.

Field Demonstration Prototype

FDP Components

The internal layout of the FDP very closely resembled the design of the SSP, only to a larger scale. Its general design resembled that of a hybrid cross/counter-flow heat exchanger. Like the SSP, the FDP was fully designed through several iterations in SolidWorks. Again, using the CAD models, plates, fins and insulation pieces were cut using CNC mills, punches and lasers.

Endplates: The FDP endplates were laser-cut to spec by JE Soares out of 6.35mm thick 304 SS. Minor ancillary machining on the plates was performed by Spark R&D. The plates were inspected and all burrs and sharp edges were removed prior to implementation. A small exhaust pipe extension was fabricated to allow for the FDP inlet plate to be connected to the existing exhaust manifold.

Fins: 800μm thick 1100-O Al was again used for the hot fins and 800μm thick C110 high purity copper was used for the cold. The CNC punch was used to cut the copper fins and some of the aluminum fins. The rest of the aluminum fins were cut with the CNC laser. The aluminum and copper fins were again electroplated with a ~7μm layer of nickel at their respective contact areas. They were then cleaned and prepared for implementation.

Spacers: Steel spacers made from 800μm thick 1018 cold-rolled steel were CNC punched to their desired shapes. The steel spacer design was eventually

altered further and new spacers made from 304 SS in the same thickness were designed and cut. Again, the aim of the steel spacers remained at providing internal structural support while reducing the thermal bypass near the TE dice.

TE Elements: The power-producing TE dice were used in the functional variants of the FDP. The dice were of the dimensions 2.04mm on each side and 1.52mm tall. This die height was specified in order to negate the necessity of using any Grafoil pieces inside the FDP. From results gained from SSP testing, no contact materials were used between the TE dice and their respective fins.

Insulation: As stated before, 1.59mm thick Thermo-Tork® TN-9045 gasket material was chosen for the insulation of the FDP. The insulation pieces for the FDP were cut to spec using CNC laser equipment by Miller Gasket Co. of San Fernando, CA. This laser-cutting process also produced a layer of carbon build-up at the cut edges which was carefully cleaned from the insulation pieces.

Since the size and volume of the gaskets needed for the FDP was on the order of 10 times of that of the SSP, outgassing was not a feasible option. Another outgassing constraint was that the time required to outgas FDP quantities was too great. Another problem was that an oven of sufficient size to outgas a reasonable number of insulation pieces was not readily available. It was determined that the insulation pieces would slowly cure while in use in the Honda genset.

Compression Rods: 35.6cm long, ¼-28 Inconel X750 through rods were designed and custom ordered. More anodized 3003 aluminum tubes were used to insulate the internal conductive components of the FDP from the through rods.

Bellevilles: Inconel X-750 Bellevilles were used on the FDP. Several different stacking techniques were investigated in order to find the best combination of spring force and expansion deflection.

Heat Dissipation Washers: Only SS finned heat dissipation washers were used in the FDP. They were placed only on the hot-side Bellevilles of the FDP since it was determined that the cold-side would stay well under 75°C.

Ducting: In order to effectively convey air from the radiator fan to the cold-side of the FDP, ducting was required. The CAD model of the entire Honda genset was used to design the ducting needed to bridge the gap between the radiator outlet and FDP cold-side inlet. When the final design was chosen, it was submitted to JE Soares and cut, bent and constructed by their equipment.

FDP Assembly

The FDP was assembled in much the same way that the SSP was. Layer by layer, the fins and insulation pieces were stacked until the assembly was complete. The stack was then compressed by torquing the through rods to the desired value while constantly monitoring the internal resistance of the stack. When the stack was compressed, the nuts of the rods were removed one-by-one and a stack of

Belleville springs were added and the rod was re-torqued to the previous value. When the entire FDP was assembled and ready, it was installed into the ES6500 via an extension between the stock exhaust manifold and the inlet of the FDP plate.

FDP Mock-up Testing

A mock-up of the FDP was constructed without any TE dice. The mockup was then installed onto the exhaust system and tests were performed. The first test of the mock-up FDP was of the exhaust backpressure exerted on the engine. The backpressure was measured with the same PX309-001G5V pressure transducer as was used with the stock muffler. The two pressures were then compared.

Another test performed with the mock-up was air flow rate testing through the cold-side of the FDP. The method used was the static pressure probe measurement. A differential pressure transducer was used to measure the pressure drop across the cold-side of the FDP in the way described above. One port of the differential pressure transducer was connected through the cold side fin bank into the air stream. The other port was left exposed to ambient air. The air flow rates at 10 different locations were measured. Figure 39 shows the 10 locations where air flow rates were measured.

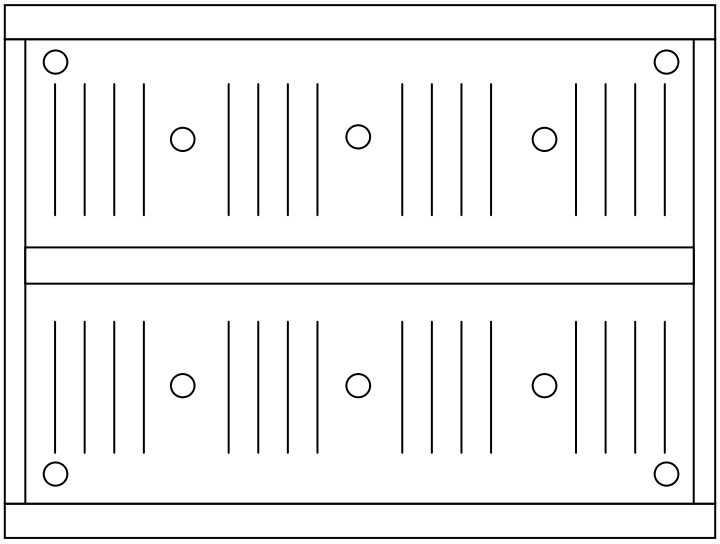

Figure 39: FDP Cold-Side Air Flow Rate Locations

Each location had its own vinyl tube that was pulled through the cold side fin bank from the outlet to the inlet. The ten locations measured all had individual tubes so that the test could be expedited. The tubes can be seen in Figure 40.

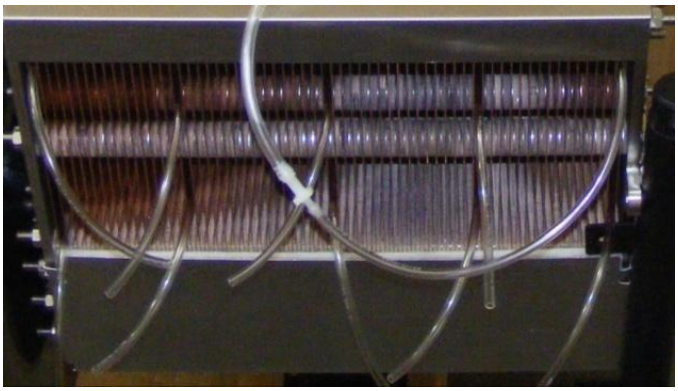

Figure 40: Cold-Side Pressure Tubes

The air flow rate testing was performed twice. The first test was performed with the engine running and powering the radiator fan in its stock configuration. The differential pressure transducer used for this test was a model PX139-015D4V

from Omega Engineering. The transducer required an excitation voltage of 5VDC which was provided by the Caswell SPC-9250 rectifier. The input voltage was monitored with a Radio Shack Model 22-812 handheld DMM and kept precisely at 5.00VDC. The PX139 transducer featured a ±103.4kPa pressure difference range and output a linear voltage range of 0.25VDC to 4.25VDC; where ΔP=-103.4kPa output 0.25VDC, ΔP=0kPa output 2.25VDC and ΔP=+103.4kPa output 4.25VDC. The output of the transducer was monitored with an Agilent U1252A handheld DMM.

The second test was performed by powering the fan externally with the Caswell SPC-9250 rectifier. For this test, the fan voltage was varied from 10VDC to 15.5VDC in increments of 0.5VDC. This was done so that the air flow rate could be measured over a range of fan outputs. The fan voltage was measured with a Radio Shack 22-812 handheld DMM and its current draw was measured with a Radio Shack 22-178 handheld DMM. This test featured a model PX164-010D5V differential pressure transducer for the pressure drop measurements. The PX164-010D5V featured a 0-2.49kPa pressure difference input range. The transducer output a linear 5VDC range from 1-6VDC; where ΔP=0kPa output 1VDC and ΔP=2.49kPa output 6VDC. The PX164 required 8VDC excitation which was provided by a Protek Model 3006 DC power supply. The Protek 3006 featured a voltage output range of 0-60VDC and a current output range of 0-1.5ADC. The excitation voltage was maintained at precisely 8.00VDC. The transducer's output voltage was measured with an Agilent U1252A handheld DMM. The air temperature was measured with an Omega OS425-LS infrared thermometer with a K-type

thermocouple probe inserted into the air stream. The second air flow rate testing setup can be seen in Figure 41.

Figure 41: Second Air Flow Rate Testing

The three DMMs and both DC sources can be seen in the top-right corner. The genset and FDP can be seen in the bottom-left and the PX164 differential pressure transducer can be seen on top of the FDP. The infrared thermometer and thermocouple can be seen in the top-left corner of the figure.

Both sets of pressure drop data were used to calculate the flow rate through the cold side using Bernoulli's Energy Principle of Fluid Dynamics. Both setups produced similar results.

FDP Testing

A fully functional variant of the FDP was constructed and installed into the genset. The generator was run at various engine speeds while exhaust inlet and

outlet temperatures, engine coolant temperatures and the open-circuit voltages were monitored and recorded. Later, the FDP was loaded resistively with a power resistor load bank to determine the power output characteristics of the FDP module.

FDP Performance Testing

FDP Mock-up

The FDP mock-up was fully assembled in the way intended by the design except that no TE dice were installed. The fins and insulation pieces were cleaned and inspected prior to installation. When all components were assembled, the top plate was put on and nuts were threaded onto the rods. The rods were torqued incrementally to ~0.565N-m (just tighter than finger-tight).

The mock-up was installed into the genset. The genset was run at idle and full speed/no load. The back-pressure was measured with the PX309-001G5V transducer. The transducer output was measured with the U1252A DMM at a sensitivity of 1VDC/1.379kPa.

For the first cold-side air flow rate testing, the engine was run at full speed with no load and the fan being powered in its stock configuration. The voltage output by the PX139 differential pressure transducer at each of the 10 locations was measured. The voltages were then converted into pressures.

For the second round of air flow rate tests, the fan was powered externally using the Caswell SPC-9250 DC source and the engine was not run. The fan output was varied by changing the input voltage to the fan. The fan voltage was varied

from 10.0-15.5VDC in increments of 0.5VDC. The fan voltage and current were recorded at each interval. The current and voltage were used to calculate internal resistance and power consumption of the fan. The PX164 differential pressure transducer was used to measure the pressure differential at each of the 10 locations for each of the fan input voltages. The array of flow rates and fan power data were used to aid in determining the flow regime of the cold-side of the FDP

FDP Build #1

FDP Build 1 was assembled using 504 TE dice clusters arranged in series. Its internal resistance was monitored while the stack was assembled and compressed. No contact media were used between the dice and fins. The fin tabs were cleaned with rubbing alcohol and allowed to dry before they were installed. The stack's rods were ultimately torqued to 2.825N-m. The FDP was then installed into the genset.

The genset was first operated at only the idle condition which gave an exhaust temperature of 285°C. Later it was operated at the full speed/no load condition with the exhaust temperature at 355°C. The open-circuit voltage of the FDP was monitored as were the exhaust inlet and outlet temperatures. Also measured was the coolant temperature at the entrance to the radiator. Fuel consumption rates were measured while FDP Build 1 was in place. The fuel consumption test was performed 4 times; two with the fan being powered in the genset's stock configuration and two with the fan being powered externally.

FDP Build #2

The internal steel spacer design was altered between FDP builds 1 and 2. New SS spacers were used in Build 2. FDP Build 2 was assembled the same way as Build 1 but two more layers of TE dice were added for a total of 512 dice clusters. All components were cleaned again and the stack was compressed as before. A different Belleville stacking technique was used for Build 2. Bellevilles were stacked in series on each of the rods.

Build 2 was subjected to the same idle and full speed/no load genset conditions for open circuit voltage testing. Build 2 was also subjected to resistive load testing with the genset running at full speed/no load to determine its power output. Two resistive loads were applied to the FDP: 0.5438Ω and 1.0294Ω.

CHAPTER 5

RESULTS AND DISCUSSION

TE Material Testing Results

Metal Foil TE Seebeck Testing

Initial iterations of the TE generator were designed to employ TE metals as the power-producing components of the heat exchanger. In order to gain an understanding of the TE effect, several rounds of testing were performed with regard to the Seebeck coefficient of different TE materials. The alloys Constantan and Chromel have the highest thermal emf output of all commercially available thermocouple metals. It was for this reason that these two alloys were initially chosen for evaluation. Several other metals and alloys were also tested as potential candidates for the TE generator. The materials tested included many different copper-nickel alloys, cobalt foil, many different nickel-chromium alloys, some iron-chromium alloys, several brazes, solders and graphite foils.

The following is a table of thermal emf values and corresponding Seebeck coefficients for TE materials tested over a range of temperature differentials. Also included is some tabulated reference data provided by thermocouple material manufacturers.

Table 5: Thermal EMF Values of Tested TE Materials

MATERIAL	**ΔT (K)**						Avg. Seebeck (μV/K)
P-Type Metals	100	200	300	400	500	600	
Kanthal-Cuprothal EN; vs. Pt-67, 0°C ref	3.505	7.451	11.71	16.18	20.79	25.48	39.31
Kanthal-Cuprothal CL; vs. Pt-67, 0°C ref	4.000	8.620	NA	NA	NA	28.66	43.62
Gen I (proprietary) P-Type	4.565	9.800	15.29	20.45	29.59	37.52	53.07
Gen II (proprietary) P-Type	4.150	8.510	13.40	18.55	23.84	28.80	45.13
Omega-Red Leg of Type E Thermocouple	4.173	9.012	14.33	19.92	25.76	31.77	48.14
Mathey-CuNi44Mn1-0.025mm	3.319	7.847	12.33	17.40	22.74	28.79	41.75
Schlenk-CuNi 44-as rolled-0.05mm	4.400	9.281	14.34	19.69	25.49	31.16	48.39
Goodfellow-Cobalt Foil-Annealed-0.05mm	3.440	7.576	12.08	16.63	20.55	24.26	39.28
Schlenk-CuNi 44-annealed-0.025mm	4.806	9.879	15.21	21.05	26.51	32.88	51.43
Schlenk-CuNi 18 Zn 20-as rolled-0.02mm	2.081	4.392	6.973	9.925	13.24	16.85	24.23
Schlenk-CuNi 18 Zn 20-tempered-0.02mm	1.903	4.095	6.556	9.242	12.32	15.77	22.57
N-Type Metals							
Kanthal-Thermothal P; vs. Pt-67, 0°C ref	-2.814	-5.970	-9.323	-12.76	-16.21	-19.62	-31.01
Kanthal-Nicrosil; vs. Pt-67, 0°C ref	-1.784	-3.943	-6.348	-8.919	-11.60	-14.37	-21.36
Gen I (proprietary) N-Type	-2.143	-4.370	-6.594	-8.756	-10.98	-13.11	-21.82
Gen II (proprietary) N-Type	-2.550	-5.030	-6.900	-9.200	-11.01	-13.10	-23.41
Omega-Purple Leg of Type E Thermocouple	-2.159	-4.514	-6.800	-9.069	-11.35	-13.43	-22.43
Ohmalloy-406-0.0559-080558A	-0.208	-0.499	-0.837	-1.211	-1.604	-1.989	-2.820
Ohmalloy-406-0.0533-0713039	-0.202	-0.455	-0.732	-1.032	-1.354	-1.690	-2.473
All values measured vs. unknown Ag wire (2.39% Pt) as reference leg, unless otherwise stated Measurements taken with a reference junction of 25°C unless otherwise stated Kanthal Data Tabulated (Kanthal)							

The Seebeck coefficients of high performance metal TE materials were tested because published values for thermal emf and Seebeck were not explicit in the

conditions that they were tested. Seebeck coefficient measurements are simple to perform. The components needed are a heat source, a heat sink and a system to measure voltage potential. The voltage potential between the hot and cold sides can then be measured and compared to the applied temperature gradient. As discussed previously, the Seebeck coefficient is simply the electrical potential produced per unit of temperature difference, i.e. volts/degree Kelvin. In order to produce a wide range of thermal gradients, it was necessary to build an insulated chamber with a heat source. This way, the material could have imposed upon it a high temperature on one side and the other can be subjected to either ambient temperatures or to a controlled temperature setting.

Traditional TE research typically uses a closed chamber for making Seebeck measurements. This allows for better control of the hot and cold temperatures. The major downfall of a high-precision Seebeck chamber is that they are very expensive. The Seebeck chambers used in this study were constructed of relatively low cost, off-the-shelf parts. The chambers used in this work were, however not conducive to testing bulk-die TE materials, such as the Bi_2Te_3 TE dice eventually used in the SSP and FDP. If Seebeck testing of these materials would have been desired, a new chamber would have been required.

Metal Foil TE Material EDS Elemental Analysis

Elemental analyses were performed on the metal TE materials in order to determine what comprised them. In addition to general knowledge of the materials in use, it was hoped that elemental analysis of the TE materials would shed some

light on how exactly the TE effect works. The samples were mounted in epoxy and inserted into the FE SEM chamber. The FE SEM chamber features a high-vacuum sample chamber. The high vacuum removes almost all air particles that can throw off the testing equipment. If any air is present in the chamber the electron beam can be disrupted and the test may be thrown off.

Table 6 and Table 7 feature the elemental analysis of the two proprietary TE metals procured for use in the TE heat exchanger. The metals have no specific name, so they are referred to as "N-Type Metal" and "P-Type Metal." Note that this "P" and "N" nomenclature does not refer to the solid-state conduction of the materials, only their TE polarity behavior as defined in the Background.

Table 6: N-Type Metal Elemental Composition

Element	Wt%	At%
Ni	90.17	88.74
Cr	8.81	9.79
Al	0.35	0.75
Ag	0.34	0.18
Si	0.21	0.42
Fe	0.25	0.26
Mn	0.13	0.14
Total	100.25	100.28

Table 7: P-Type Metal Elemental Composition

Element	Wt%	At%
Cu	56.27	54.14
Ni	41.65	43.37
Mn	1.20	1.33
Ag	0.26	0.15
Fe	0.29	0.32
Al	0.24	0.55
Si	0.04	0.09
Cr	0.04	0.05
Total	100.00	100.00

The tables feature the weight and atomic percentage of each element. The N-type metal closely resembles the composition of the thermocouple metal known as Chromel. The P-type metal closely resembles the composition of the thermocouple metal, Constantan.

Samples tested in the XRD are typically easier to prepare. Samples can be crushed and powdered or left in their solid state. They only must be cleaned in preparation for the XRD analysis. The machine was then operated through the desired incident angles and the diffracted beam data was collected. The XRD analysis performed on the TE metal foils did not show that any strange or unusual crystal phases were present in either metal foil.

Through Seebeck testing and solid-state physics research, it was determined that while TE metals work extremely well for temperature measurement, they do not work well in power production. The main reason for this is that metals have such a high thermal conductivity that a high thermal gradient is difficult to maintain. Attempts to decrease the thermal conductivity of a metal would decrease its electrical conductivity due to the Franz-Weidmann law discussed previously. Another major reason to use semiconductors was that their power output performance in terms of TE FOM is 10-100 times better. These factors supported the transition from metal TE materials to semiconductive TE materials.

The numerical modeling performed with this work was the defining factor in the transition from metal to semiconductive TE materials. It showed that thermal gradients would be difficult to maintain with the metal elements. Another major reason for the switch was that semiconductive TE dice were available from previous work. TE Bi_2Te_3 cooling dice had been procured for a previous task and were subsequently implemented into the Thermohex® design.

Cooling TE Bismuth Telluride SEM Analysis

When the transition to semiconductive TE materials was made, the Thermohex® design was modified slightly to accommodate the bulk dice. Several cooling TE dice previously used in the SSP were subjected to SEM and EDS analysis. These analyses were performed mainly as a way to investigate the contact surfaces of the dice. It was desired to know the condition of the silver contact material, i.e. to determine if it was porous, how well it was adhered, or if it was causing any unknown problems with the dice themselves.

The following figures show SEM micrographs and corresponding EDS line scans performed on the materials. The line scans were set to look for invasive elements entering the TE dice. The dice are typically coated with three functional layers on their contact surfaces. Molybdenum, nickel and solder flux layers were deposited in that order. The Mo layer was to prevent nickel diffusion into the dice, the nickel was to be a highly conductive oxidation prevention layer and the solder flux was to promote solder adhesion for use with soldered contacts.

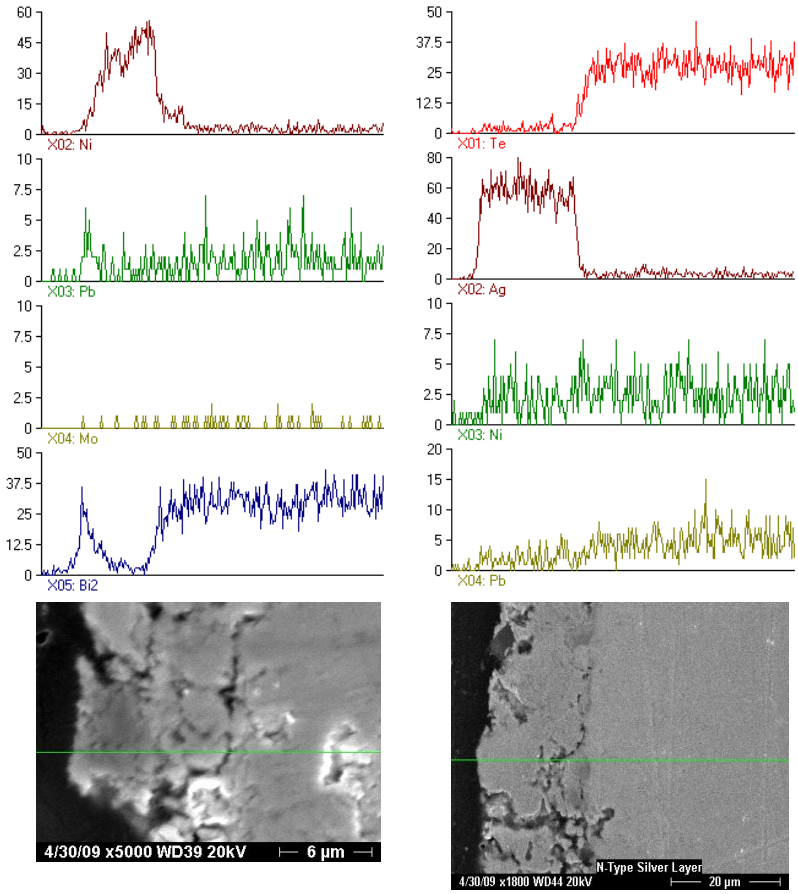

Figure 42: EDS Line Scans and Micrographs of TE Dice

The die on the left is a P-type and the die on the right is an N-type. An unused P-type die was examined for the Mo, Ni and solder layers thought to be present. The Ni layer was very apparent on the left edge, as was a small amount of Pb from the solder, but very little Mo was detected. The line scan on the right was of a used N-type TE die. The silver layer was examined in this scan and is easily seen as a relatively solid layer on the left side. Very little Ni and Pb were detected though. This may have been because the magnification was much lower than that of the right scan (1800x vs. 5000x).

A more in-depth investigation into the quality of the deposited silver was performed on the TE dice. The adhesion and porosity of the silver layer were the emphases of this analysis. The following figures show porous silver contact layers and poor adhesion to the surface of the TE dice.

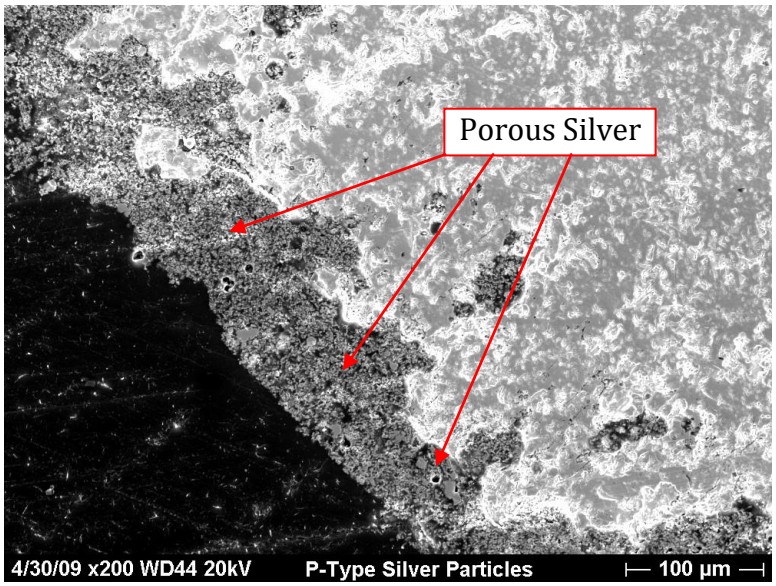

Figure 43: SEM Micrograph Detailing Porous Silver Contact Layer

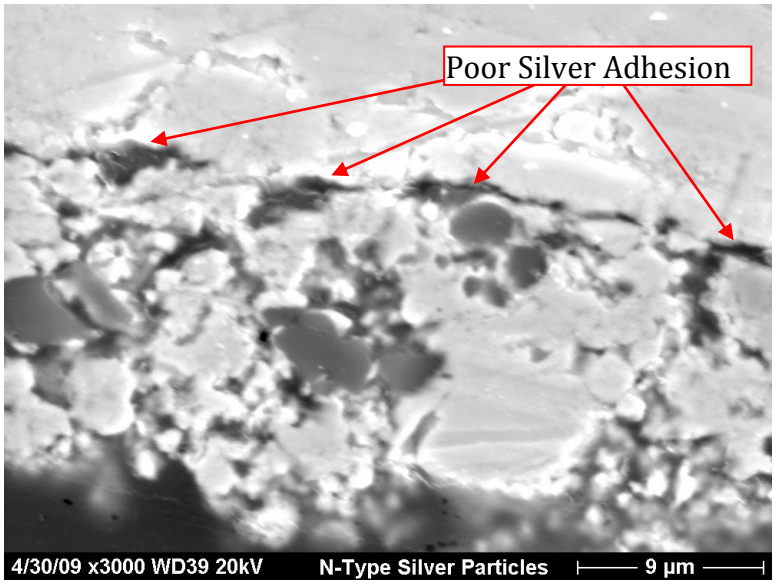

Figure 44: SEM Micrograph Detailing Poor Adhesion of Silver Contact Layer

As is easily seen from the micrographs, the condition of the silver was not conducive to electrical conduction. The high porosity and poor adhesion to the die's surface greatly inhibit the electrical contact between the dice and conduction fins. This high porosity and poor adhesion effectively decreases the cross-sectional area of the conduction surface, increasing its resistance.

Another check made was the condition of a fractured TE die. Figure 45 shows a cross-section of the fractured TE cooling die used in the SSP. The die was installed into the SSP and was subjected to high vertical pressure (~3MPa). As apparent in the micrograph existing slip planes of the crystal run parallel with the direction of compression, yielding planar slip.

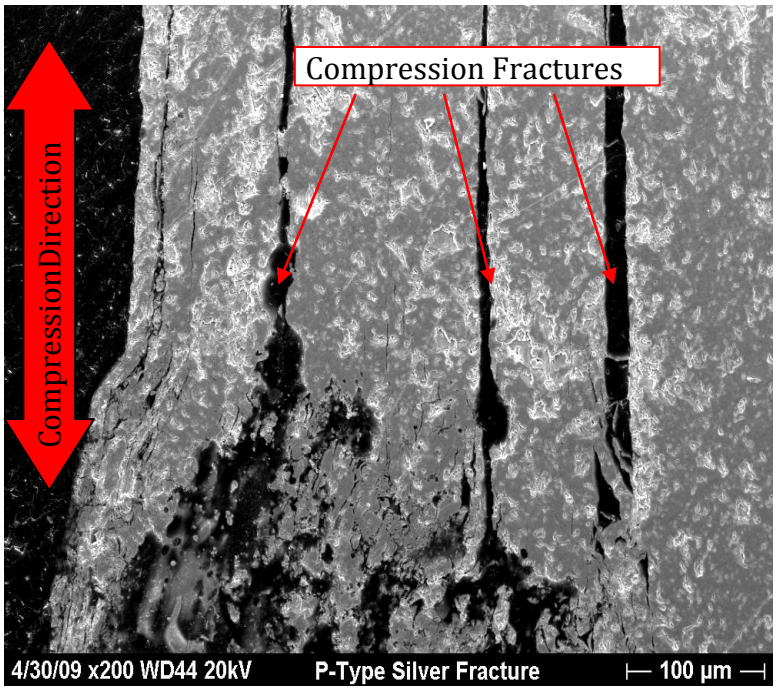

Figure 45: SEM Micrograph of Fractured Cooling Die

From the micrograph of the fractured die, it appears as though the conduction path through the die is maintained even though it is fractured longitudinally. Thus, it is felt that the fracturing seen by the dice in use is not catastrophic to the module. If a die does fracture, it is felt that the compression exerted between it, the fins and the surrounding insulation will help maintain contact.

Insulation Material Testing

The novel design of the Thermohex® TE heat exchanger has given way to the profound need for adequate thermal and electrical insulation. Since the fins of the heat exchanger not only conduct heat, but electricity as well, special care has been taken to ensure that each fin is isolated from its neighbors.

Figure 46 has been provided in order to better illustrate the concept applied to the Thermohex TE heat exchanger.

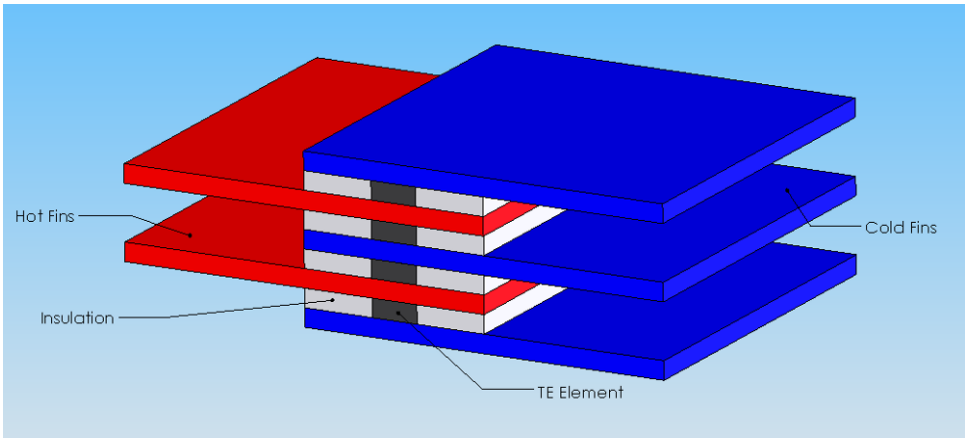

Figure 46: Simplified Design of the TE Heat Exchanger

As shown, the insulation must not only insulate the hot zone from the cold, it must also electrically insulate the fins from one another.

Insulation Materials

A variety of insulation materials were investigated as to their suitability with the TE heat exchanger design. Initial candidates were 3M Nextel 312 Ceramic Fiber Tape, a woven fiberglass cloth; and Zircar Refractory Composites Inc. RS-Tape, which is a fiber reinforced alumina composite. Woven ceramic fiber gasket material proved difficult to handle due to the brittle nature of ceramics. Also, the woven layout of the material made cutting a difficult issue due to frayed fiber ends that would unravel. Another issue encountered with the woven material was that its uneven surface tended to leave indentations in the soft metal fins. Ultimately it was determined that ceramic based insulation materials were too rough and not delicate enough for use in the thermoelectric heat exchanger.

It was decided that organic fiber-based insulation materials would be the best candidates for use in the thermoelectric heat exchanger. Organic gasket materials investigated were Interface Solutions' models TN-9000 and TN-9045 and Garlock 706 from Garlock Sealing Technologies. TN-9000 is an aramid fiber with a fully cured nitrile butadiene binder, TN-9045 is an acrylic fiber with an acrylic binder and Garlock 706 is an inorganic fiber matrix with a nitrile binder.

Organic-based fibrous insulation material was selected for its relatively low cost and ease of fabrication. A major advantage of using the type of insulation was that it can be cut very easily using a CNC laser. Laser-cutting allows for almost any

geometry to be selected for the gasket layout. Refractory ceramics and fiberglass must be cut using a specialized laser or by mechanical means (i.e. punching, shearing, etc.), which can be very expensive and time-consuming. Another major advantage of the fibrous insulation over the refractory is that it is very strong yet pliable and can be handled with little risk of damage. Refractory sheeting tends to be quite brittle and can be fractured easily.

A major disadvantage of using organic materials as the insulation for the thermoelectric heat exchanger is that the temperatures seen by the design can be above the maximum operating temperature of the material. Using an organic-based material at elevated temperatures can cause decomposition of the material. The decomposition then causes the material to become more brittle and less pliable.

Binder Curing

If an organic material is to be used at high temperatures for long periods of time, it is thought that the outgassing caused by the breakdown of the material could lead to electrical contact fouling. It was discovered that the insulation can be "baked" or "cured" in a ventilated laboratory oven near the desired operating temperature. The controlled curing of the insulation's binder before installation allows for the material to outgas without adversely affecting to the module. The outgassing doesn't noticeably affect the electrical and thermal insulating properties of the material. Care must be taken when handling the outgassed material because it becomes relatively fragile. The outgassing of the SSP insulation pieces was performed in a lab furnace.

Due to the much larger scale of the FDP, its insulation pieces were outgassed in another way. The insulation was installed into a non-functional mock-up of the FDP with no TE elements. It was then subjected to intended operating conditions and the insulation was allowed to cure. The mock-up was run at standard operating conditions for extended periods of time to ensure even and complete curing. After it was felt that the insulation was sufficiently cured, the TE elements were mounted in the insulation and the module was reconstructed.

High Temperature Analysis

DTA/TGA: The combination of the TGA and DTA can yield very useful data about how a material reacts to long-term high temperature exposure. A sample TGA/DTA was performed on calcium oxalate monohydrate, a material with a very pronounced and repeatable TGA/DTA reaction profile. A sample of calcium oxalate monohydrate was tested in the TGA/DTA as a basis for understanding the processes involved in subjecting materials to high temperature environments. Figure 47 shows the data from the calcium oxalate monohydrate ($CaC_20_4+1H_20$) reduction test.

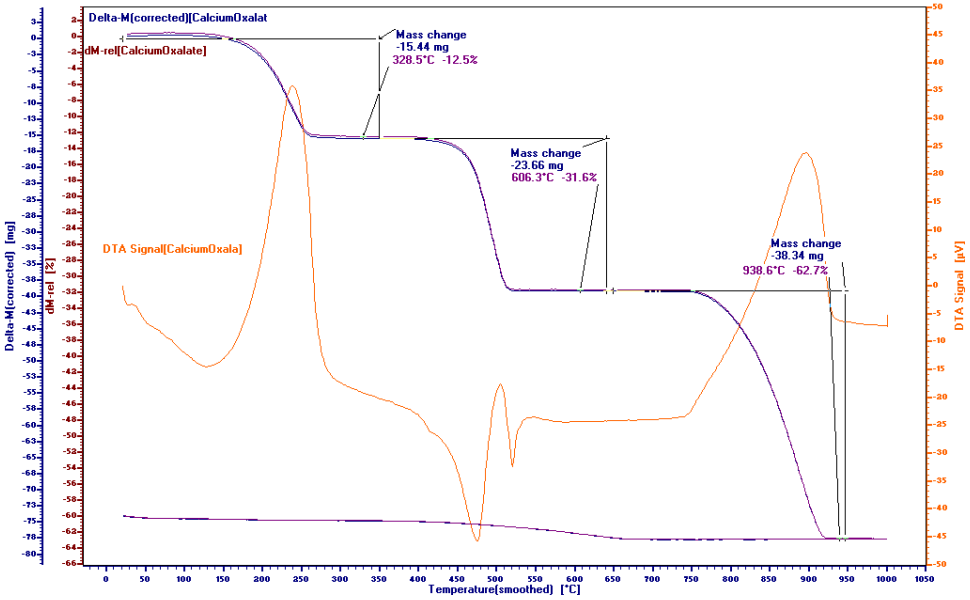

Figure 47: TGA and DTA Data for Calcium Oxalate Control Test.

The first reaction seen is dehydration, an endothermic reaction, where the water evaporates: $CaC_2O_4 + 1H_2O \Rightarrow CaC_2O_4 + H_2O\uparrow$ (-12.5% of total mass). The second is carbonation, exothermic, where carbon monoxide is released and calcium carbonate is formed: $CaC_20_4 \Rightarrow CaC0_3 + CO\uparrow$ (-31.6% of total mass). The third is called decarbonation, endothermic, where carbon dioxide is then released and calcium oxide is all that remains: $CaC0_3 \Rightarrow CaO + CO_2\uparrow$ (-62.7% of total mass). This test greatly aided in the understanding of the TGA/DTA equipment as well as the reactions that occur in other materials.

Insulation TGA Data: TGA tests of the candidate insulation materials were performed to determine the high temperature performance of the aforementioned materials. Figure 48 features a comparison between the respective amounts of mass lost of the materials during the same high temperature exposure. The three

materials tested were ThermoTork® TN-9045 and TN-9000 from Interface Solutions, Inc. and Garlock 706 from Garlock Sealing Technologies.

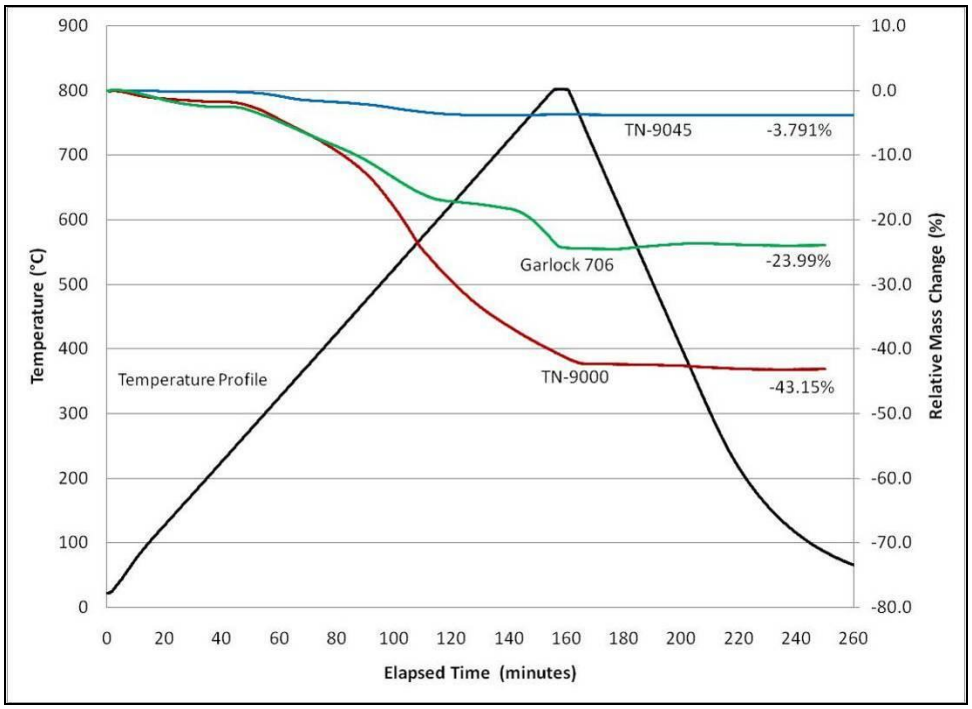

Figure 48: Comparison of Relative Mass Change of Insulation Materials

The TN-9045 lost 3.791% of its original mass, the TN-9000 lost 43.15% of its original mass and the Garlock 706 lost 23.99% of its original mass. Since the 9045 lost the least amount of mass during the test, it was felt that it had the best high-temperature performance and would best handle the rigorous temperatures seen in the SSP and FDP modules. The Garlock 706 and TN-9000 seemed to be satisfactory materials for the design, but their high mass loss indicated that their high temperature resilience was not adequate for use in the Thermohex® design. They were also less compliant and became more brittle after outgassing than the TN-9045.

Insulation DTA Data: DTA tests of the candidate gasket materials were performed concurrently with the TGA testing. The DTA signal is a measure of the magnitude of an occurring thermal process. A negative DTA signal is characteristic of heat absorption and a positive DTA signal is characteristic of heat evolution. Figure 49 features the comparison of DTA signals for all three candidate gasket materials.

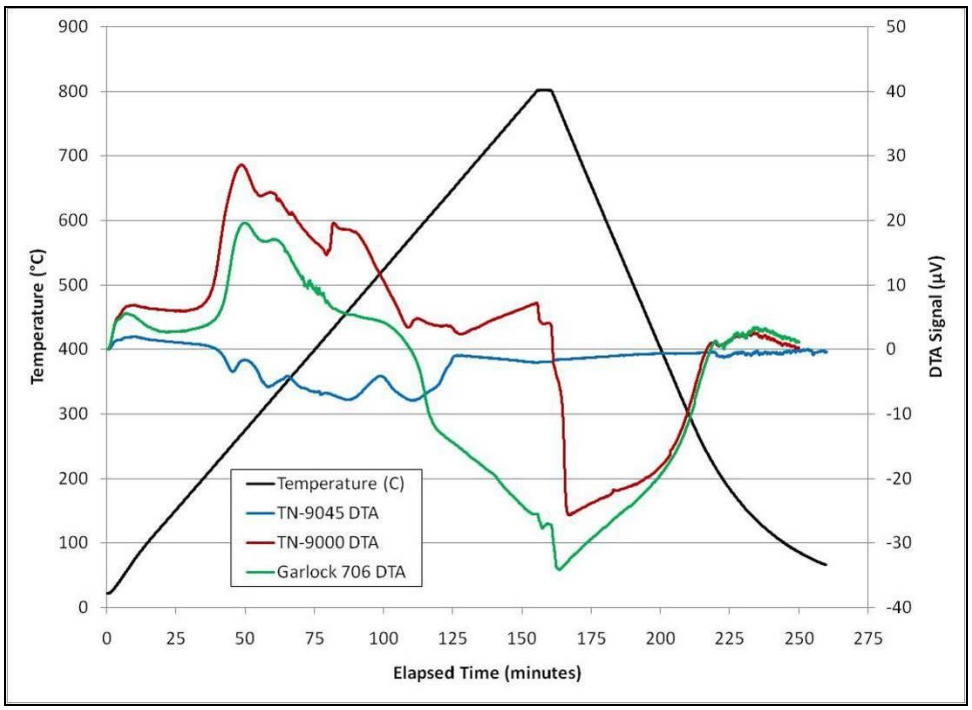

Figure 49: Comparison of Differential Thermal Analysis Values

As shown in Figure 49, the TN-9045 insulation had the lowest DTA signal peak at -7.90µV, the TN-9000 insulation had a maximum DTA signal peak at +28.6µV and the Garlock 706 insulation had the highest DTA signal peak at -34.2µV. This test also showed the high-temperature stability of the TN-9045. It had the lowest thermal reaction signal of the three materials tested. From the DTA data, it is

hypothesized that the material composition of the TN-9045 is very different from the Garlock 706 and TN-9000. Both the Garlock 706 and TN-9000 use a nitrile-based binder which is thought to be the reason that they act similar in the DTA test. It is thought that the nitrile binder must be less stable at high temperatures than the acrylic binder used in the TN-9045.

Dilatometry: Another test performed on the insulation material was a dilatometer test. A dilatometer measures minute changes in one axial direction as a function of increased temperature. It is comprised of a heated chamber inside of which is the sample fixture. The fixture consists of two parallel plates made of alumina, one of which is rigidly fixed and the other is connected to a LVDT. An LVDT (linear variable differential transformer) is a device that measures very small changes in linear displacement. An LVDT consists of three coils surrounding a paramagnetic core. The core is fixed to the free side of the sample fixture. The main coil in the center is charged with AC current and the outer two coils measure the current induced from the main coil through the core. As the core moves, the magnetic field of the sensing coils is altered and a voltage change is observed. The change in voltage can then be correlated to a change in displacement of the core due to the change in thickness of the sample. A schematic of an LVDT is featured in Figure 50.

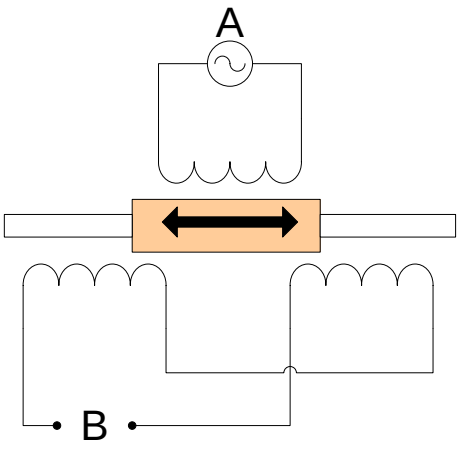

Figure 50: LVDT Schematic

Most materials tend to expand when heated. The expansion can be attributed to the decrease in density of the material due to the higher excitation of the individual atoms of the sample. Dilatometer data can be used to empirically calculate the CTE of a material. The dilatometry is a unique tool that can give great insight into a material's dimensional response to increased temperature.

TN-9045 Dilatometry Data: An outgassed piece of TN-9045 insulation material was subjected to a dilatometer test in order to determine its thermal expansion behavior. Before the test was performed, the insulation sample was outgassed in a lab oven at 375°C for 2 hours. Figure 51 features the dilatometry data taken for the TN-9045 insulation material.

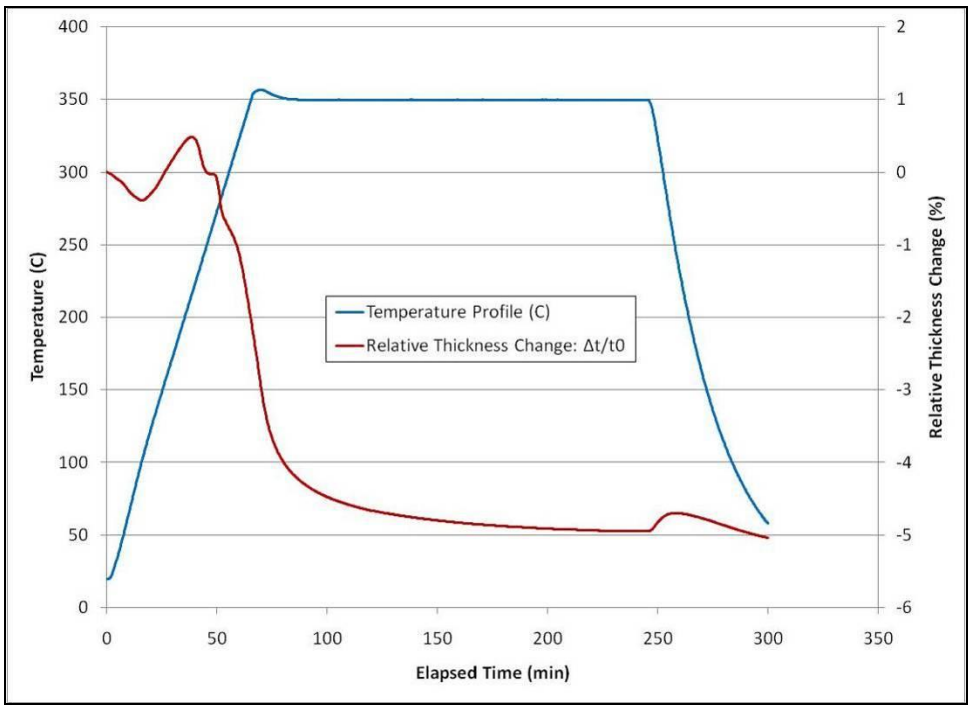

Figure 51: TN-9045 Dilatometry Data

As can be seen from Figure 51, the TN-9045 material lost approximately 5% of its original thickness over the length of the test. This loss of thickness indicated that thermal creep had occurred.

Through the combination of the TGA, DTA and dilatometry testing, it was determined that the TN-9045 gasket material was best suited for use in the Thermohex® design. The combination of low mass loss, low thermal reactivity and low dimensional change lead to the decision.

High Pressure Tests

Uniaxial Press

A damaged uniaxial press was reconditioned and used for pressure testing. The press frame was designed to handle a hydraulic jack with a 89kN force capacity. The original jack had an outlet port so the internal hydraulic pressure could be read and ultimately converted to the force being applied to the sample. The original analog pressure gauge had leaks that were addressed but could not be remedied. The leaking gauge assembly was inspected and attempted to be fixed but the threads of outlet port were not of a common type, and parts could not be found to match. Instead of trying to locate another pressure gauge assembly to replace the damaged one, the old jack assembly was completely removed and a new one was installed. The new jack also had a pressure outlet port. An electronic pressure transducer was selected over a traditional Bourdon gauge so that the pressure could be recorded with the DAQ. Heated platens were also used when making pressure vs. thickness measurements. The platens were capable of heating to ~200°C.

The reconditioning of the press produced a very useful piece of equipment. With the instrumentation available, the press has been and continues to be used in many different applications. The press was invaluable in the characterization and selection of insulation materials for the internal workings of the heat exchanger.

Long-term transient testing was attempted with the press, but it was discovered that the jack lost pressure over time as hydraulic fluid flowed around the pressure surfaces within. This made maintaining a constant pressure impossible.

One method used to remediate this issue was to constantly reapply pressure with the jack pump. This method was not the most accurate way to maintain the force of the press, but it sufficed for the testing performed.

Insulation Compressive Performance

In order to gain insight on how the insulation material performed mechanically after it was cured, several rounds of compressive testing were performed. The candidate materials were outgassed and subjected to uniaxial pressure with the use of the uniaxial press. The thicknesses of the materials with respect to static loads were recorded for various pressures and procedures. Non-cured samples were also subjected to the same testing as a baseline. Three main tests were performed on the TN-9045 gasket material.

In Test A, the samples thicknesses were roughly measured by using a digital caliper to measure the space between the top and bottom plates of the press. This proved to be very inaccurate and difficult to repeat. The data from Test A are provided in Figure 52.

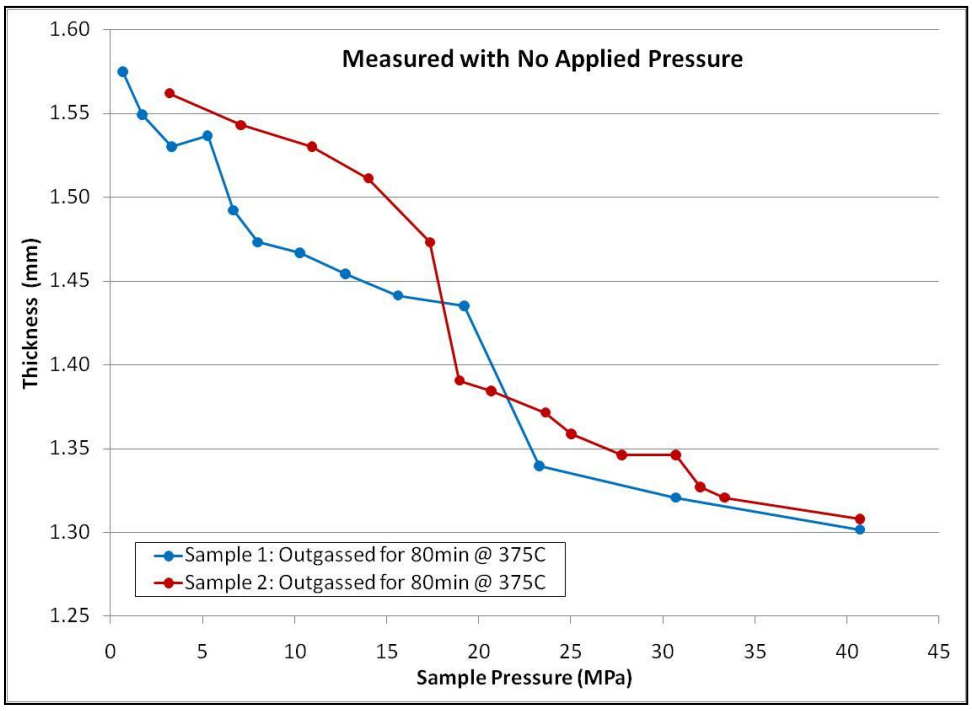

Figure 52: TN-9045 Pressure Test A

Test A yielded interesting results, but the employed method of measuring the thicknesses was thought to be of poor accuracy. In Test B, the load was applied to the material and then released and the thickness of the insulation was measured once removed from the press. Figure 53 shows the data from Test B.

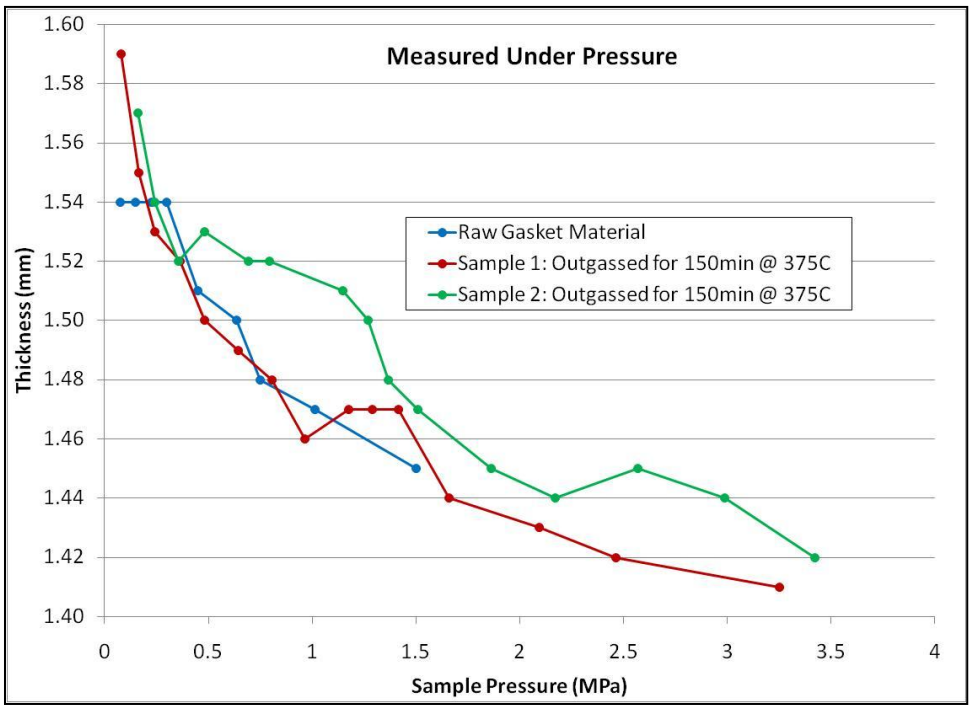

Figure 53: TN-9045 Pressure Test B

The method in Test B worked well and gave good accuracy. It was not, however, representative of the material's thickness under load. In Test C, a TE die was inserted into a hole cut in the insulation material. The sample was then loaded to the desired pressure. The load was released and the crushed die was removed and measured. The die height was directly representative of the thickness of the gasket at that pressure. The pressure applied to the insulation and dice cause the die to compress plastically, thus remaining at its shortest height. The data from Test C are shown in Figure 54.

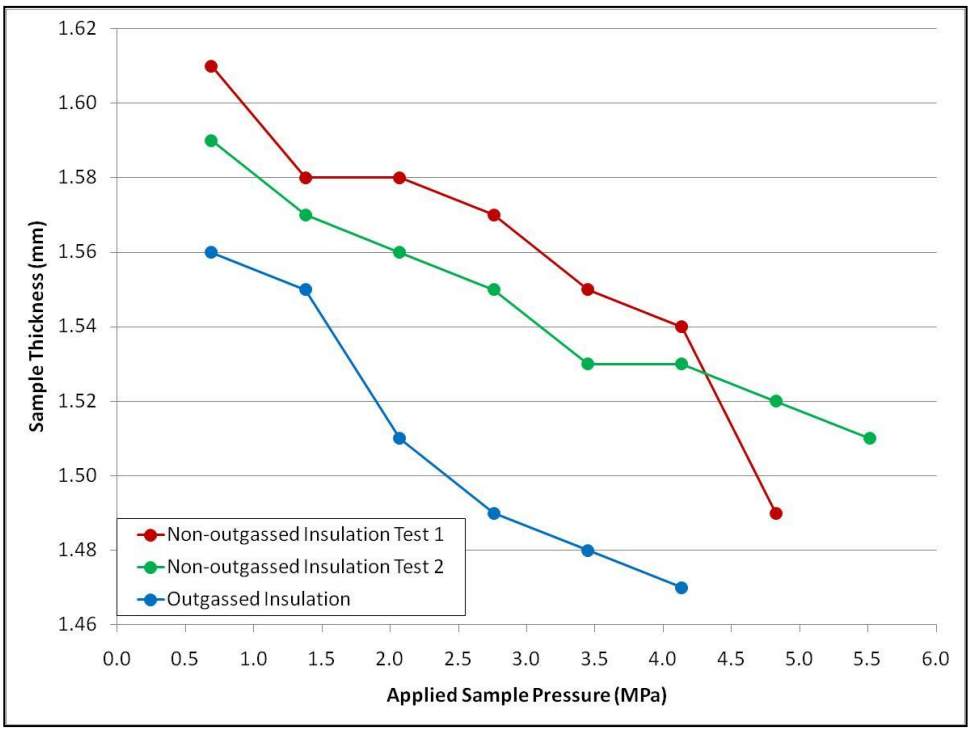

Figure 54: TN-9045 Pressure Test C

Test C yielded the most accurate and precise results for testing the gasket thickness vs. pressure. It is easily seen that the non-outgassed insulation holds its thickness better under pressure, which is logical due to the breakdown of the organics in the material.

As previously discussed, the crystal orientation of the TE dice is very orthotropic, meaning highly directionally dependent. In the case of the TE materials, the crystal planes run uniformly in the vertical direction. When the die is compressed, these crystal planes slip against one another and remain at their greatest deformed state. The strictly plastic deformation is due to the slipping of crystallographic planes of the dice as failure/fracture occurs. Figure 55 features a comparison between a compressed and a non-compressed cooling TE die.

Figure 55: Compressed and Non-Compressed TE Dice

Liquid Working Fluid Conductivity Testing

Limited research was performed into the feasibility of using liquid working fluids in the design of the TE heat exchanger. The use of liquid heat exchanger fluids could greatly increase the amount of heat absorbed and rejected per unit volume. Liquid water has a specific heat capacity of 4.18kJ/kg-K at 25°C and air has a specific heat capacity of 1.004kJ/kg-K at 25°C. The density of water at 25°C is 997kg/m^3 whereas air is 1.169kg/m^3 at the same temperature. This equates to the fact that 1L of water can hold 3500 times the amount of heat as 1L of atmospheric air at the same temperature.

Fin Surface Treatment Testing

The electrical conductivity of propylene glycol-based engine coolant between bare aluminum electrodes and anodized aluminum electrodes was compared. Engine coolant was selected due to the fact that it is already abundantly used in many thermal systems. A major issue with the design of the TE heat exchanger was that the fins are all electrically charged and have electrical potential between one another. If a conductive medium is present between the charged fins, current loss

may become significant and the overall performance of the TE generator would degrade. The electrical conductivity was tested to determine if it would cause electrical shorts between the conduction fins. The engine coolant was diluted with distilled water to a concentration of 50%.

Two tests were performed on the conductivity of engine coolant. The first used 1350-O Al electrodes with no surface treatment and the second featured the same grade 1350-O Al electrodes with an anodized surface finish. Figure 56 features the comparison of resistivity vs. liquid temperature for the tests performed with anodized and bare aluminum electrodes.

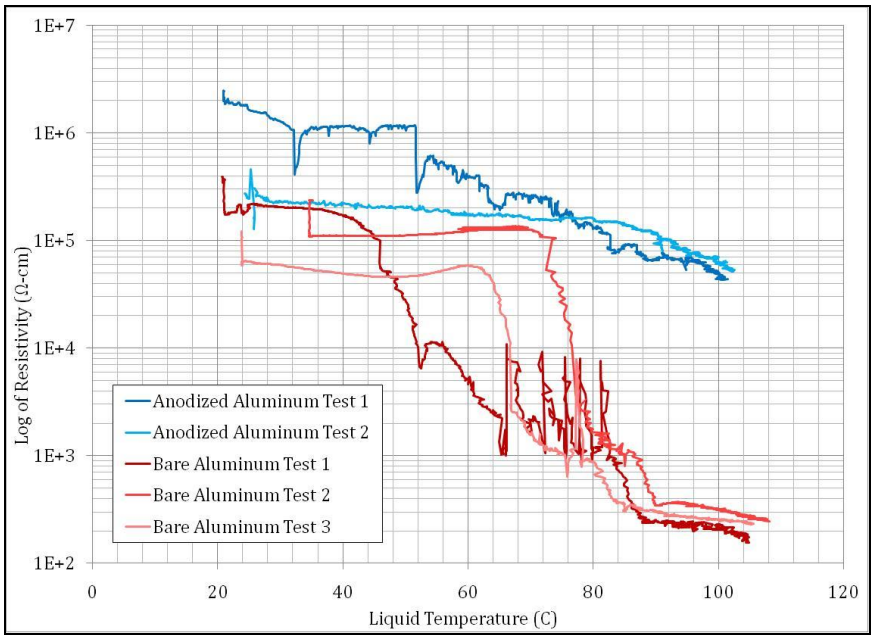

Figure 56: Semi-Log Plot of Engine Coolant Resistivity

The comparison shows that at around 100°C, the resistivity of the engine coolant between the bare aluminum electrodes was more than 100 times lower than that of their anodized counterparts. Another notable result was that the bare

aluminum test saw a drastic decrease in resistivity as a function of temperature. The reason for this has not been determined, but it is hypothesized that resistivity of the thin layer of natural oxide on the bare aluminum electrodes decreases with temperature.

The investigation of liquid operating fluids was eventually suspended due to sealing issues. If liquid operating fluids were to be used, a better method of sealing the gaskets was required. In addition, the selected gasket material used absorbs liquid quite readily. In order to properly seal the fins, while still maintaining overall electrical insulation, polymeric gaskets would be required. The use of polymers greatly lowers the maximum operating temperature the module can see. These issues led to the indefinite suspension of the liquid operating fluid investigation.

Electroplating

Aluminum Fins

Since aluminum naturally oxidizes in atmosphere at room temperature, it must be fully cleaned and stripped of this oxide. At the same time, further oxide growth must be prevented if proper plating adhesion is to occur. The use of sodium zincate takes on both of these jobs. Sodium zincate is an aqueous compound or zinc dissolved in sodium hydroxide. The alkalinity of the solution dissolves the aluminum oxide leaving a bare aluminum surface. The zinc ions in the solution are then attracted to the pure Al surface and become chemically bonded. As the surface of the aluminum becomes completely coated with metallic zinc, the oxidation of the

aluminum is prevented and can be exposed to air without issue. The freshly zincated aluminum can then be plated or the zincate can be etched with nitric or sulfuric acid and reapplied. Double zincating ensures that the aluminum surface is completely protected from oxidation by the zinc layer.

The subsequent plating steps then replace the zinc with the desired plating material (Ni, Cu, etc.). One issue involved with this process is that as the zinc is replaced by the desired material, its concentration in the plating bath builds up over time and fouls the bath chemistry. The zinc is removed periodically by running a "dummy" plate every so often using a corrugated SS cathode. The zinc in the bath plates to the low points on the corrugated surface and eventually is depleted from the bath.

Copper strike coats are typically used to build up the surface to be plated and to fill in any imperfections that may exist. It also serves as a good base for nickel adhesion since nickel and copper have a high affinity for one another.

Initial plating attempts all fell short of desired quality. The aluminum fins were first attempted to be plated with a copper strike coat followed by nickel coat. The plating tended to look satisfactory from the outside but further investigation yielded delamination of the nickel from the copper and the copper from the aluminum. Several initial different attempts were made with very few desirable results.

Figure 57 and Figure 58 feature two different views of an unsuccessfully plated aluminum part. Figure 57 is a 100x magnification of a cross-section of the

aluminum part. Delamination between the nickel, copper and aluminum is visible in the middle and right of the micrograph.

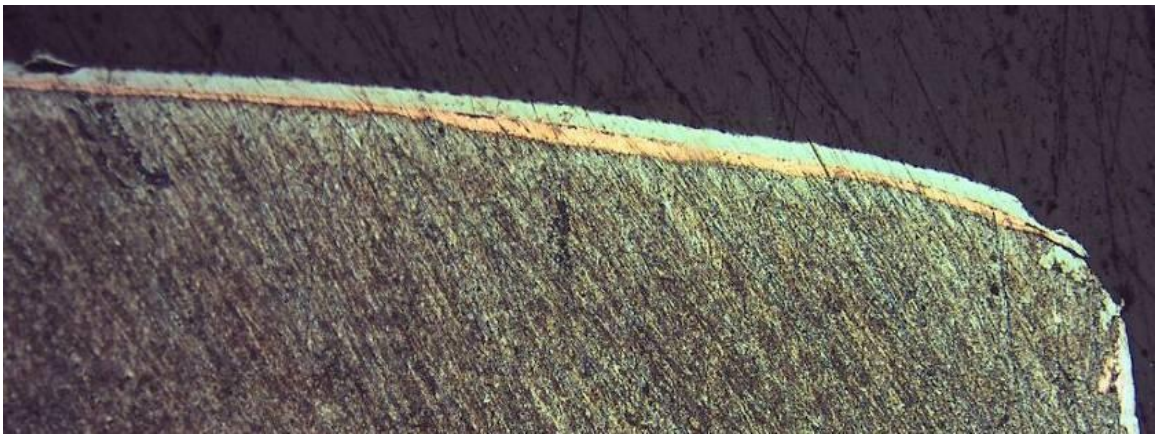

Figure 57: Optical Micrograph of Poorly Plated Aluminum Part (100x)

Figure 58 features a 100x magnification view of the surface of the same part as in Figure 57. The copper plating is visible through the holes in the nickel plate. Pitting and delamination are very apparent from this vantage.

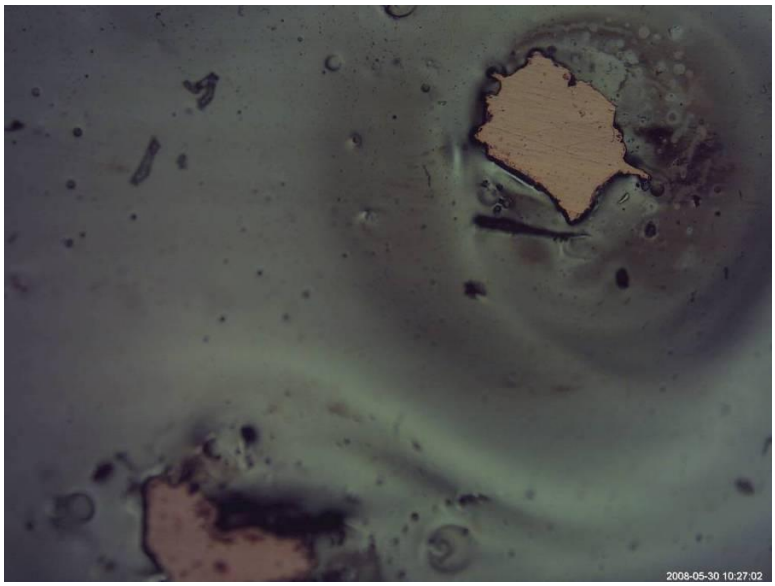

Figure 58: Optical Micrograph of Unsuccessfully Plated Aluminum Part (100x)

A major downside with using the copper strike coat is that it effectively doubles the time required to coat objects. It was also realized that copper strike coats are usually only used when the nickel plate is to be decorative. In the case of coating heat exchanger fins, the appearance of the fins is not important, only the quality and adhesion of the plate matter. It was for these reasons that the copper strike coat was eventually discontinued from the process of the TE heat exchanger construction.

Upon more investigation and research on electroplating, the procedure for successfully plating nickel onto aluminum was perfected. Previous plating attempts fell short for one major reason, neglecting the use of anode bandages. Initially no anode bandages were used due to the fact that their use had not been properly understood. It was later determined that anode bandages are an extremely important part of the electroplating process. The bandages collect sulfides and oxides that may evolve from the reduction of ions at the anode's surface. Once their importance was understood, the bandages were used and superior plating was achieved. Figure 59 features an SEM micrograph of a successfully plated aluminum part. The quality of the resulting plate was very high with good adhesion.

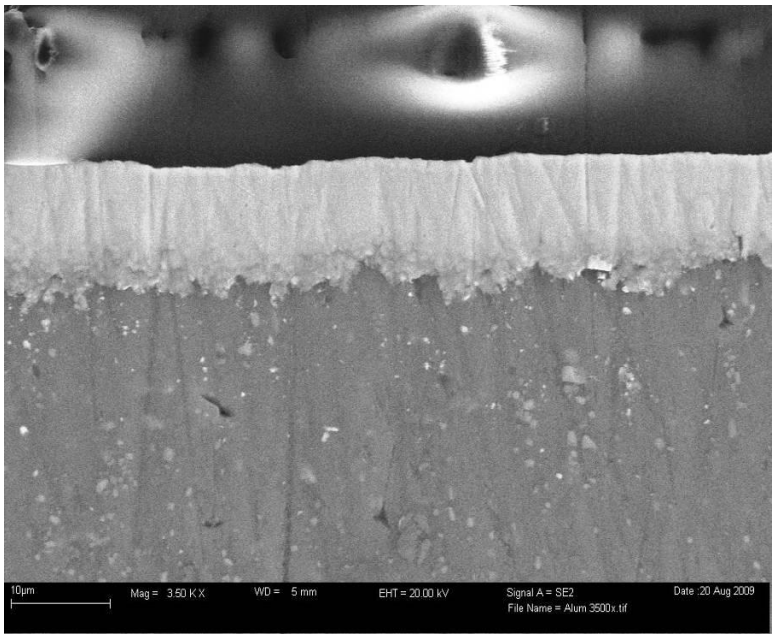

Figure 59: SEM Micrograph of Nickel Successfully Plated onto Aluminum

Copper Fins

Since copper also tends to oxidize easily, the copper surface must be cleaned and etched very well. Preparing copper for plating is much easier than for aluminum. Copper does not oxidize as quickly as aluminum and therefore only needs a quick surface etch to become ready for plating. Initially, ferric chloride was used to etch the surface of the copper parts. Ferric chloride etched the copper very aggressively and was difficult to control. Dilute nitric acid was found to be a much more effective copper etchant. A solution of 1 part 69-70% HNO_3 to 4 parts distilled water was used. It cleaned the surface very well without any aggressive reaction.

Initial plating of the copper fins dealt with the same types of delamination issues as with the aluminum. Upon optimization of the cleaning, etching and preparation methods, the nickel plating on the copper began to turn out well.

Both types of fins were plated with a current density of 97amps/m^2 for approximately 15min. This yielded a plating thickness of 7-10μm. It was later decided that 7-10μm was not sufficiently thick to protect the fins from mechanical wear. The plating duration will be increased to nearly 20 minutes in future plating endeavors.

Small-Scale Prototype

The small-scale prototype was an essential component of the research and development of the TE heat exchanger. It allowed for major design changes to be evaluated and tested without needing to fabricate large quantities of parts.

SSP CAD Models and Design Progression

As the conceptual design of the SSP progressed, its CAD models were continuously updated. Different stacking configurations and fin designs were investigated. The CAD model was imperative to the overall progression of the design. Not only did the CAD model allow for parts to be fabricated, it allowed for concepts and ideas to be attempted and examined without needing to have a great deal of parts made. Figure 60 shows an early CAD model of the SSP. This model featured TE metal foils as the power generating source. Figure 61 shows the stacking configuration for the SSP utilizing TE metal foils as the TE elements.

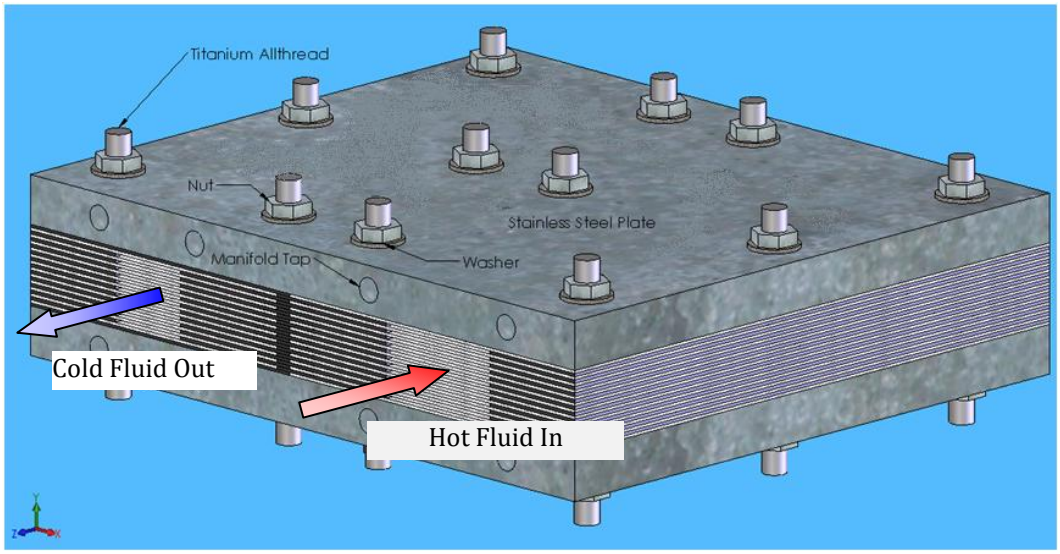

Figure 60: Early CAD Model of SSP

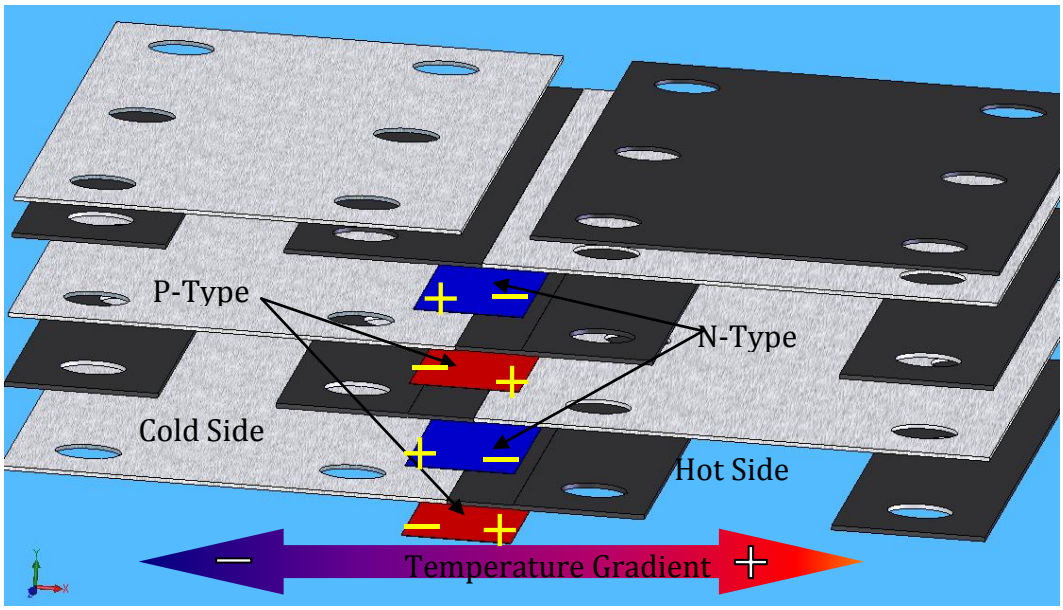

Figure 61: TE Metal Foil Stacking Design

The overall concept of the SSP did not vary much over time. The internal components, however, did. When the design of the SSP was altered to accommodate bulk TE dice as the TE elements, the internal components changed drastically. The

concept of the insulation material went from simply facilitating a thermal gradient, to actually housing the TE elements themselves. The figures below show the initial TE dice configuration of the SSP.

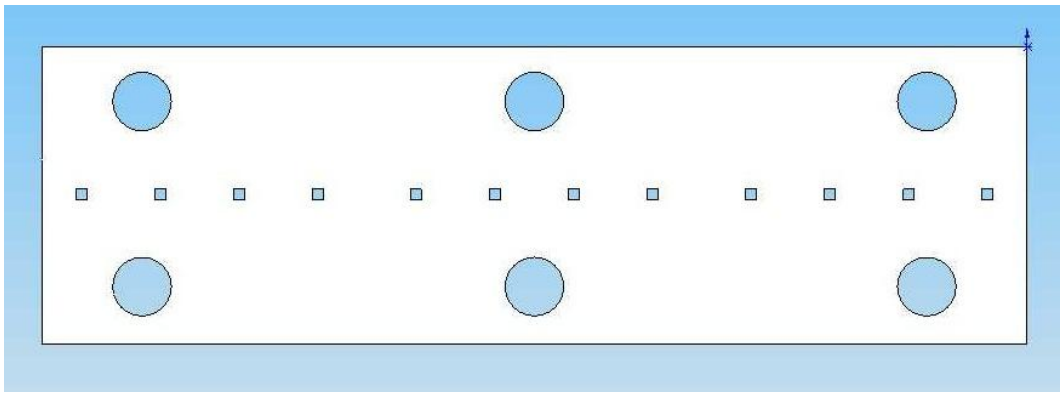

Figure 62: Initial Insulation Design for Housing TE Cooling Dice[2]

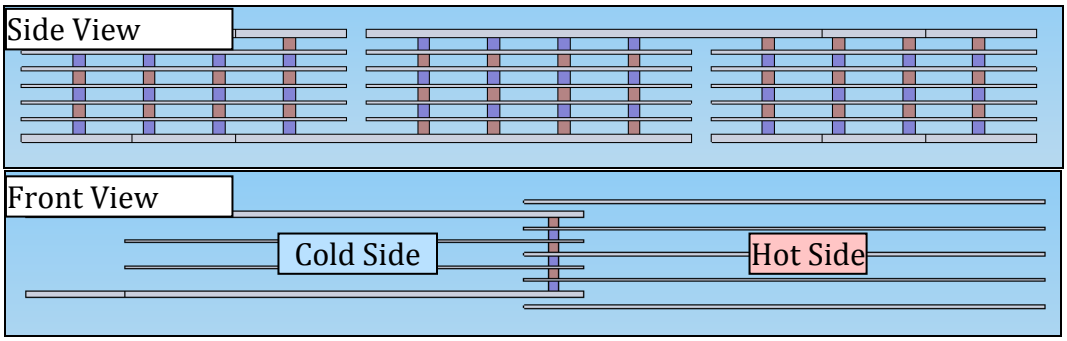

Figure 63: Side and Front View of Initial TE Dice Stacking Configuration (Only Fins and TE Dice Shown)[3]

The initial SSP layout featured 18 single cells of 4 dice. The side view picture shows the serpentine electrical path adopted early on and use throughout the life of

[2] CAD model by Nik Sorenson

[3] CAD model by Nik Sorenson

the SSP. The serpentine conduction path allowed for a much higher voltage to be achieved with the SSP. If this had not been adopted, the total power output would have remained the same but the voltage output would have been reduced by a factor of 3 and the current output would have been increased by a factor of 3. The front view shows the hot and cold-side fins from the direction of fluid flow (in and out of the page).

The dice configuration shown above was never fabricated but a similar one featuring two dice instead of four was assembled in Build 1. The next step in the design progression introduced the use of dice clusters instead of singe dice. There were several reasons for switching to clusters of dice; the first of which was that TE dice tend to be expensive and to custom order without knowing the optimal size for use within the SSP was not feasible. The cooling TE dice used were left over from previous TE work and were readily available. A major functional reason for the change was redundancy. If a single, large die was put in place of a cluster of dice, and that single die failed or fractured, the electric circuit may become compromised. If a cluster was in place and a single die were to fail, the rest of the dice would continue to function with only minimal loss of performance. Figure 64 shows the change in insulation design from single dice to dice clusters.

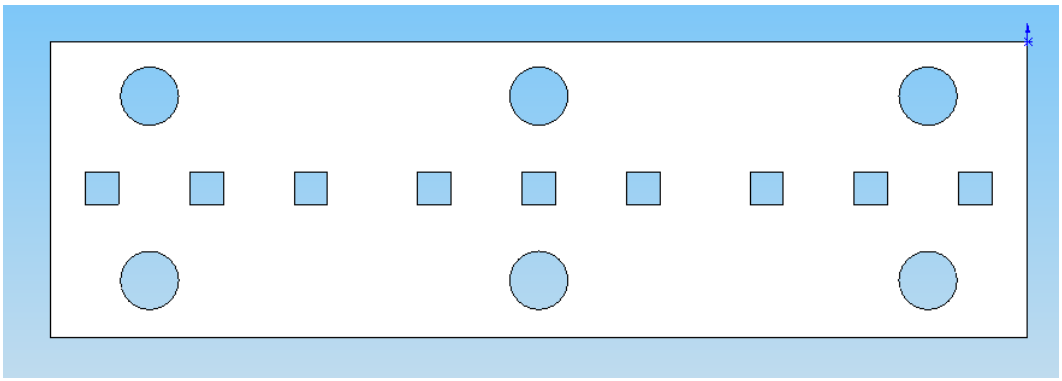

Figure 64: Initial 2x2 Dice Cluster Design[4]

This design was entertained only for a short while when it was determined that this number of dice clusters would not only be difficult to handle, it would allow more thermal bypass than was acceptable. High thermal bypass would lower the temperature differential of the individual cells, thus lowering the voltage building capabilities of the TE elements.

In order to combat thermal bypass, the number of clusters was lowered from 54 to 18. The number of dice in each cluster started at 4 (2x2) and then went to 9 (3x3). Increasing the number of dice per cluster effectively increases the amount of current the device is capable of outputting, while keeping relatively the same voltage potential. Another method employed in combating thermal bypass was the use of tabs. The tabs were designed to allow heat to reach the hot side of the TE dice while drawing heat away from the cold side of the TE dice, all the while preventing

[4] CAD model by Nik Sorenson

heat from travelling directly from the hot fin through the insulation and to the cold fin. Figure 65 shows the initial tab design developed for the SSP fins.

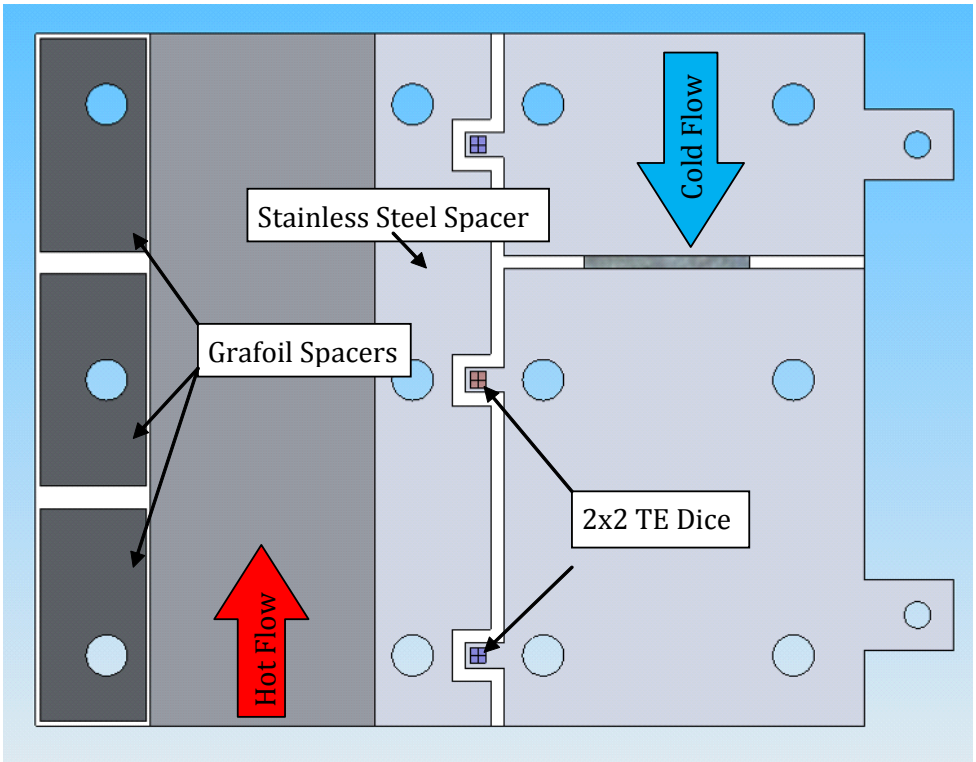

Figure 65: Initial Tab Design for SSP[5]

The fin tab design was taken one step further to end up at the final selected design. More material was added to the tab base in order to allow better heat transfer and more stability. The final fin tab design is shown in Figure 66.

[5] CAD model by Nik Sorenson

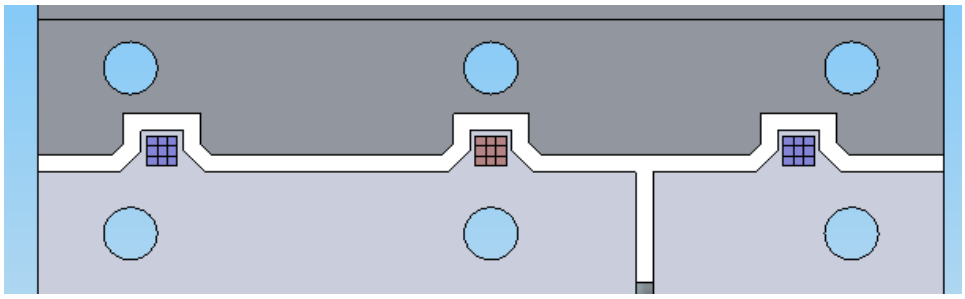

Figure 66: Final SSP Fin Tab Design[6]

The final fin design featured tabs that just covered the TE dice clusters. This allowed for solid electrical connection while allowing heat to flow to and from the dice clusters. By adding and optimizing the tab design to the fins in the SSP, its open-circuit voltage was dramatically increased from 88.0mVDC to 345mVDC.

When new power generation TE dice were ordered, their side length was chosen in order to be able to use the existing tabbed fins. The power generation TE dice were clustered in a 2x2 configuration due to problems encountered with the 3x3 configuration. The middle die in the 3x3 cluster would occasionally fall out due to inadequate pressure from the other dice in the cluster. In the 2x2 configuration, each die had pressure exerted on two sides by the insulation and by dice on the other two sides. The final TE element configuration proved to be very effective and easy to handle.

The tab design also prompted the introduction of internal steel spacers. In order to maintain even pressure on the TE dice, SS spacers were designed and

[6] CAD model by Nik Sorenson

implemented in the SSP. The spacers were the same thickness of the fins. SS was chosen for two main reasons. SS does not corrode easily, which is a problem with steel at high temperatures. The other main reason was that SS has a very low thermal conductivity (~16W/m-K @100°C).

SSP Components

Endplates and Manifolds: The SSP endplates and manifolds were constructed early in the project and used throughout. The endplates were the standard on which the fins and other internal components were based.

Fins: Several fin types and designs were investigated as possible candidates for use in the SSP. Initially, 0.4mm thick 1350-O aluminum was chosen for both the hot and cold-side fins when the metal foil TE materials were being investigated.

TE Elements: The SSP design initially featured TE metal foil material as the primary candidate. Several alloys were investigated, namely Ni-Cu and Ni-Cr alloys for their relatively superior Seebeck coefficients. In order to increase the overall power producing performance of the module, higher output TE semiconductors were introduced. Bi_2Te_3 TE cooling dice were available from previous work performed. The TE cooling dice measured 1.4mm on each side and 1.62mm tall. It was discovered that the cooling dice were coated with three different layers, a molybdenum layer, a nickel layer and a solder flux layer. The molybdenum layer was intended to prevent nickel diffusion into the TE material; the nickel was added

to act as a corrosion inhibitor; and the solder flux layer was intended to help with the adhesion of solder to the TE dice, as the cooling dice were designed to function in a soldered Peltier cooling module. The cooling dice were used extensively in the SSP to test for open-circuit voltages as well as power output performance. Builds 1-6 of the SSP featured the use of the cooling TE dice. Once it was felt that the bulk TE dice configuration would perform well, new TE dice for power generation were ordered. It was felt that the cooling dice were slightly too tall at 1.62mm. The power generation dice were ordered to a size of 2.04mm on each side and 1.52mm tall. The new TE power generation dice were used in Builds 7-9 of the SSP.

Contact Media: Four electrical contact media were investigated for this work. The contact media were not meant to fix the TE elements to the fins, but only to help maintain even and adequate electrical contact. CircuitWorks® silver conductive grease was investigated as a highly conductive contact material. The silver grease used consisted of very fine silver particles suspended in silicone oil. The silicone oil was initially thought to be an issue and rightly so. The oil tended to be drawn into the gasket material, effectively drying out the contact. The leftover silver then adhered well to the TE dice but did not perform as well as expected.

Next, Colloidal graphite from Ted Pella, Inc. was tested due to its use in SEM analysis. The graphite is painted onto a non-conductive object, such as the epoxy used to mount SEM specimens, in order to create a conductive path for the bombarding electrons to follow. The graphite was suspended in isopropanol which was allowed to evaporate leaving only pure graphite. It was felt that the graphite

would be very conductive and, therefore, would work well as an electrical contact. However, the contrary was discovered. The electron voltage used in SEM analysis is typically on the order of 10keV, whereas the individual dice clusters produced a voltage on the order of 20mV. The graphite was conductive but not nearly enough for the low-voltage, high current contacts within the SSP.

Two pure silver powders were also investigated. Powders consisting of 0.5-1μm silver microspheres and 4-7μm silver particles, both from Alfa Aesar, were chosen and tested. Both were dispersed in alcohol and painted onto the desired surfaces. As with the silver grease, the silver somewhat sintered itself to the surface of the dice. It was felt that the adhesion was due to the silver sintering to the solder flux layer on the TE dice. It was eventually discovered that the TE module output its greatest power when no conduction media were used.

Internal Steel Spacers: Internal spacers made of 304 SS were added to the SSP when the fin tab design was introduced. The spacers were made out of SS sheeting the same thickness as the fins and mirrored the tab layout. The spacers were intended to help evenly distribute the pressure within the stack, and performed this task very well. SS was chosen because of its low thermal conductivity and high temperature stability.

Insulation: 1.59mm thick Thermo-Tork® TN-9045 gasket material was chosen for the insulation of the SSP and, ultimately, the FDP. The insulation pieces were cut to spec by Die Cut Technologies in Northglenn, CO, using CNC laser

equipment. The laser-cutting process employed to cut the insulation materials produced a layer of carbon build-up at the cut edges. The carbon was carefully removed from the insulation pieces which were outgassed to the point that was necessary for the test runs.

Outgassing: It was discovered that the insulation pieces would outgas on their own when installed into the SSP while being subjected to the intended operating conditions. This prompted the pre-implementation outgassing procedure.

Grafoil: Since the available TE cooling dice were taller than the thickness of the TN-9045 insulation, it was felt that the thickness added by layers of Grafoil® would help protect them from being crushed. Grafoil® GTB flexible graphite sheet from GrafTech International was used to add thickness to the insulation. The thickness of Grafoil chosen for this application was 127μm. A piece of Grafoil was cut to the desired shape and placed on each side of the dice-cluster containing insulation. Special care was taken to not allow Grafoil to touch two separate conduction fins due to the fact that it is somewhat electrically conductive. The GTB grade was selected for its low cost and for the fact that it contains no binders or fillers and is said to be typically 98% carbon. The lack of binders aids in the high temperature stability of the Grafoil. The use of the Grafoil was eventually discontinued because it, in fact, added too much thickness and did not allow for adequate electrical contact to be made between the TE dice and the conduction fins. Removing the Grafoil from the SSP and, ultimately, the FDP designs greatly

simplified the fabrication and construction of both. The Grafoil pieces were very light, fragile and generally difficult to handle.

Compression Rods: The stack's compression rods were constructed of titanium for the reason that it has a very low CTE of 9-10ppm/°C. The rest of the stack has a composite CTE of much greater than 10ppm/°C and therefore would be passively compressed by the rods as the stack expands from heat. The rods used to compress the SSP were initially #10-32 UNF threaded titanium rods, cut to length. Standard jam nuts were used to compress the stack. The rods were torqued to nearly 5.65N-m. This tension value was determined to be too great for the #10 rods to handle due to observed bending. Custom cut and threaded titanium rods in the size ¼-28 UNF were obtained to replace the #10 rods. The rods were lubricated with Thread Magic Anti-seize, which is a paraffin wax-based lubricant. Bolt torque vs. internal compression calculations were made using the bolt torque vs. tension numerical model presented in Shigley (2004).

Rod Insulators: The #10 threaded rods were initially insulated from the conduction fins using alumina tubes. When the rods were changed to the larger size, alumina tubes could not be found with a thin enough walls to fit between the rod and the holes cut in the SSP plates and fins. Aluminum tubes were found that could fit between the rods and through holes. The aluminum tubes were anodized creating a non-conductive surface that successfully insulated the rods from the fins.

Belleville Springs: Belleville springs were introduced to the design as another way of keeping compression on the stack as it expanded and contracted. Belleville springs are conical shaped and designed for tension preservation. Bellevilles can be combined in either parallel (cupping each other"<<") or series (opposing each other"<>, ><") or any combination of the two. The parallel configuration increases the spring coefficient without changing the amount of possible deflection. The series configuration allows for a lower spring constant and a greater range of deflection. Any possible combination of the two can be used to tailor the Belleville stack to the desired load/deflection characteristics. Figure 67 is a cutaway view of some Belleville stacking configurations.

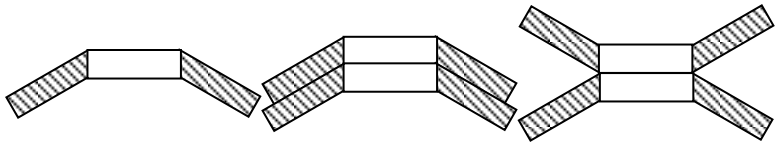

Figure 67: Belleville Spring Washer Stacking Configurations (cross-section)

Three Belleville materials were investigated: SS, carbon steel and Inconel X750. The SS was found to creep at high temperatures. The carbon steel and Inconel Bellevilles both have high temperature resistances (Sanders 2000) but Inconel X750 was ultimately chosen due to its superior high temperature creep and oxidation resistance.

Heat Dissipation Washers: Finned washers were designed and fabricated to aid in keeping the Belleville washers cool, therefore helping to inhibit thermal creep. Testing revealed that the Bellevilles in the SSP can reach as high as 220°C. No

definitive correlation between lower temperatures of the Bellevilles has been attributed to the use of the heat dissipation washers, but some tests have shown a decrease of 30°C with the use of SS washers.

SSP Testing

Non-Functional Build

The SSP was initially constructed in a non-functional form. This build was aimed at investigating the high temperature performance of the individual SSP components. The SSP mock-up was assembled without any TE elements and it was subjected to inlet air temperatures of 430°C. The components behaved satisfactorily except that the insulation materials began to outgas, which prompted the pre-construction binder outgassing procedures.

Functional Builds

Functional builds of the SSP constituted a large portion of the work performed for this project. As the design progressed, changes were made to the design and components. Build 1 featured relatively thin 1350-O aluminum fins (~250μm thick). The 250μm fin material was chosen as a starting point because it was felt that it would allow for the cell density to be increased. 1350-O aluminum was chosen as the fin material due to its high purity. Pure materials typically have better thermal and electrical conductivities and also feature higher melting temperatures than alloys. It was eventually determined that from a physical and

thermal standpoint, this fin thickness was too thin. Fins of this thickness were difficult to process and cut and were very easily bent and distorted. They were also restrictive in terms of conductive heat transfer. Thicker fin materials were subsequently chosen. 1100-O aluminum in 800μm thickness was selected as a sufficient compromise between overall compactness and high conductive heat transfer to and from the TE dice.

The high thermal and electrical conductivities of pure copper lead to the decision to include copper as the cold-side fin material. Copper fins on the cold side would offer great improvement in the way that the thermal gradient at the TE dice would be higher and the dice would stay cooler as more heat would be drawn away.

Much investigation was performed as to the ideal torque that would be applied to the through rods. As mentioned previously, the torque vs. tension approximation set forth by Shigley was used to approximate the internal pressure of the SSP with reference to the bolt torque. Through empirical testing and mathematical modeling, it was determined that a torque of 1.695N-m would offer sufficient internal pressure as well as maintain bolt tension between thermal cycles. Torque values of up to 2.825N-m were used on the SSP rods with no detrimental effect to performance. The rod torque, in addition to the use of Belleville springs, yielded a successful and reliable technique for maintaining internal contact pressure. Functional variants of the SSP were constructed 9 different times. The following are results gathered from each of the builds.

SSP Build #1

3/27/09–4/6/09 (2hrs run time): The stack's IR at 1.695N-m of torque was 0.32Ω. Its IR at 3.39N-m was 0.20Ω. An open-circuit voltage of 75mVDC was achieved and maintained for 45minutes at an air inlet temperature of 350°C. The maximum open circuit voltage achieved with this build was 88mVDC with a 483°C inlet temperature.

Upon dismantling Build 1, it was discovered that the silver contact material had hardened to the surface of the TE dice. It looked as though the silver had sintered to the dice.

SSP Build #2

5/29/09–6/7/09 (1hr run time): Build 2 contained 18 total dice; 9 sets of 2 dice in series). The IR was measured to be 0.6Ω at 1.695N-m. The maximum open-circuit voltage was measured to be 345.5mV at an inlet temperature of 373°C. The measured open-circuit voltage was greater than the numerical model's predictions. After the SSP had cooled, the IR had dropped to 0.35Ω.

SSP Build #3

6/8/09–6/10/09 (3hrs run time): The rods were re-torqued to 1.695N-m which gave an IR of 0.5Ω. The module was run in the test rig and achieved an OCV of 347mV with an inlet temperature of 386°C. Resistive loading was performed yielding a power output of 110mW at 184mV and 0.592A. The next day, the SSP was run again and a power output of 125mW (187mV and 0.670A) was reached.

SSP Build #4

6/15/09–6/30/09 (14.5hrs run time): The SSP was torqued to 1.695N-m and IR = 0.054Ω. Comparing the voltage of a dice cluster to its corresponding temperature difference gave a Seebeck coefficient of approximately 170μV/K which is near what manufacturers predict. Build #4 was run 5 separate times and produced a maximum OCV of 375mV at 483°C and a maximum power output of 405mW (178mV, 2.27A).

SSP Build #5

7/17/09–7/29/09 (10hrs run time): The stack was torqued to 1.695N-m and 0.045Ω. The stack was run in the test rig which output a maximum OCV of 380mV at 483°C and a maximum power of 540mW (217mV, 2.48A). The power output dropped to less than 200mW toward the end of testing.

SSP Build #6

8/3/09–8/31/09 (2hr 20min run time): The IR was approximately 100mΩ at 2.26N-m of torque. The maximum open-circuit voltage reached was 384mV at 560°C. The power output peaked at nearly 250mW but degraded to around 200mW.

SSP Build #7

8/31/09–9/18/09 (5hr 45min run time): The IR was ~50mΩ. The maximum open-circuit voltage was 350mV at 495°C. The maximum power output

was 700mW (210mV, 3.3A) and was maintained for 3 hours. The power output degraded to 550mW (180mV, 3.0A) in subsequent tests.

SSP Build #8

9/18/09–10/20/09 (9hr 40min run time): The IR was measured to be 26.35mΩ using LOM-510A micro-ohmmeter. The SSP produced a maximum open circuit voltage of 342mV at 493°C. It initially output around 750mW (191mV, 3.92A) and degraded to 580mW (170mV, 3.42A) by the end the first test. The IR had increased to around 60mΩ after test. The SSP was re-torqued to 1.695N-m which brought the IR down to 41mΩ.

The stack was heated in an oven to 300°C for 8 hours. The IR at the start was 51mΩ and had fallen to 19.5mΩ after it had cooled. The SSP was run again, producing over 900mW for two hours. The SSP was run a third time, producing over 850mW for an hour. After the testing was complete and the stack had cooled, the IR was measured at 22.61mΩ. The stack was re-torqued to 1.695N-m lowering the IR to 21.62mΩ. The SSP was disassembled revealing that the TE dice were very strongly bonded to the fins.

SSP Build #9

10/20/09–11/3/09 (36hr run time): SSP Build 9 was the last build tested for this work. It was the culmination of the information and experience gathered from the previous 8 builds. It used no contact media. It featured the highest output seen to date. (1.47W).

Test 1: The stack was torqued down to 1.695N-m and the IR was measured to be 12.6mΩ. The SSP was run in the test rig and produced 385mV of open-circuit voltage at 485°C. Test 1 had one thermal cycle over 2hr 20min. Under load, the SSP produced a maximum of 1.47W (195mV, 7.54A). The power output remained over 1.40mW for 1.5hr.

Test 2: The IR was 12.92mΩ. Re-torqued to 1.695N-m resulting in IR = 12.24mΩ. The maximum open circuit voltage was 385mV at 487°C. The power peaked at 1.52W (198mV, 7.69A). The power held over 1.3W for the single 4hr50min cycle.

Test 3: The IR was 13.22mΩ. Re-torqued to 1.695N-m resulting in IR = 12.94mΩ. The maximum open circuit voltage was 403mV at 530°C. The power peaked at 1.35W (192mV, 7.03A) and held over 1.25W for two thermal cycles totaling 6hr.

Test 4: The IR was 14.52mΩ. The stack was not re-torqued. The maximum open circuit voltage was 392mV at 492°C. The power peaked at 1.35W (199mV, 6.76A) and held over 1.20W for 3hr.

Test 5: The IR was 14.57mΩ. The stack was not re-torqued. The maximum open circuit voltage was 420mV at 540°C. The power peaked at 1.40W (192mV, 7.32A) and held over 1.20W over three thermal cycles totaling 2hr.

Test 6: The IR was 18.99mΩ. The stack was not re-torqued. The maximum open circuit voltage was 388mV at 520°C. The power peaked at 1.35W (189mV, 7.15A) and held over 1.10W over four thermal cycles totaling 4hr.

Test 7: The IR was 25.52mΩ. The stack was not re-torqued. The maximum open circuit voltage was 365mV at 480°C. The power peaked at 1.15W (186mV, 6.18A) and held over 1.10W over two thermal cycles totaling 2.5hr.

Test 8: The IR was 27.37mΩ. The stack was not re-torqued. The maximum open circuit voltage was 355mV at 480°C. The power peaked at 1.05W (175mV, 5.99A) and held over 0.90W over three thermal cycles totaling 2.5hr. The IR was measured to be 32.24 after the SSP had cooled.

The SSP was allowed to sit for 2 days past the last test. Its IR at that time was 38.38mΩ. It was torqued to 1.695N-m giving IR=32.59mΩ. The torque was increased to 2.26N-m giving IR=25.93mΩ. It was then torqued to 2.825N-m giving IR=22.12mΩ. It was disassembled. It is hypothesized that the increase in IR resistance was resultant from several factors. One factor may have been that the dice themselves were undergoing phase changes or diffusion on a molecular scale due to elevated temperature. Another reason may have been that the plated contacts had been damaged and the underlying copper and aluminum was oxidizing, increasing contact resistance.

During Test 8, two of the aluminum fins in the hot fluid stream had warped to the point that they were in contact with one another. This resulted in an electrical

short across a TE couple. The extreme warpage was resultant from the hot fluid stream reaching temperatures in excess of 550°C on three separate occasions.

Honda ES6500 Genset Test Bed

The main purpose of the project was to design, fabricate and test a TE heat exchanger that can be used in practical applications. In order to fully accomplish this goal, a practical test bed was needed. The test bed needed a certain set of attributes to be compatible with the TE heat exchanger design. One of the main attributes was that the test bed needed to produce unwanted heat that could be captured and used in a TE module. Another important feature was that the test bed needed to be small and mobile for ease of testing and analysis. Finally, the test bed needed to be a machine or device with real-world application potential, not an exotic machine with limited practical use. It was finally decided that an internal combustion engine would be the best candidate for the TE heat exchanger application.

Since internal combustion engines are one of the most common machines in use today, more refinement had to be made to the selection of the TE heat exchanger test bed. Another criterion was added to the selection parameters: a liquid-cooled engine. The heat rejected from the radiator of a liquid-cooled engine could most certainly be used in the TE heat exchanger. Another feature of a liquid-cooled engine was that the system's radiator could potentially be modified and retrofitted to act as the TE heat exchanger.

The addition of the liquid-cooled engine parameter greatly narrowed the search. A major problem encountered was that few small engines feature liquid cooling systems due to the fact that most small, light duty engines can be cooled easily by air with finned cylinder heads and engine blocks. Liquid cooling systems are hard to find in engines smaller than 15kW.

Small motorcycle and ATV engines were investigated as possible candidates, but tended to be undesirable due to the fact that they weren't self-contained and easily maneuvered. Finally it was decided to find a generator featuring a liquid-cooled engine. This proved to be somewhat difficult because most new generators smaller than 7kVA in the U.S. tend to be air-cooled. Part of the reason for this is that regulations on small engine emissions have forced engine designers to reduce the compression ratio of the engines. Lower compression ratios yield cooler running, albeit lower efficiency engines. The cooler running engines can, in turn, be cooled using simpler means.

A liquid-cooled Honda ES6500 genset was ultimately selected as the test bed for the TE heat exchanger. The ES6500 was a 6.5kW peak, 6kW continuous output generator powered by a liquid-cooled 9.7kW motor. This model was selected for a number of reasons: it featured a liquid cooling system with an electric fan; it was small, self contained and mobile; and it provided a useful amount of power, i.e. a typical household can be easily powered by 6kVA.

An ES6500 with an aftermarket gaseous fuel conversion was located. The conversion kit featured connection fittings, a regulator and fuel cutoff solenoid so

that the engine could be run on propane/LPG/natural gas or gasoline if desired. This was very beneficial due to the fact that propane burns much cleaner than gasoline and can be used indoors for short periods of time. Another desirable aspect of using propane fuel was that it can be handled very easily and safely in the form of 9kg tanks.

Another major benefit of using small 9kg propane tanks was that fuel flow rates could be easily and accurately measured. The mass change of a propane tank was easily measured. The change in mass over a known period of time could then be correlated to energy flow rate into the engine by using the calorific value of the fuel. The following formula better illustrates the conversion of mass change to energy transfer:

$$P_{in} = h_{fuel} \cdot \Delta M_{fuel} / t \tag{11}$$

Where P_{in} is the rate of energy (power) in Watts (Joules/second) input to the engine in the form of fuel, ΔM_{fuel} is the mass change of the fuel tank in kg, h_{fuel} is the calorific value of the fuel being used in Joules/kg (energy/mass) and t is the time over which the test was run. The amount of power output by the genset in relation to the amount of fuel consumed is known as the energy conversion efficiency, i.e. how well the genset converts fuel energy to output energy.

A major benefit of using a generator as opposed to an engine with only a shaft output was that power output could be very easily measured using an AC power analyzer. A known resistive load was applied to the generator and the power output to the load was measured using the power analyzer. By contrasting the

power input in the form of chemical energy with the power output in the form of electricity, the energy conversion efficiency of the genset could be calculated.

The genset's radiator was cooled by a 50-60watt electric fan that was powered by an unregulated secondary coil within the main winding of the generator. The unregulated power source output between 50 and 60W of DC power between 10.5 and 11 VDC, depending on the speed and load of the motor. Since the fan was drawing power from the shaft of the engine, it was deduced that by removing the fan load from the engine, an increase in fuel conversion efficiency or a decrease in the fuel consumption rate could be obtained. The fan could then be powered by the DC power output by the TEG. In essence, the engine would be cooled using the energy contained in its own rejected heat.

It was initially evaluated that the heat rejected through the cooling radiator would be sufficient to power the TEG. Much more heat was rejected through the exhaust of the engine, but it was believed that the temperatures therein would be too high; the exhaust gas reaches as high as 515°C with the generator under a 2.4kW load. Low alloy aluminum was chosen for the heat exchanger's fin material and the melting point of low alloy aluminum is around 643°C. A common rule of thumb is to not use a material at or above 2/3 of its melting temperature. 515°C is 83% of the melting temperature of aluminum. It was for this reason that the exhaust gas was not initially chosen for the hot-side working fluid of the TE heat exchanger. It was felt, however, that the exhaust temperatures at the idle and full speed/no load conditions, 315°C and 425°C respectively, may be suitable for use with the FDP. It

was finally decided that since the energy expelled through the exhaust was many times that expelled by the radiator, more electrical power could be obtained by using the exhaust. From before, the overall efficiency of the TE module is a function of the applied temperature gradient; therefore, higher temperature yields higher efficiency. The thermal limitations of the aluminum were outweighed by the much greater amount of thermal energy and higher temperature of the exhaust.

The lower load consideration brought about the idea that more could be benefited from reducing the engine's fuel consumption at low and no load conditions. Many large gensets run continuously regardless if a load is present. A primary power genset, like those found in remote military encampments, may be continuously running on standby because power may be needed at any time. If the fuel consumption of a continuously running genset could be reduced even a few percent, the overall benefit in cost and fuel savings would be very large. In the case of the ES6500, the fan drew 50-60W, or about 1% of the genset's peak load capability. Larger stationary power gensets can require cooling fans that draw 12-16% of the genset's peak output capability. The removal of a parasitic load of this magnitude would be extremely beneficial and worthwhile.

Honda ES6500 CAD Model

The genset was recreated in CAD in order to successfully design the FDP integration. The CAD model was used extensively as a guide for interference detection and feasibility of design modifications. Being able to see how the FDP

integrated into the genset was very advantageous. The following figures show the CAD model of the stock Honda ES6500 genset.

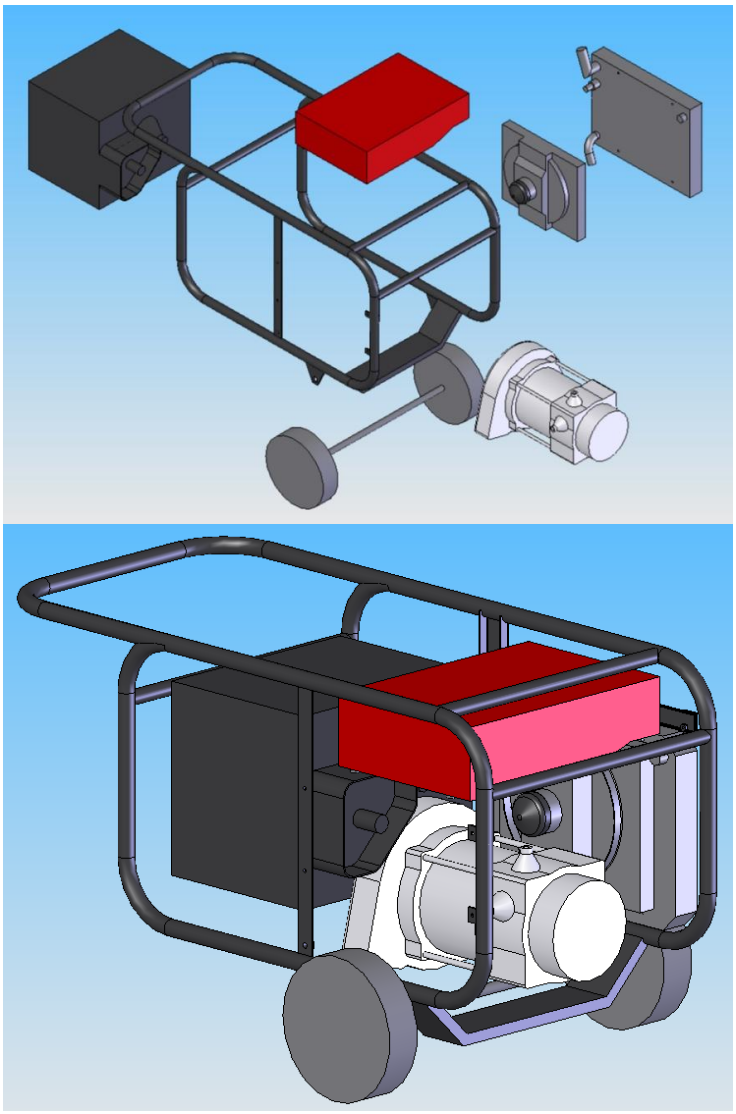

Figure 68: CAD Model of Stock Honda ES6500 Genset[7]

Figure 68 shows the CAD model of the stock genset with the muffler removed. The engine is represented as a generic block since the only pertinent

[7] CAD model by Nik Sorenson

feature was the exhaust outlet. The generator is visible in white on the bottom and the fuel tank is red on top. The radiator and fan housing can be seen in the back on the right side. Minor modifications were made to the genset structure to accommodate the FDP. The modified genset is shown in Figure 69.

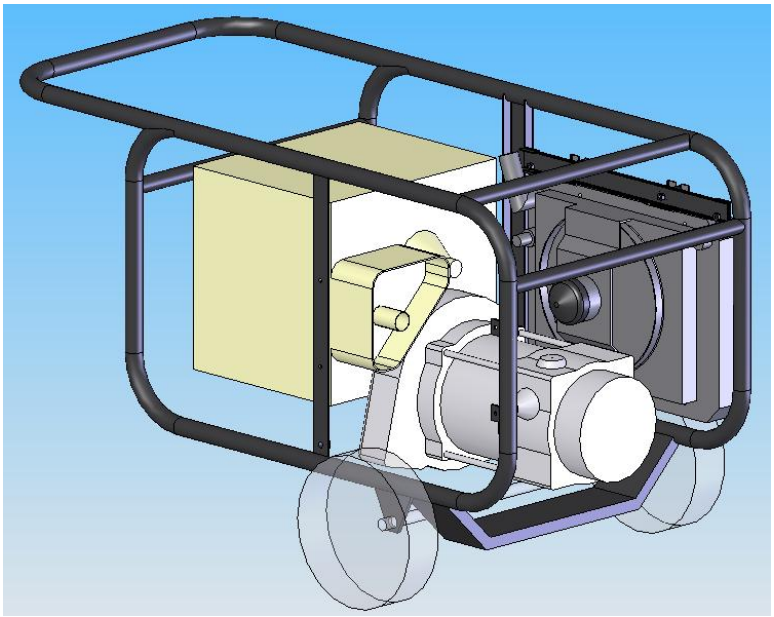

Figure 69: CAD of Modified Genset

The modifications made to the genset were generally minor, yet notable. The fuel tank was removed. The radiator was moved upward and outward ½" to make a straighter path for which to run ducting between the FDP and radiator outlet. Other modifications included removing small tabs and other non-vital components.

The ES6500 was arranged so that implementation of the FDP was quite simple and did not require drastic modifications. In its stock configuration, the air from the radiator was directed in the direction of the exhaust system. This orientation was very beneficial to the design and dramatically cut down the

modifications required to implement the FDP. Figure 70 shows the layout of the genset with the FDP in place of the muffler.

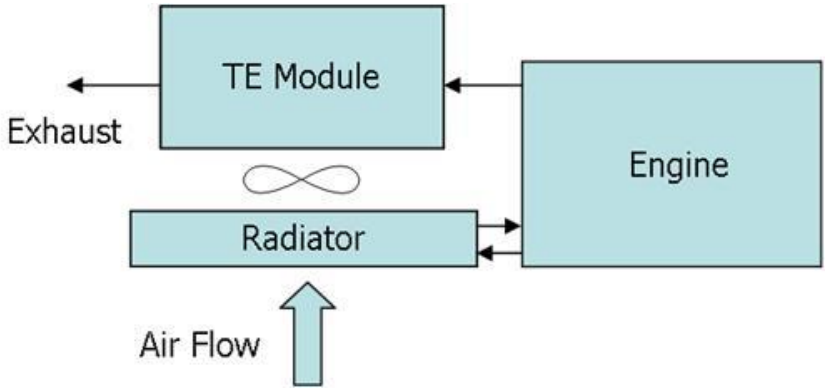

Figure 70: Honda ES6500 Genset Layout

Stock Running Conditions

The genset was operated in its stock configuration on both gasoline and propane fuel. Table 8 features a performance comparison of the Honda genset in its stock form, running on gasoline and propane.

Table 8: Comparison of Honda Genset Performance on Gasoline and Propane

	Gasoline			Propane		
Measurement	**Idle**	**No Load**	**2.4kW**	**Idle**	**No Load**	**2.4kW**
Exhaust Gas Temp - tailpipe outlet (°C)	204	302	371	165	282	401
Exhaust Gas Temp - muffler inlet (°C)	NA	NA	NA	~315	~430	515
Engine Coolant Temp Into Radiator (°C)	62.8	71.1	85	~38	80	83.2
Engine Coolant Temp Out of Radiator (°C)	29.4	35	40.5	~21	23.9	34.5
Coolant ΔT - Average (°C)	33.4	36.1	44.5	~17	31.2	27.1
Air Into Radiator (°C)	21.1	23.9	26.7	~10	~16	19.2
Air Out of Radiator (°C)	32.2	37.8	43.3	~10	~32	35.7
Air ΔT (Average) (°C)	11.1	13.9	16.6	~0	~16	16.5
Radiator Fan Voltage (VDC) (average)	9.95	10.49	10.87	~10.5	10.58	10.84
Radiator Fan Current (ADC) (average)	5.23	5.68	6.25	~5.25	5.3	5.26
Radiator Fan Power P=VI (W)	52.04	59.58	67.94	55.13	56.07	57.02
Coolant Flow Rate - min, max, avg (L/min)[2]	2.8, 5.6, 4.2			2.8, 5.6, 4.2		
Exhaust Backpressure (muffler inlet) (kPa)				0.4771	1.229	3.244
Calculated Radiator Air Flow Rate (gm/s)						1006
Calculated Engine Exhaust Flow Rate (gm/s)						12.75
Average Fuel Conversion Efficiency (LHV, %)[3]						9.13

1: Approximate values for idle and no load due to short data time

2: When at operating temp, flow rate shows little variance with load

3: Efficiency = Load (W)/(fuel mass burned(kg)*LHV(J/kg)/load time(s)) LHV of propane=45.8E6 J/kg

Figure 71, Figure 72, and Figure 73 are typical stock running conditions of the instrumented Honda genset running on propane fuel.

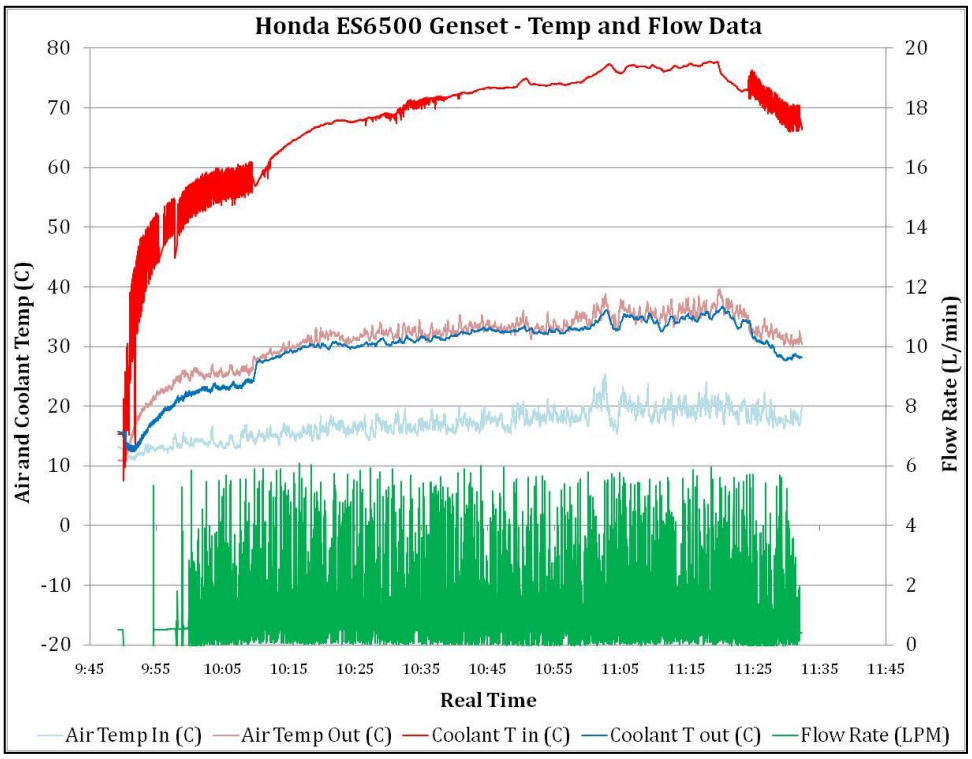

Figure 71: Stock Honda Coolant System Temperatures and Flow Rate

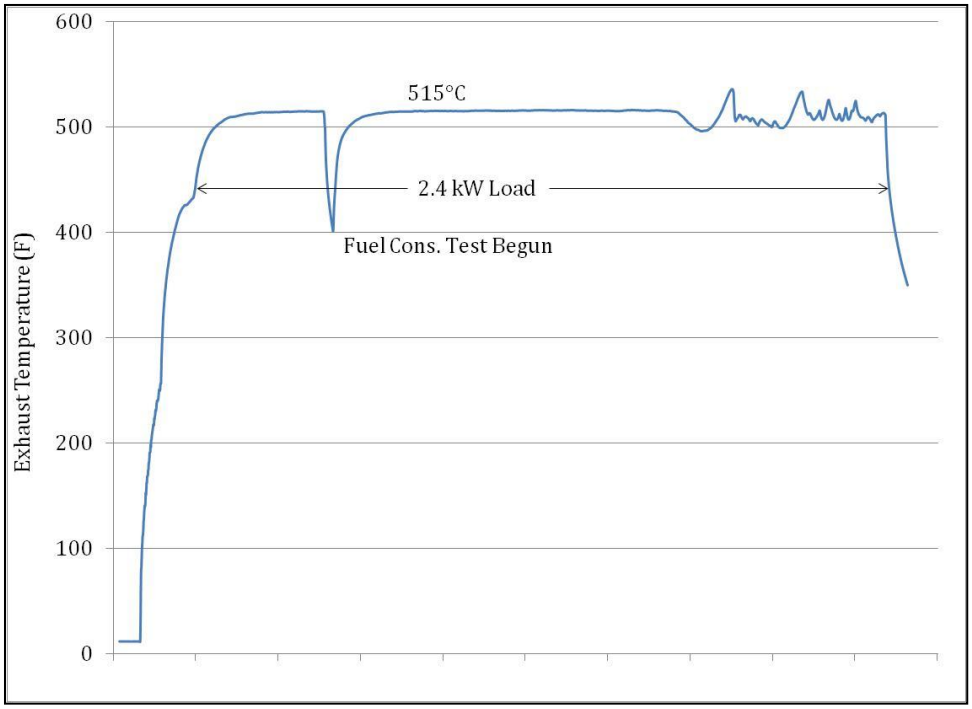

Figure 72: Stock Honda Exhaust Temperature at Muffler Inlet

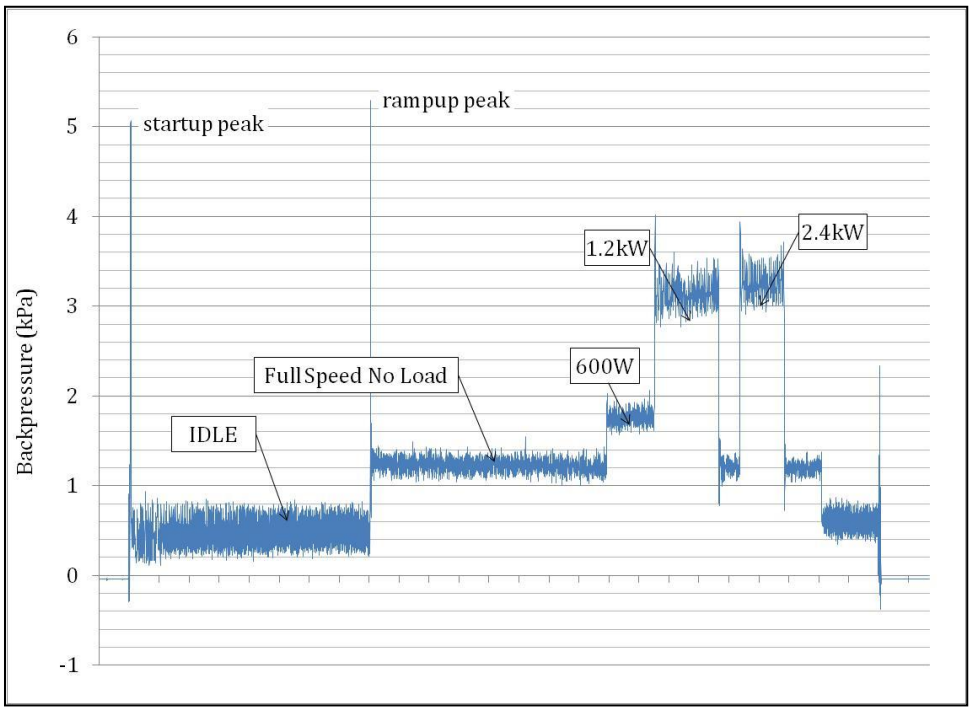

Figure 73: Stock Honda Exhaust Back-Pressure

Fan Power Data

The stock radiator fan was powered externally over a range of input voltages. The current and voltage were monitored and used to calculate the internal resistance and power consumed by the fan over the voltage input range of 10-15.5VDC. Figure 74 shows the current and power data for the fan.

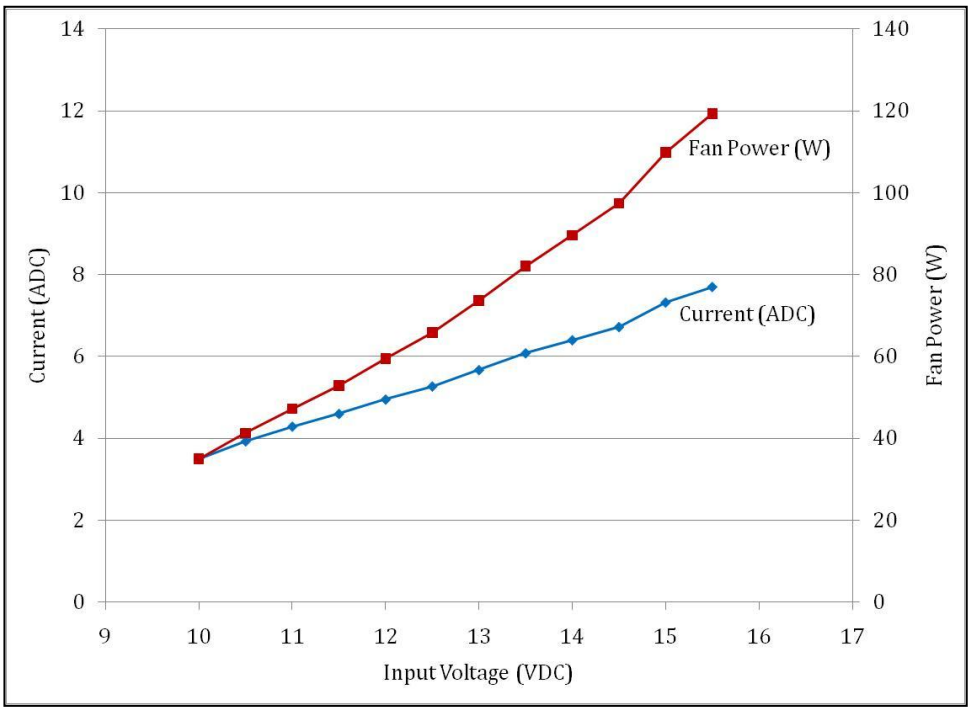

Figure 74: Fan Performance vs. Applied Voltage

Fuel Consumption and Efficiency Testing

Figure 75 is a plot of the measured conversion efficiency vs. load of the genset while running on propane fuel.

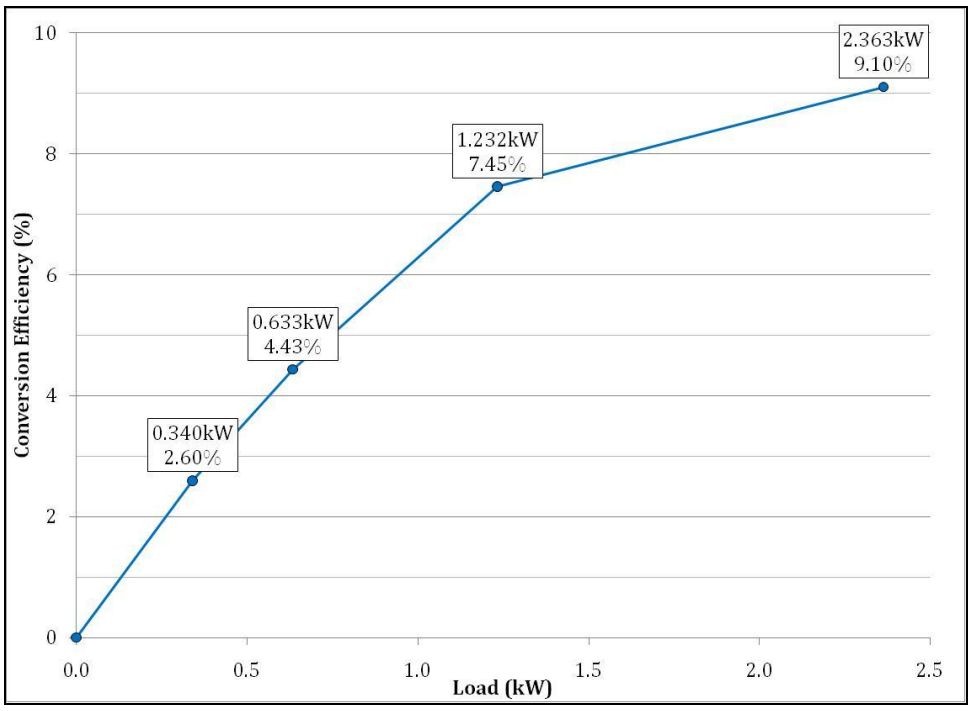

Figure 75: Honda ES6500 Efficiency vs. Load

Additionally, the fuel consumption rates were measured for the genset running in the no-load condition. The fuel consumption rate of the genset was measured for three different conditions: the genset running in its stock configuration; with the FDP in place of the muffler; and with the fan being powered externally (while the muffler was replaced). These flow rates show improvements in fuel consumption with respect to modifications. Table 9 shows the improvement in fuel consumption rate.

Table 9: Fuel Consumption Rate Improvements (no load condition)

Operating Condition	**Fuel Consumption Rate (kg/hr)**	**Overall Improvement (%)**
Stock Genset	0.999	N/A
FDP in Place of Muffler	0.883	11.62
Fan Powered Externally	0.869	13.07

Field Demonstration Prototype

FDP Performance Modeling

The performance of the Thermohex® design was modeled using numerical analyses as well as empirical data gathered from SSP and FDP testing. The temperature distribution of the module was approximated using a counterflow heat exchanger ε-NTU assumption and a numerical model to determine the temperature profile within the FDP (Lindstrom 2005). The model included several assumptions:

- The control volume was considered adiabatic
- Heat transfer coefficients were considered constant
- Extended surface efficiencies were considered constant
- Temperature gradients transverse to the flow direction were neglected
- Flow maldistribution was neglected
- Longitudinal conduction was neglected
- Radiation heat transfer was neglected

The modeled temperature profile was then used to determine the TE effects and overall performance of the module. Since the design of the FDP was not truly a counterflow heat exchanger and the assumptions did not perfectly model the design and actual processes it was difficult to produce perfectly matching results. Nonetheless, the numerical model did give a solid starting point from which to progress the design. The numerical model was continuously updated and optimized as new empirical data became available from SSP and FDP testing. Table 10 is a list of target specifications obtained through numerical modeling.

Table 10: FDP Target Specs

Heat Exchanger Properties			
m_h, m_c (gm/s)	13.3, 317	T_{hi}, T_{ho} (C)	350, 258
A_h, A_c (m^2)	0.641, 3.71	T_{ci}, T_{co} (C)	30, 34
β_h, β_c (m^{-1})	430, 430	C_{star} (-)	0.048
Re_h, Re_c (-)	171, 3579	ε (%)	0.29
h_h, h_c ($W/m^2 \cdot K$)	40.6, 32.8	Q (W)	1411
ΔP_h, ΔP_c (Pa)	186, 89.6	L x W x H (cm)	22.1x27.4x31.8
PP_h, PP_c (W)	4.55, 33.2	Total Mass (kg)	46.3
Thermoelectric Properties			
T_{eh}, T_{ec} (C)	221, 66	q_e (W/cm^2)	14.93
α ($10^{-6} \cdot V/K$)	187	ρ ($10^{-5} \cdot \Omega \cdot m$)	1.03
k ($W/m \cdot K$)	1.467	FOM ($10^{-3} \cdot K^{-1}$)	2.32
V_m (V)	12.178	I_m (A)	5.063
P_m (W)	61.66	IR (Ω)	0.521

Table 11: Description of Terms for Table 10

Symbol	Description
A	Hot Side Total heat transfer Area
FOM	Thermoelectric figure of merit
h	Convective heat transfer coefficient
H	Heat exchanger height
I	Electric current
IR	Internal resistance
k	Thermal conductivity
L	Heat exchanger length
m	Mass flow rate
P	Electric power
PP	Pumping power
q	Heat flux
Q	Total heat exchanger duty
Re	Reynolds number
T	Temperature
V	Voltage
W	Heat exchanger width
Greek	
α	Seebeck Coefficient
β	Compactness, ratio of heat transfer area on one side of a heat exchanger to the volume between the plates on that side
ΔP	Pressure drop of one fluid side
ε	Heat exchanger effectiveness
ρ	Resistivity
Subscripts	
c	Cold side
h	Hot side
e	Thermoelectric element
i	Inlet
m	Matched load
o	Outlet

FDP CAD Model and Design Progression

The information gained from the design, construction and testing of the SSP was directly used in the FDP progression. Initially, the fin design did not feature the tab configuration, but as it was introduced and tested in the SSP, it was added to the FDP. Figure 76 shows an early CAD model of the FDP. This model featured a similar serpentine conduction path with 3 single dice in contact with the fins.

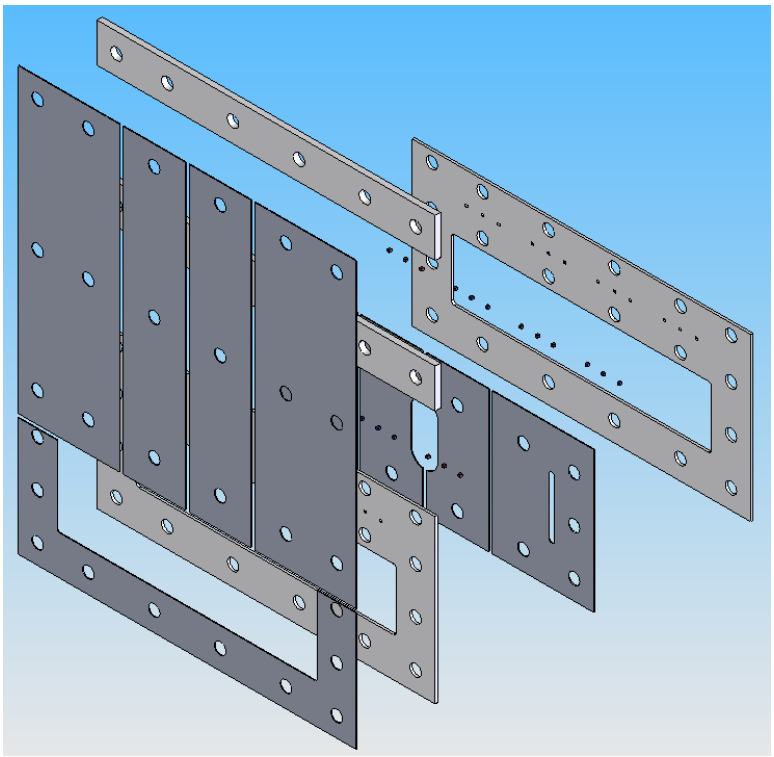

Figure 76: Early CAD Model of 1 Cell of FDP[8]

Just as in the SSP, the fin tab design and dice clusters were employed as a means to improve the heat transfer to and from the dice. This design featured

[8] CAD model by Nik Sorenson

aluminum fins for the hot and cold sides as well as steel spacers. As the SSP design progressed, the FDP design was also changed to match the improvements seen. When fin tabs and cold-side copper fins were added to the SSP, tested and verified, they were also added to the FDP design. The following figures feature internal layers of the FDP.

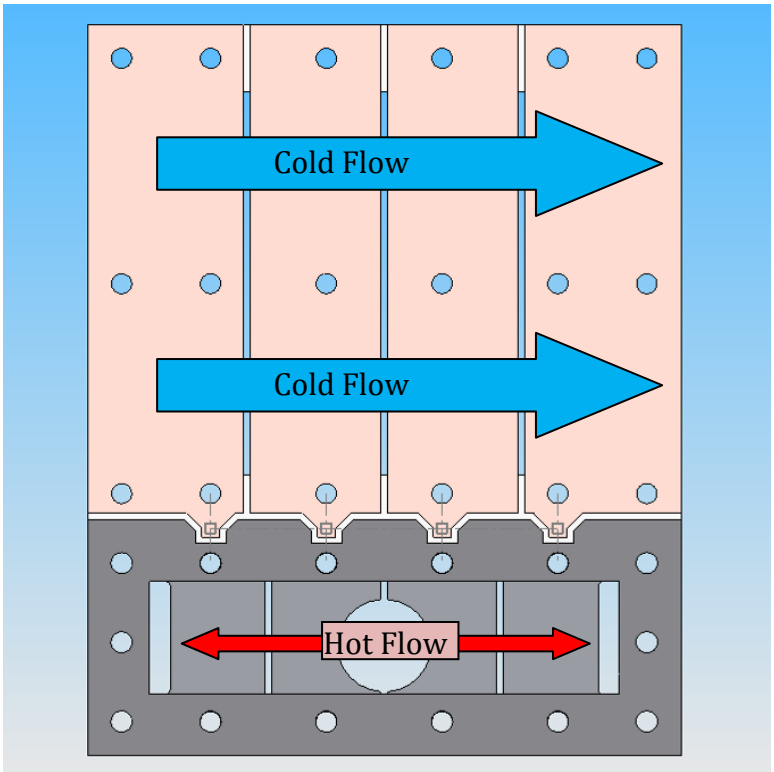

Figure 77: Cold-Side Layer of FDP with Tab Design[9]

[9] CAD model by Nik Sorenson

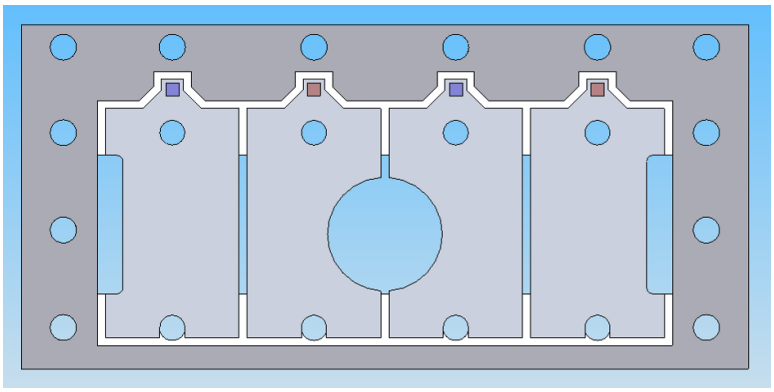

Figure 78: Detail View of Hot-Side Fins

The CAD model was instrumental in the design, construction and optimization of the FDP module. The CAD software coupled with the capabilities of CNC machining allowed for almost any conceivable shape to be constructed for the module. The final CAD model is shown in Figure 79.

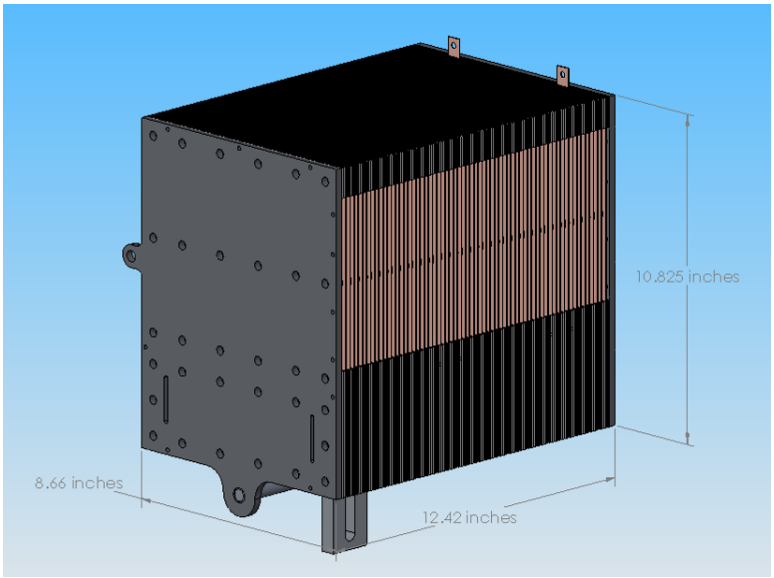

Figure 79: FDP Final CAD Model[10]

[10] CAD model by Nik Sorenson

It is desired to eventually use the CAD model in finite element analysis software in order to help better understand the thermal processes that occur within. The complexity of the internal thermal processes is extremely difficult to model and predict.

FDP Components

The design of the internal components of the FDP was directly dependant on the results obtained through the testing of the SSP. The fin tab design was carried over from the SSP results. The steel spacers were also continued. Initially, 1018 steel was used for the spacer design in the FDP. This material was stitched with 304 SS due to issues encountered with corrosion and thermal bypass within the stack. Concurrently, the design of the spacers themselves was altered to aid in preventing thermal bypass from the spacers on the hot side to the cold-side fins. By redesigning and changing the material of the steel spacers, a 50% increase (from 3.69VDC to 5.49VDC) in the open-circuit voltage of the FDP was attained.

FDP Shroud

Several iterations of the shroud were developed and attempted. Many existing design challenges were needed to be approached and overcome. First, the inlet of the FDP was square whereas the outlet of the radiator was round. Also, the radiator and FDP inlet were not aligned in a convenient manner. The following picture shows the eccentricity of the radiator open vs. the FDP inlet.

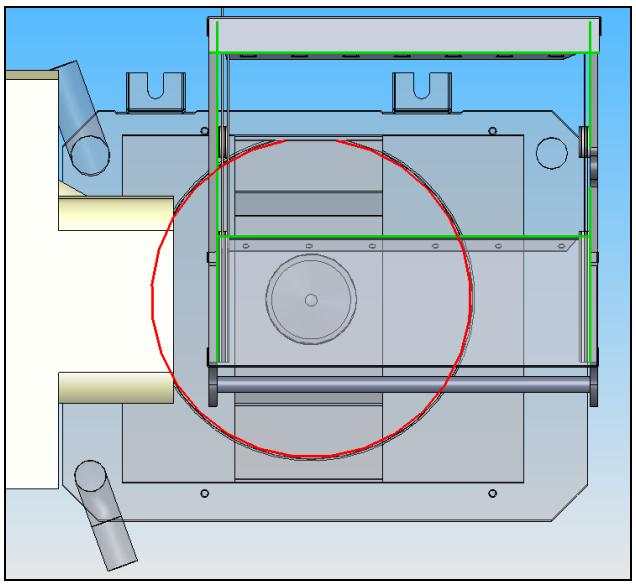

Figure 80: Eccentricity of Radiator Outlet vs. FDP Inlet[11]

The red line outlines the radiator outlet while the green lines show the FDP inlet. As is apparent from this view, mating the stock radiator to the FDP inlet was no trivial matter.

FDP Shroud Design Progression: The shroud design started as a round inlet at the radiator and a square outlet to the FDP. The idea was to find the optimal mating geometry between the radiator outlet and the FDP cold inlet. The round to square FDP shroud is shown below.

[11] CAD model by Nik Sorenson

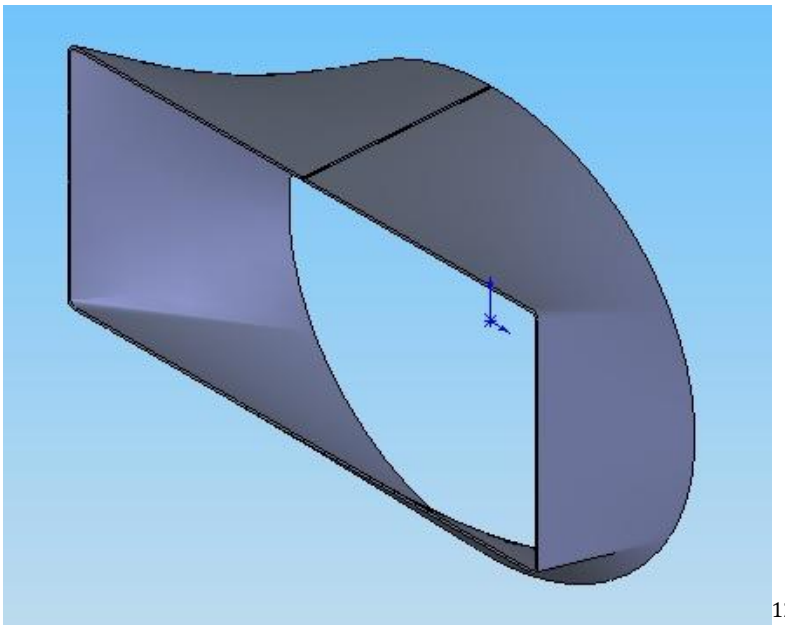 [12]

Figure 81: Round to Square FDP Shroud Design

It was determined through trial and error that the fabrication of a sheet metal part with a round opening on one end and a square on the other would be very difficult if not impossible for the intended application. It was then decided that a polygonal opening on the radiator side would closely mimic the desired round shape. An eight-sided design was chosen and is shown in Figure 82.

[12] CAD model by Nik Sorenson

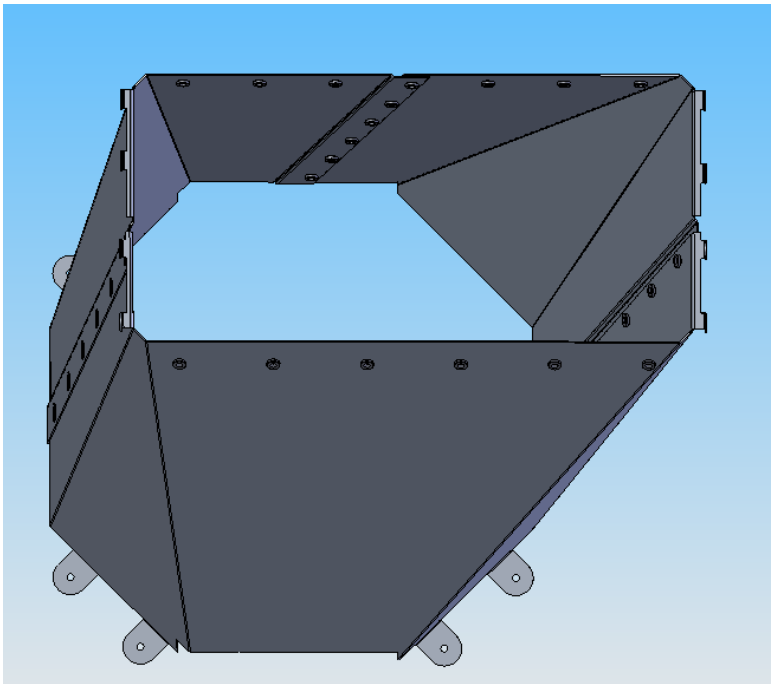

Figure 82: Eight-Sided FDP Shroud CAD Model[13]

JE Soares of Belgrade, MT was solicited to fabricate the shroud components. The patterns were cut from 5052 aluminum sheet and bent into form using press breaks. Figure 83 shows the shroud installed into the genset.

[13] CAD model by Nik Sorenson

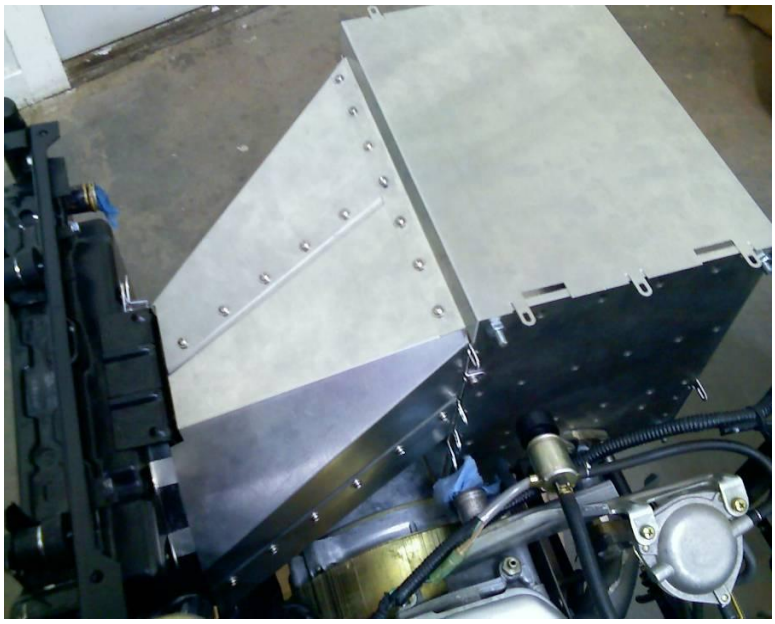

Figure 83: Eight-Sided Shroud Installed in Genset

The shroud was designed with three pieces for the ducting between the radiator and FDP and two others to mate to the FDP. The modular design allowed for great ease of assembly. The success of the eight-sided shroud led to the notion that maybe an even better fit could be attained with a more detailed profile. A 16-sided shroud was designed and a CAD model was completed but has not been fabricated as of yet. The model has been inspected by JE Soares and it is felt that it is feasible to construct should the need arise. The 16-sided shroud will facilitate a better air seal since it more closely resembles the round outlet of the radiator. Its CAD Model is shown below.

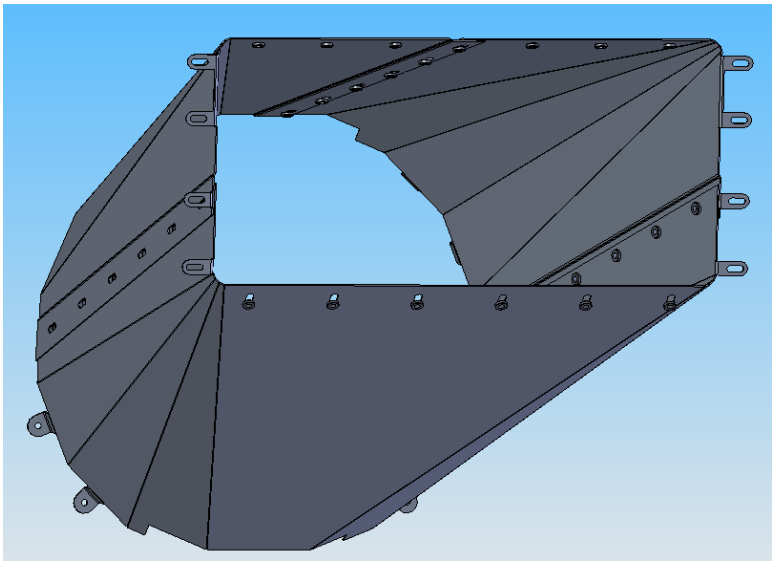

Figure 84: 16-Sided FDP Shroud CAD Model[14]

Non-Functional Mock-Up

FDP Back-Pressure Testing: The backpressure exerted on the engine by the FDP mock-up was measured. At idle, the backpressure was 0.483kPa. At full-speed/no load, it was 1.10kPa. Compared to 0.483kPa (idle) and 1.24kPa (full speed) for the backpressure exerted by the stock muffler, the backpressure exerted by the FDP at full speed, no load was 11.1% less than that of the stock exhaust system.

Fan Flow Rate Testing: The volumetric air flow through the cold-side of the FDP was measured using what is known as a static pressure tube test. For this method, the total dynamic pressure, i.e. the pressure exerted due to velocity, is used

[14] CAD Model by Nik Sorenson

to convert the pressure drop to fluid energy and, ultimately, flow rate. The static pressure tube simply measures dynamic pressure with the use of a differential pressure transducer. The dynamic pressure is the difference between the total pressure facing into the flow stream and the static pressure within the duct. (Beckwith 1995) The dynamic pressure is then used to approximate the fluid flow rate using Bernoulli's fluid energy equation. The concept of a static pressure probe measurement is shown below.

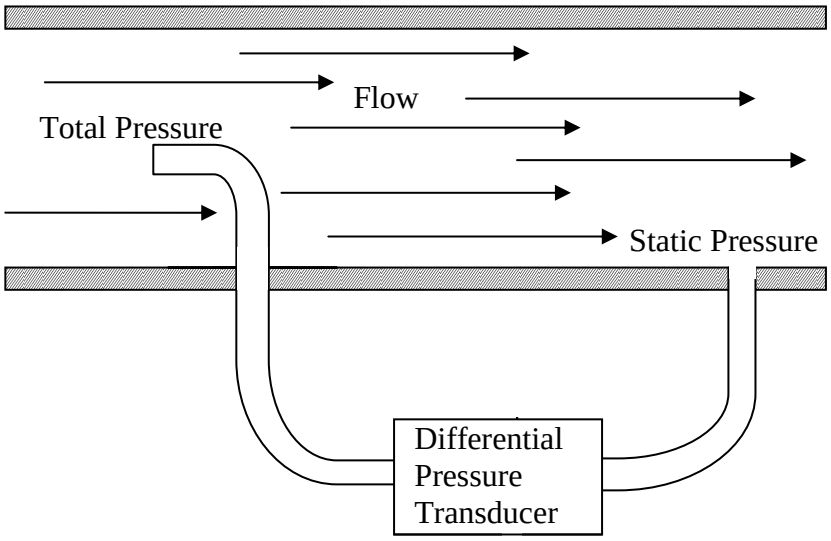

Figure 85: Static Pressure Probe

The pressure drop data was then used to calculate the flow rate through the cold side using Bernoulli's Energy Principle of Fluid Dynamics. The flow rate was approximated using the following assumptions:

- Inviscid flow
- Developed flow
- Incompressible flow
- Constant density
- Fluid performs no work and transfers no heat during flow

The inviscid and developed assumptions are satisfied for high Reynolds numbers (>4000). The Reynolds number for the air flow in this case was on the order of 10^5, thus was assumed to be developing/fully developed and boundary effects were neglected. In terms of compressibility, air can be assumed to be incompressible at Mach numbers less than 0.3 (Munson 2006). In this case, the Mach number was on the order of 6E-3 so the assumption was valid. The Reynolds and Mach numbers are provided below. The constant density and no heat transfer/no work assumptions were adequate approximations for the present effort.

$$Re = \rho \cdot V \cdot l / \mu \tag{12}$$

$$Ma = V/c \tag{13}$$

Where ρ is the fluid density, V is the fluid velocity, l is characteristic length, μ is the dynamic viscosity of the fluid and c is the speed of sound in the fluid. Bernoulli's general energy equation for the flow of incompressible fluids is represented in the following form:

$$P_1 + \tfrac{1}{2} \cdot \rho_1 \cdot V_1^2 + g_1 \rho_1 z_1 = P_2 + \tfrac{1}{2} \cdot \rho_2 \cdot V_2^2 + g_2 \rho_2 z_2 \tag{14}$$

For flow in a closed duct, the static tube method was used to determine the velocity of the fluid. For this study, the following assumptions were made:

- No elevation difference:
  - $z_1 = z_2 = z$
- Density of dynamic air assumed to be same as static air:
  - $\rho_1 = \rho_2 = \rho$

- P_1 is stagnant (total) pressure on tube facing flow
- P_2 is static pressure on tube perpendicular to flow
    - assumed to be ambient pressure in this case
- ΔP Measured by differential pressure transducer:
    - $\Delta P = P_{dynamic} = P_1 - P_2 = P_{total} - P_{static}$
- V_1 is the velocity of the fluid at the stagnant tube
- V_2 is ambient air velocity,
    - assumed to be negligible in comparison to velocity of forced air
- Gravitational constant g assumed to be constant at all locations:
    - $g_1 = g_2 = g$
- Since z, ρ and g are constants, their terms cancel one another out from each side of equation 9

When the above assumptions are applied to the Bernoulli's energy equation, it becomes the following:

$$P_1 + \frac{1}{2} \cdot \rho_1 \cdot V_1^2 = P_2 \tag{15}$$

By rearranging equation 10 and, taking $P_2 - P_1 = \Delta P$ solving for V_1, the following relation is yielded:

$$V_1 = \sqrt{\frac{2 \cdot (\Delta P)}{\rho}} \tag{16}$$

Where ΔP (dynamic pressure) is the difference between the total and static pressures of the fluid flow, V_1 is the velocity of the dynamic fluid and ρ is the density of the fluid. ΔP is measured directly using the differential pressure transducer. The measured value for dynamic pressure can simply be inserted into the equation and

the fluid velocity can be calculated. The velocity can then be used to calculate the volumetric flow rate using the following equation:

$$Q = V \cdot A \tag{17}$$

Where Q is the volumetric flow rate, V is the velocity, and A is the flow area perpendicular to the flow.

A notable difference between the theory applied and the method used was that the static pressure, P2, was assumed to be ambient air pressure. This was done for the reason that making an accurate static duct pressure proved too difficult. When the static pressure measurement is made in conventional static tube use, special care is taken to ensure that the pressure measured is not affected by the flow of the fluid. In theory, this concept is simple; in practice, however, it is not. If the geometry of the tube measuring static pressure is not situated perfectly, the flow of the air will have an effect. It was for this reason that the static pressure within the tube was assumed to be equal or near ambient air pressure. In reality, the static pressure within the duct may be greater than ambient. The approximation used, therefore, overestimates the flow rate of the fluid.

10 tubes were inserted through the cold-side fin bank to the leading edge of the fin inlet. The pressure drop at each one of the tube sites was measured. The following figure shows the locations of the tubes with respect to the module.

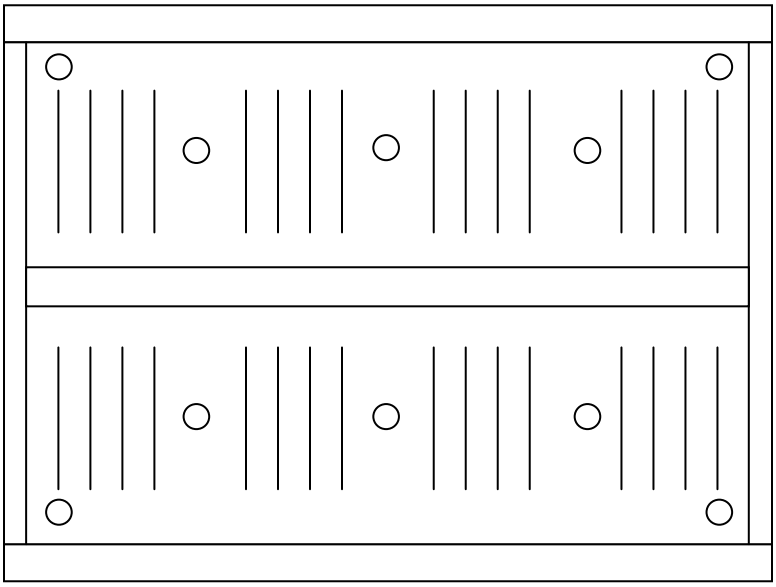

Figure 86: FDP Cold-Side Air Flow Rate Locations

The air flow rate testing was performed twice and both tests used the static-tube method for air flow rate measurement. The first test was performed with the engine running and powering the radiator fan in its stock configuration. The range of the PX139-015D4V differential pressure transducer was ±100kPa whereas the total pressure to be measured was on the order of 6.9Pa; so needless to say, the transducer's range was too broad to read the pressures with very high precision. The first flow rate testing yielded the following results:

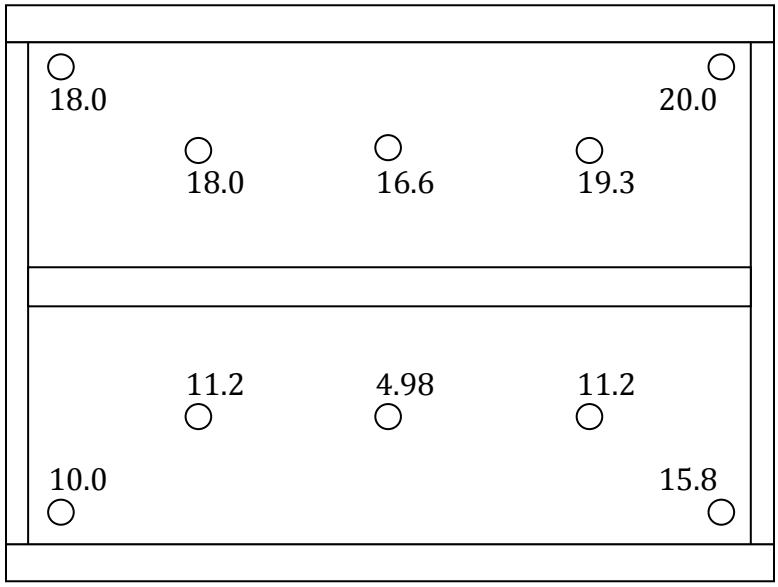

Figure 87: Cold-Side Air Flow Rates-Test 1 (m^3/min)

The second test was performed by powering the fan externally with a variable voltage DC rectifier and varying the voltage from 10-15.5VDC. The PX164-010D5V differential pressure transducer measured a pressure range of 0-2.488kPa. This transducer much better suited for this measurement. A higher precision differential pressure transducer would have better suited the test, but higher sensitivity transducers were much more expensive and it was decided that the lower precision would suffice. The second set of testing yielded flow rates for all 10 zones over the voltage input range of 10-15.5VDC into the radiator fan. The results for this test are shown below:

Table 12: Cold-Side Air Flow Rates-Test 2

FAN POWER SPECS		FLOW RATE MEASUREMENTS		
Voltage (V)	**Power (W)**	**Top Avg. (m^3/min)**	**Bottom Avg. (m^3/min)**	**Total Avg. (m^3/min)**
10.0	35.0	12.71	7.453	10.08
10.5	41.3	13.85	8.061	10.96
11.0	47.2	14.69	8.889	11.79
11.5	52.9	15.36	9.404	12.38
12.0	59.4	16.15	9.911	13.03
12.5	65.9	16.72	10.21	13.47
13.0	73.7	17.32	10.54	13.93
13.5	82.1	17.95	11.07	14.51
14.0	89.6	18.60	11.46	15.03
14.5	97.4	19.25	11.68	15.46
15.0	109.8	19.94	12.21	16.08
15.5	119.4	20.56	12.84	16.70

FDP Mockup Assembly: Assembling the mockup FDP was beneficial in terms of discovering the nuances and techniques required in a module of its size. The internal workings were essentially a repeating pattern of fins, spacers and insulation pieces. It was easy to forget a piece or double up on single pieces; so much care was taken in maintaining the correct number and placement of the parts.

The backpressure and fan flow rate testing were very beneficial. A major concern with the FDP design early on was that it may impose too much backpressure on the engine. This concern was immediately quenched with the test. The fan flow rate testing was another issue of concern. Until the FDP and shroud were in place and the fan was operated, it was not known how the fan would react to the sudden air flow restriction. The installation and testing of the FDP mockup calmed many concerns with the genset's overall response to the foreign objects installed onto its systems.

FDP Functional Builds

As of yet, two fully-functional FDP builds have been assembled. Build 1 was subjected to approximately 6 hours of testing in all. The open-circuit voltage was not as high as expected, but nonetheless it is felt that any voltage on the first try is a success. When Build 1 was disassembled, it was noticed that 5 layers of middle aluminum fins were slightly warped from the heat. From the results gained in testing Build 1, the internal steel spacer configuration was significantly altered and new spacers were constructed out of 304 SS. The new design had a two-pronged function; the new spacer layout was intended to help decrease the amount of thermal bypass from the hot steel spacers to the cold fins, and the use of SS inherently would decrease the amount of heat bypass by virtue of its lower thermal conductivity.

Build 2 featured the dice and fins from Build 1 as well as the new steel spacer design. The stack was assembled and begun to be compressed, but the insulation had crept down slightly from use in Build 1 so that the overall thickness of the FDP became less than 30.5cm, the length of the anodized aluminum insulation tubes. So as not to damage the aluminum tubes, an entire cell (two layers of dice) was added in order to increase the thickness of the stack without fundamentally changing anything. Build 2 then held 512 layers of series dice clusters. The internal resistance was much higher than anticipated when Build 2 was installed. It dropped after testing which lead to the notion that the internal compression was inadequate. Steps were taken to improve the compression of the contacts within.

FDP Build #1: 10/31/09–11/20/09

The internal resistance of Build 1 of the FDP was 518mΩ when it was installed into the genset. The fully functional Build 1 of the FDP was installed in the genset and operated to both the idle and full speed, no load conditions. At idle, the exhaust temperature reached a maximum of 285°C and the FDP reached a maximum open-circuit voltage of 2.38VDC. At the full speed, no load condition, the exhaust temperature was 355°C and the maximum open-circuit voltage was 3.69VDC. The internal resistance of Build 1 was 550mΩ when testing was complete.

FDP Build #2: 12/7/09–12/15/09

The internal resistance of Build 2 was 885mΩ when it was installed. Build 2 of the FDP was run in the genset at the full speed, no load condition. The exhaust temperature reached a maximum of 345°C. FDP Build 2 reached a maximum open-circuit voltage of 5.49VDC and a maximum power output of 8.49W at 2.99VDC and 2.84ADC. The internal resistance of Build 2 had fallen to 660mΩ after the load test was performed.

CHAPTER 6

FUTURE WORK

SSP Future Work

The SSP has been instrumental in the design progression of the Thermohex® concept. Changes made to the fundamental design will be evaluated first in the SSP to minimize time requirements and to mitigate costs associated with part fabrication.

FDP Future Work

Further FDP Testing

More FDP testing is required. Build 2 will be tested further before it is dismantled and examined. The procedure that will be used for more testing of Build 2 will yield higher power output due to improved electrical contacts.

FDP Design Improvements

It has been hypothesized that changing the hot fin material from 1100-O aluminum to C100 copper would have an advantageous effect on the open-circuit voltage capability of the FDP. Copper fins to replace the hot aluminum have been procured and are awaiting integration. The copper added to the hot side of the TE dice will facilitate a higher temperature gradient therein, increasing the output of the TE elements as a whole.

The use of copper on the hot-side of the FDP does come with its own risks. The temperatures and conditions seen in the exhaust stream will promote the copper to oxidize and spall. To prevent such occurrences, the copper fins will be fully clad in ~8μm of nickel plating. The nickel plating is intended to prevent cupric oxide growth on the fin surface, while at the same time, not hindering the heat transfer from the exhaust stream to the fins.

Thermohex® Design Applications

The Thermohex® design is currently under development as a heat pump as well as a TEG. As a heat pump, it is anticipated that the Thermohex® design will be used as a quiet and robust environmental control unit.

REFERENCES CITED

Ashby, Michael; Shercliff, High; Cebon, David. Materials: Engineering, Science, Processing and Design. Elsevier, Ltd. Oxford, UK. 2007.

Balducci, A.; Marinelli, Marco; et al. "CVD-Diamond-based Thermocouple for High Sensitive Temperature Measurements." Springer-Verlag. Heidelberg, Germany. *Microsyst Technol* 12 (2006): 365–368.

Beckwith; Marangoni; Lienhard. Mechanical Measurements. Fifth Ed. Addison-Wesley Publishing Co. Reading, MA. 1995.

Bennett, Gary L. "Mission interplanetary: Using radioisotope power to explore the solar system." Elsevier. Oxford, UK. *Energy Conversion and Management*: 49 (2008): 382–392.

Blatt, Frank J.; Schroeder, Peter A.; Foiles, Carl L.; Greig, Dennis. Thermoelectric Power of Metals, Plenum Press. NY & London. 1976.

"Brayton Cycle." *Wikipedia*. Wikimedia Foundation, Inc. 2003. Web. <http://en.wikipedia.org/wiki/Brayton_cycle>

Burns, Gerald. Solid State Physics. Academic Press, Inc. Orlando, FL. 1985.

Cadoff, Irving B.; Miller, Edward. Thermoelectric Materials and Devices. Reinhold Publishing Corp. New York, NY. 1960.

"The Caswell Plating Manual." Version 8. Caswell, Inc.

Cusack, N. The Electrical and Magnetic Properties of Solids. Longmans, Green and Co. London, UK. 1958.

Davis, Joseph R. ASM Handbook Vol. 2: Properties & Selection: Nonferrous Alloys and Special Purpose Materials. ASM International. (1990) 871

Dowling, Norman E. Mechanical Behavior of Materials. Second Ed. Prentice Hall. Upper Saddle River, NJ. 1999.

Egli, Paul H. Thermoelectricity. John Wiley and Sons. New York, NY. 1960.

Global Thermoelectric. "Thermoelectric Generator Brochure." Calgary, Alberta, Canada. Web. <http://www.globalte.com/>

Goldsmid, H.J. "A simple technique for determining the Seebeck coefficient of thermoelectric materials." Marlow Industries Inc. Dallas, TX. *J. Phys. E: Sci. Instrum*. 19 (1986): 921-922.

Hi-Z. "Waste Heat Recovery Brochure." San Diego. 2006.

Honda Motor Co., Ltd. *Honda Power Equipment Owners Manual: Generator ES6500*. Part # 00X31-ZA0-7240. Japan. 2002.

Hori, Y.; Kusano, D.; Ito T.; Izumi, K. "Analysis on thermo-mechanical stress of thermoelectric module." 18th International Conference on Thermoelectrics (1999). IEEE 0-7803-5451-6/00. 2000.

Incropera, Frank P.; DeWitt, David P. Introduction to Heat Transfer. Fourth Ed. John Wiley and Sons. Hoboken, NJ. 2002.

Kanthal. "Alloys for Thermocouples, Extension and Compensating Cables." Kanthal AB. Catalog 4-A-1-3 3000 2. 02. Hallstahammar, Sweden.

Kaye, Joseph; Welsh, John A. Direct Conversion of Heat to Electricity. John Wiley and Sons. New York, NY. 1960.

Kittel, Charles. Introduction to Solid State Physics. Eighth Ed. John Wiley and Sons. Hoboken, NJ. 2005.

Kushner, Joseph B. "The Nickel Tank Doctor." Joseph B. Kushner Electroplating School. Stroudsburg, PA. 1955.

Lan, Y.C.; Wang, D.Z.; Chen,G.; Ren, Z.F. "Diffusion of nickel and tin in *p*-type $(Bi,Sb)_2Te_3$ and *n*-type $Bi_2(Te,Se)_3$ thermoelectric materials." *Applied Physics Letters*. 92 (2008): 101910

Lindstrom, Joel D. "Design and Evaluation of Compact Heat Exchangers for Hybrid Fuel Cell and Gas Turbine Systems." MS thesis Montana State University, 2005.

Manley, Oscar P. "Migration and Effects of Copper in P-Type Bismuth Telluride." *Technical Report 376. Massachusetts Institute of Technology.* Cambridge, MA. 1 September 1960.

McChesney, Mike. Electronic Materials and Processes Handbook. Third Ed. *CH 6: Electroplating and Deposited Metallic Coatings*. New York. McGraw-Hill. 2004.

Munson, Bruce R.; Young, Donald F.; Okiishi, Theodore H. Fundamentals of Fluid Mechanics. Fifth Ed. John Wiley and Sons. Hoboken, NJ. 2006.

Nolas, G. S.; Sharp, J.; Goldsmid, H.J. Thermoelectrics: Basic Principles and New Materials Developments. Springer-Verlag. Heidelberg, Germany. 2001.

Pan, Lawrence S.; Kania, Don R. Diamond: Electronic Properties and Applications. Kluwel Academic Pub. Norwell, MA. 1995.

Parsonnet. Victor. "Power Sources for Implantable Cardiac Pacemakers." *CHEST*. 61.2 (1973): 165-173.

"Radioisotope Thermoelectric Generator." *Wikipedia*. Wikimedia Foundation, Inc. 2003. Web. <http://en.wikipedia.org/wiki/Radioisotope_thermoelectric_generator>

Reed, James S. Introduction to the Principles of Ceramic Processing. John Wiley & Sons. New York. 1988. (p76-80)

Rowe, D.M.; Bhandari, C.M. Modern Thermoelectrics. Reston Publishing Company, Inc. Reston, VA. 1983.

Rowe, D.M. Thermoelectrics Handbook: Macro to Nano, Taylor & Francis Group. Boca Raton, FL. 2006.

Sanders, Gary G. "A Case for Bellevilles." Penberthy, Inc. 2000.

Seebeck, Thomas J. "Magnetische Polarisation der Metalle und Erze durch Temperatur-Differenz." *Abhand Deut. Akad. Wiss.* Berlin. (1822) 265-373. Web. <http://libcoll.mpiwg-berlin.mpg.de/libcoll_zogilib?fn=/permanent/einstein_exhibition/sources/7X568YX0/pageimg&pn=2>

Shigley, Joseph E.; Mischke, Charles R.; Budynas, Richard G. Mechanical Engineering Design. Seventh Ed. McGraw-Hill. New York, NY. 2004.

Sonnntag, Richard E.; Borgnakke, Claus; Van Wylen, Gordon J. Fundamentals of Thermodynamics. Sixth Ed. John Wiley and Sons. Hoboken, NJ. 2003.

Thermo-balance measurement of Calcium oxalate. Linseis Inc. Robbinsville, NJ.

"Thermoelectric Effect." *Wikipedia*. Wikimedia Foundation, Inc. 2003. Web. <http://en.wikipedia.org/wiki/Thermoelectric_effect>

Tittes, Kerstin; Bund, Andreas; et al. "Electrochemical Deposition of Bi2Te3 for Thermoelectric Microdevices."Springer-Verlag. Heidelberg, Germany. *J Solid State Electrochem*. 7 (2003): 714–723.

Tompkins, J. Andrew. "Engineering Evaluation of Nuclear Powered Pacemakers as Special Form Radioactive Material." LAUR-01-6353. Los Alamos National Laboratory. Nov 2000.

Uemura, K.I. "Short Course on Thermoelectrics –1993." International Thermoelectric Society. November 1993.

Yu, Peter Y.; Cardona, Manuel. Fundamentals of Semiconductors - Physics and Materials Properties. Thrid Ed. Springer-Verlag. Heidelberg, Germany. 2001.